

A quantum network node based on a nanophotonic interface for atoms in optical tweezers

A DISSERTATION PRESENTED
BY
POLNOP SAMUTPRAPHOOT
TO
THE DEPARTMENT OF PHYSICS

IN PARTIAL FULFILLMENT OF THE REQUIREMENTS
FOR THE DEGREE OF
DOCTOR OF PHILOSOPHY
IN THE SUBJECT OF
PHYSICS

HARVARD UNIVERSITY
CAMBRIDGE, MASSACHUSETTS
APRIL 2021

©2020 – POLNOP SAMUTPRAPHOOT
ALL RIGHTS RESERVED.

A quantum network node based on a nanophotonic interface for atoms in optical tweezers

ABSTRACT

Efficient interfaces between photons and memory qubits constitute fundamental building blocks for quantum networking and large-scale quantum information processing. Our approach utilizes a photonic crystal cavity to realize such optical interfaces for atoms in optical tweezers. With this platform, we observe strong coupling between two atoms mediated by the cavity. Combining this observation with coherent manipulation and non-destructive measurements, we implement a protocol for generating Bell pairs that remain entangled when transported away from the cavity structure. These results present prospects for building integrated optical interconnects for neutral atom quantum information processors, adding capabilities such as rapid non-destructive readout and flexible connectivity to the rapidly-growing platform.

Contents

1	INTRODUCTION	1
1.1	Background and Motivation	1
1.1.1	Quantum networks	1
1.1.2	Quantum interconnects with cavity QED	2
1.1.3	Nanophotonic interfaces between optical photons and neutral atoms	6
1.1.4	Quantum simulation	7
1.2	Overview of this thesis	8
2	STRONG COUPLING OF TWO INDIVIDUALLY CONTROLLED ATOMS VIA A NANOPHOTONIC CAVITY	11
2.1	Introduction	11
2.2	Description of the experiment	13
2.3	Single-atom reflectivity response	16
2.3.1	Single-shot detection	18
2.4	Controlling two atoms near a photonic crystal cavity	18
2.5	Collective linewidth enhancement	21
2.6	Reflectivity response in the dispersive regime	21
2.6.1	Spectroscopic signature of coupling between atoms	23
2.7	Summary and outlooks	23
3	A NANOPHOTONIC INTERFACE FOR TRANSPORTABLE ENTANGLED ATOMS	27
3.1	Introduction	27
3.2	Nanophotonic interface for atoms in tweezers.	29
3.3	Coherent control near the nanostructure	32
3.4	Entanglement generation	35
3.5	Entanglement transport	37
3.6	Conclusion and outlooks	38
4	CONCLUSION	42
	APPENDIX A APPARATUS AND METHODS USED IN CHAPTER 2	48
A.1	Apparatus	48
A.2	Photonic crystal cavities	50

A.2.1	Design and fabrication	50
A.2.2	Frequency stabilization of the cavity	51
A.3	Experimental sequence	52
A.4	Individual tuning of the atomic resonances	56
A.5	Theoretical models	58
A.5.1	Atomic motion in the cavity mode	60
A.5.2	Cooperativity estimation	62
APPENDIX B APPARATUS AND METHODS USED IN CHAPTER 3		66
B.1	Cooperativity estimate	66
B.2	Experimental sequence	68
B.2.1	State preparation	71
B.2.2	Two-atom readout in free space	72
B.2.3	Readout through the cavity	75
B.3	Fidelity extraction from parity	75
B.4	Concurrence bound	77
B.5	Entanglement scheme using the interferometer	78
B.6	Theoretical models for the entanglement protocol	81
B.6.1	Coherent model	81
B.6.2	Mixed model	83
B.7	Coherence properties of atoms next to the photonic crystal cavity	86
B.8	Phase accumulation while moving	90
B.8.1	Dipole potential for different trap configurations	90
B.8.2	Differential light shift during the transport	92
B.8.3	Phase accumulation and cancellation	93
B.9	Modeling losses upon loading into the cavity near-field	96
APPENDIX C CONSTRUCTION OF AN ULTRA-HIGH VACUUM SYSTEM FOR INTEGRATION WITH NANOPHOTONICS		100
C.1	Device fabrication and characterization	101
C.2	Installation of a photonic crystal device in a vacuum system	102
C.3	Pump-down of the ultra-high vacuum system for atom trapping	103
APPENDIX D LASER SYSTEM FOR INDIVIDUAL ADDRESSING		107
D.1	List of laser systems	107
D.2	Experimental requirements for the individual addressing beams	108
D.3	Generation of laser frequencies	110
BIBLIOGRAPHY		112

TO MY PARENTS, NARIN AND CHUTIMA.

Acknowledgments

This work would not have been possible without support from a remarkable group of people. I am indebted to my advisor Misha Lukin for his ceaseless support to my growth as a scientist and as a person. I am grateful for his positive encouragement, for the freedom he has given his students to explore their ideas, for his boundless vision for quantum science, and for the scientific community he has nurtured. I am grateful to Vladan Vuletic for his continual mentorship since my undergraduate days at MIT. Vladan’s insightful comments always brought positive impacts, be it fresh perspectives on physical concepts or ideas to improve the experimental capabilities. I also thank Philip Kim for our conversations over the years, and for agreeing to serve on my committee.

From day one, I have been fortunate enough to be around many kind and brilliant scientists. I had the pleasure of working alongside Thibault Peyronel, Crystal Senko, Manuel Endres, and Sylvain Schwartz, all of whom guided me with their vast knowledge of atomic physics, experimental prowess, and exemplary characters. I also thank Tobias Tiecke, Jeff Thompson, and Kali Nayak for laying down the infrastructure we have been using for years.

Tamara Dordevic, Paloma Ocola, and Hannes Bernien joined soon after and made

tremendous contributions to the experimental advances towards coupling and entangling two atoms. Tamara and Paloma brought with them enormous energy and enthusiasm, carrying these difficult experiments through to fruition. I thoroughly enjoyed learning from them and sharing our fun times in and out of the lab. Hannes is a problem-solver, a listener, and a role model. His approach to simplifying and reorganizing the experiment helped us maintain our clear goal amid uncertainties. Later on, we were joined by Brandon Grinkemeyer and Ivana Dimitrova, both of whom brought incessant streams of ideas along with their technical mastery. I am excited that the future of this project is in the hands of these very capable and passionate people.

A large portion of the work presented in this thesis was carried out remotely during the pandemic. This is made possible thanks to the dedication of a special group of people. I thank Elana Urbach, Sam Dakoulas, Tamara Dordevic, Sepehr Ebadi, Giulia Semeghini, and the other members of the Lukin critical support team for helping keep our experiments alive. I also thank Misha Lukin and John Doyle for their leadership during this difficult time, ensuring smooth operation of the apparatus while putting our safety first.

The Lukin group offers unlimited sources of wisdom and laughter. Working at the intersection between atomic physics and nanophotonics puts me in a unique position to seek help from many other group members. Countless times, I have drawn from the expertise of the Rydberg array team and the silicon-vacancy teams. I thank Daniel Assumpcao, Rivka Bekenstein, Mihir Bhaskar, Dolev Bluvstein, Sepehr Ebadi, Ruffin

Evans, Yan Qi Huan, Alex Keesling, Erik Knall, Can Knaut, Harry Levine, David Levonian, Bart Machielse, Christian Nguyen, Ahmed Omran, Ralf Riedinger, Giulia Semeghini, Alp Sipahigil, Pieter-Jan Stas, Pasha Stroganov, Denis Sukachev, and Tout Wang for their insights on atoms and cavities. I enjoyed my conversations about physics and various other topics over bagels and lunch with Johannes Borregaard, Alexei Bylin-skii, Maddie Cain, Iris Cong, Joonhee Choi, Soonwon Choi, Frankie Fung, Jan Gieseler, Oksana Makarova, Leigh Martin, Maya Miklos, Janos Perczel, Eric Peterson, Kristine Rezai, Emma Rosenfeld, Arthur Safira, DaLi Schaefer, Tamara Sumarac, Elana Urbach, Aditya Venkatramani, Harry Zhou, Leo Zhou, among many others. I would like to especially thank Sasha Zibrov for his extraordinary expertise on hands-on techniques, Stan Cortreau for his guidance in the machine shop, Adam Ackerman, Sam Dakoulas, Carol Davis, Silke Exner, and Clare Ploucha for their generosity with their administrative help, and finally Jacob Barandes and Lisa Cacciabuado for helping me navigate through my PhD journey.

The CUA community has been home for me for almost a decade. I enjoyed stimulating and entertaining discussions with Boris Braverman, Sergio Cantu, Dorian Gangloff, Jonathan Hood, Nick Hutzler, Rajibul Islam, Akio Kawasaki, Lev Kendrick, Joyce Kwan, Lee Liu, Yu Liu, Hyungmok Son, Eric Tai, Wenchoao Xu, Yichao Yu, Kenneth Wang, Jessie Zhang, among many others. I will remember the positivity that my buddies Eric Peterson, Lin Su, and Zhongying Yan, brought to our midweek lunch and cannoli breaks.

Most importantly, I would like to thank my parents Chutima and Narin, my brothers Tay and Baiboon, and my partner Pantra, for the unwavering and unconditional support throughout this journey. This thesis is dedicated to them.

Citations to previously published work

Parts of this dissertation cover research reported in the following articles:

Chapter 2 in its entirety, has been published as

“Strong coupling of two individually controlled atoms via a nanophotonic cavity”, P. Samutpraphoot, T. Tamara Dordevic, P. L. Ocola, H. Bernien, C. Senko, V. Vuletic, M. D. Lukin, *Physical Review Letters*, 124, 063602 (2020).

The material contained in Chapters 3 is currently in preparation for publication.

1

Introduction

1.1 Background and Motivation

1.1.1 Quantum networks

The field of quantum information science has garnered increasing attention in the past decade. This is in large part due to its promising advantages in various applications ranging from solving complex problems in many-body physics [1] and quantum chemistry [2, 3], to metrology [4] and secure communication [5]. There have been rapid technological advances that enable an unprecedented degree of control of quantum systems. As these quantum systems are growing larger and more complex, the demand for interfaces between different systems becomes increasingly imminent [6, 7].

The purpose the work presented in this thesis is to link quantum systems together

under the framework of quantum networks and is motivated by applications in multiple disciplines. In quantum communication, parties may securely transfer information over a distance, and several protocols have already demonstrated its advantages over classical communication [8, 9, 10]. Quantum systems may also be linked to collectively perform quantum-enhanced tasks. Multiple near-term quantum computers with several hundred qubits may be connected to make up a more powerful quantum computer in a modular architecture, just as data centers and supercomputers comprise a multitude of linked information processing modules [11, 12, 13, 14]. Quantum sensors can also benefit from enhanced performances when operating in networks. Networks of atomic clocks can maintain, synchronize, and safeguard the time standards across parties [15] and entanglement can improve interferometry in telescope arrays, refining resolution in astronomical imaging. [16, 17].

1.1.2 Quantum interconnects with cavity QED

The standard architecture of quantum networks consists of nodes of memory qubits, or quantum systems, that are linked by communication channels [5, 18]. Optical photons make an excellent candidate for information carriers, flying qubits, that propagate in the channels. Compared to microwave photons, optical photons experience low propagation losses and are robust against thermal environments. They can be sent across distances in free space or guided in networks of optical fibers or on-chip photonic circuits and can

be naturally interfaced with emitters. While fiber optics is a standard technology the internet is built upon, fiber attenuation in fiber cores is nevertheless finite (~ 0.5 dB/km at 1550 nm), thereby exponentially suppressing signal strengths with distance. In classical communication, this problem can be mitigated by placing repeaters along the channel to restore the signal by means of amplification. The no-cloning theorem forbids quantum information from being copied in this manner, and quantum repeaters have instead to rely on entanglement swapping operations. This can improve the scaling of the success probability to polynomial [19].

The primary challenge for building a quantum repeater is the quest for a well-controlled quantum system that is sufficiently decoupled from the environment, and the demonstration of a fully-functional quantum repeater has yet to emerge. In particular, the system must satisfy the primary requirements: the long memory time of the stationary qubits, the ability to perform local multi-qubit gate within a node, and an efficient interface between the memory and flying qubits [20, 21].

While various platforms have excelled in retaining long memory and high-fidelity multi-qubit operations, realizing an efficient interfaces is a challenging task. One way to realize such architecture is to combine photons and optical emitters into hybrid systems under the framework of cavity quantum electrodynamics (cavity QED, or cQED). By placing optical emitters inside a resonator, the interactions between the emitters and the optical field confined by the resonator become coherently enhanced. When combined with emitters with long-lived and controllable internal degrees of freedom, a cavity

QED system satisfies these requirements and enables efficient protocols for operations in quantum networks and quantum information processing.

There is a wide variety of emerging candidates for cavity QED systems, constructed with different combinations of optical emitters and resonators. The field of cavity QED was originally envisioned with neutral atoms in macroscopic cavities. Early cavity QED experiments were carried out with atomic beams passing through high-finesse Fabry-Perot cavities [22]. Decades later, with the advent of the technology for atom trapping and cooling, single atoms can be held inside macroscopic cavities long enough for operations of elementary quantum protocols [23, 24, 25].

Solid-state systems, such as color centers in diamond, also exhibit a combination of these desirable properties, namely narrow optical transitions [26, 27, 28], long-lived spin degrees of freedom [29, 30, 31], and compatibility with micro- and nanoscale optical cavities [32, 33, 34, 35, 36]. There has been remarkable progress towards developing efficient integrated quantum networks with these systems [37], and elementary networking protocols have been demonstrated [38, 8, 39].

While many of the cold-atom and solid-state systems operate in the visible or near-infrared regime, efforts have been made to study emitters in the telecommunication band, which offers compatibility with the current technology in photonics such as fiber optic networks and on-chip silicon-based devices. Several solid-state systems such as rare-earth ions residing in crystalline host materials have recently been demonstrated to have good optical properties [40, 41], long memory times [42], and integration to

nanophotonics and fiber-based devices [43, 41, 44, 45]. In addition, several proposals have shown that telecom-wavelength transitions in neutral atoms can be accessed in alkaline-earth species and in alkali species with fast pulses [46, 47].

Another platform that has emerged as a leading technology for quantum computing is superconducting qubits, with various quantum advantages already demonstrated [48, 2]. The technology is based on circuit QED, a closely-related variant of cavity QED, and one may consider implementations of quantum networks with the strong interface between microwave photons and artificial atoms. However, the platform is currently facing two challenges, namely the lack of optical interfaces and the short coherence times. The operation in the microwave domain is not suitable for long-distance quantum networks due to thermal noise, and previous work has addressed the first challenge by transducing microwave quantum signals to optical photons [49]. In order to realize practical applications such as entanglement generation between distant superconducting qubits via optical photons, the current transduction efficiency $\sim 10^{-3}$ must be improved while maintaining low-noise operation. To address the second challenge, there has been a steady improvement to the qubit coherence, but the state-of-the-art memory time of a millisecond [50, 51, 52] is still shorter than signal propagation delays at the global scale.

1.1.3 Nanophotonic interfaces between optical photons and neutral atoms

Our approach makes use of distinct advantages of neutral atoms and combine them with optical interfaces provided by nanophotonic devices. Neutral atoms naturally exhibit good coherences and a high degree of controllability. Various techniques have been developed for controlling both their internal and external degrees of freedom with electromagnetic fields. Single neutral atoms can be isolated in tightly focused optical tweezers, which can be individually steered for atom transport [53, 54, 55, 56, 57, 58] and cooled to their motional ground state with laser fields [59, 60]. The internal states can be initialized optically and driven with high fidelity. Atoms of the same isotope are identical, making them suitable for applications requiring frequency standards and eliminating the need for individual frequency tuning.

The excellent intrinsic atomic properties and the degree of controllability, when combined with the strong interactions such as the Rydberg interactions, result in the rapid progress of the platform with various applications ranging from quantum simulation of many-body dynamics [61, 62, 63], atomic clocks [64, 65], high-fidelity quantum information processing [66, 67, 68]. In pursuit of quantum networks, not only do we seek to exploit these excellent capabilities of the tweezer array technology, but this otherwise rapidly-developing platform will also benefit from additional features, such as rapid non-destructive readout and flexible connectivity, provided by integrated optical

interconnects.

The remaining crucial component of our approach is the nanophotonic platform, which offers distinct advantages to macroscopic optical devices for a number of reasons. First, confining photons within a sub-wavelength scale results in increased coupling strength with atoms that experience the cavity field because the single-photon electric field $E = \sqrt{\hbar\omega/\epsilon_0 V}$ gets larger with a smaller mode volume V . Second, the small footprint of the structure introduces minimal perturbation to an atomic physics apparatus, allowing optical access for trapping and cooling. Third, nanofabricated devices present good prospects for scalability as hundreds of them can be produced on the same chip. Finally, multiple devices can be integrated into fiber networks or photonic integrated circuits on-chip.

Nanophotonic devices have been naturally integrated with solid-state systems such as quantum dots [69] or rare-earth ions [43], and several experimental efforts have combined a cold atom system with a variety of device designs and geometries ranging from nanofibers [70, 71] to photonic crystal waveguides [72], and more recently to on-chip micro-ring resonators [73].

1.1.4 Quantum simulation

With the vast variety of design possibilities, the applications of the platform is not necessarily limited to quantum networks. The strong atom-light interactions near the

device can be used to probe novel phenomena that emerge in this hybrid system such as atom-photon bound states and spin-motion entanglement enabled by the fast-varying mode field in nanoscale devices [74]. More generally, the platform is ideal for building quantum simulators to study many-body physics with light-mediated interactions, of which the range can be tuned by engineering the photonic band [75].

1.2 Overview of this thesis

Built upon previous results on observations of coupling between single atoms and a photonic crystal cavity [76] and its applications to realize a phase switch between single atoms and photons [77], the work presented in this thesis is an extension to multi-qubit operations (Fig. 1.1). We show that two atoms can strongly couple to each other via interactions mediated by photons in the nanophotonic cavity, become entangled upon a projective measurement through the efficient optical interface, and remain entangled when transported away from the nanostructure.

In chapter 2, we present a series of experiments leading to observations of atom-atom coupling. We discuss the essential ingredients to these observations, from the efficient atom-photon interface to individual control of the individual atoms. The figure of merit for the atom-photon interface is characterized by the cooperativity extracted from the reflection spectrum of the atom-cavity system. The individual control is enabled by the spatial separation of the tweezers, leaving direct access for individual addressing

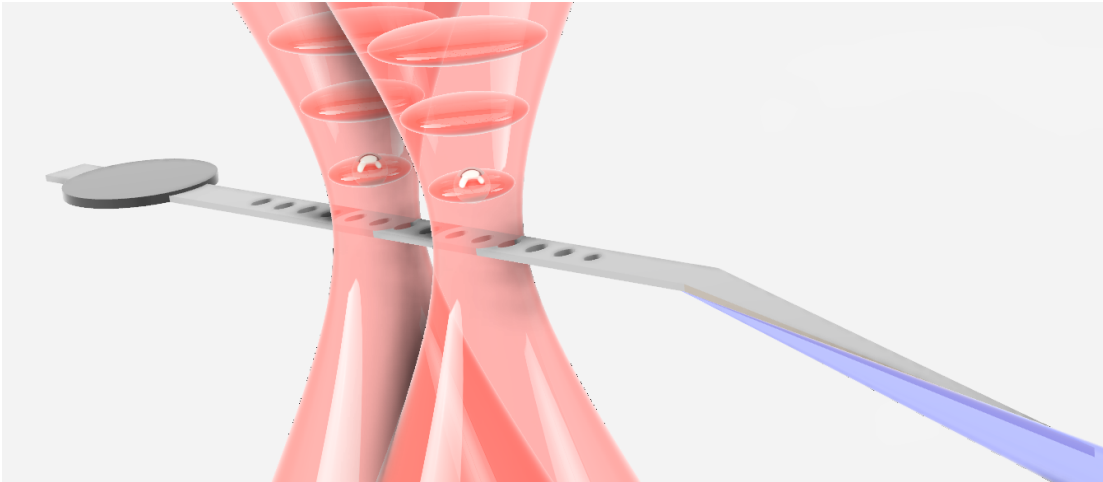


Figure 1.1: **A nanoscale interface between two atoms and nanophotonics.** Two rubidium atoms are trapped in optical tweezers near a photonic crystal waveguide cavity. The cavity is suspended at the tip of a tapered fiber, serving as an efficient interface between the system and external networks of fiber optics.

beams. The reflectivity measurements are well-described by a model that takes into account position fluctuations due to effects such as the thermal motions of the atoms. Collective coupling manifests in line broadening in the resonant regime and doubling in the cavity-induced line shift in the dispersive regime. When the optical transitions of the two atoms are tuned into resonance with each atom, the coupling of each atom to the common cavity mode results in a coherent interaction between them, leading to the formation of dark and bright two-atom states.

In chapter 3, we address the unique capabilities for coherent manipulation of two atomic qubits near the nanostructure. In addition to the efficient optical readout, our system showcases high-fidelity initialization and microwave control on the long-lived

qubit states. We discuss single-qubit coherence properties near the nanostructure and when moved away from it. The decoherence due to inhomogeneity accrued through transport can be recovered with dynamical decoupling. Combining these capabilities, we have performed an entanglement protocol heralded by single photons and observed a Bell state of two atoms. Employing dynamical decoupling and encoding the qubits into long-lived states, we show that the entangled state can be moved out of the cavity and remains entangled. These results enable the optical interface to be integrated with a larger system of tweezer arrays, paving the way for creating many-body entangled states of atoms and photons and scaling up neutral atom quantum information processors with better connectivity.

Finally, we conclude in chapter 4 with a summary of the work presented in this thesis and an outlook for future work. In particular, we highlight some of the key opportunities and challenges towards realizing quantum networks and interfaces with full-scale Rydberg array with our platform and describe how these challenges may be met.

2

Strong coupling of two individually
controlled atoms via a nanophotonic
cavity

2.1 Introduction

We demonstrate photon-mediated interactions between two individually trapped atoms coupled to a nanophotonic cavity. Specifically, we observe collective enhancement when the atoms are resonant with the cavity, and level repulsion when the cavity is coupled to the atoms in the dispersive regime. Our approach makes use of individual control over the internal states of the atoms, their position with respect to the cavity mode, as well

as the light shifts to tune atomic transitions individually, allowing us to directly observe the anti-crossing of the bright and dark two-atom states. These observations open the door for realizing quantum networks and studying quantum many-body physics based on atom arrays coupled to nanophotonic devices.

Controlled interactions between individual photons and quantum emitters are an important ingredient for the realization of scalable quantum information systems [78, 18]. Nanophotonic devices in which the light is confined to sub-wavelength dimensions constitute a promising approach for engineering strong light-matter coupling [69, 74]. The appeal of a nanophotonic platform is due to two key features. On one hand, nanophotonic devices allow the photonic dispersion to be tailored to achieve tunable-range interactions between coupled emitters [79, 80, 76, 81, 82, 83] and engineer a range of interaction Hamiltonians [75, 84]. On the other hand, the nanoscale mode volume enables an efficient high cooperativity emitter-photon interface suitable for realizing potentially scalable systems [85, 86, 20, 19]. In particular, cold neutral atoms have recently emerged as a promising approach for realizing large-scale quantum systems due to the ability to generate large numbers of identical, individually trapped atoms [53, 54, 53, 55, 56, 57, 58]. While significant effort is currently being directed towards coupling multiple isolated atoms to nanophotonic systems [87, 73, 71, 76], achieving a strong coupling of a deterministic number of atoms remains a challenge. The atoms must be trapped closely enough to the device to maximize the coupling within the evanescent field, while overcoming attractive surface forces [88, 89], and preserving the excellent

atomic coherence properties.

In this Chapter, we report on the observation of strong coupling of two individually controlled atoms via a nanophotonic cavity. In particular, we spectroscopically demonstrate collective enhancement in the resonant regime, and level repulsion in the dispersive regime. These experiments utilize individual control of the positions of the atoms with respect to the cavity mode, their internal states, and the frequencies of their transitions. This allows us to observe the anti-crossing of the bright and dark two-atom states, in analogy to prior observations involving superconducting qubits and color centers in diamond [90, 91].

2.2 Description of the experiment

Our experiments utilize a cavity QED system consisting of ^{87}Rb atoms coupled to the evanescent field of a photonic crystal (PC) cavity (Fig. 2.1a, b) [76]. The SiN nanophotonic device is suspended in a vacuum chamber on a tapered optical fiber, which is also used for efficient interrogation of the cavity by exciting and collecting photons through its fiber-optic interface [92]. This approach minimizes the physical footprint of the system, thus allowing for good optical access and unobstructed trapping and cooling while retaining the flexibility to control the atomic position and confinement. The atoms are trapped using tightly focused optical tweezers that localize them to within tens of nanometers and can be steered to desired locations. The internal states of the atoms

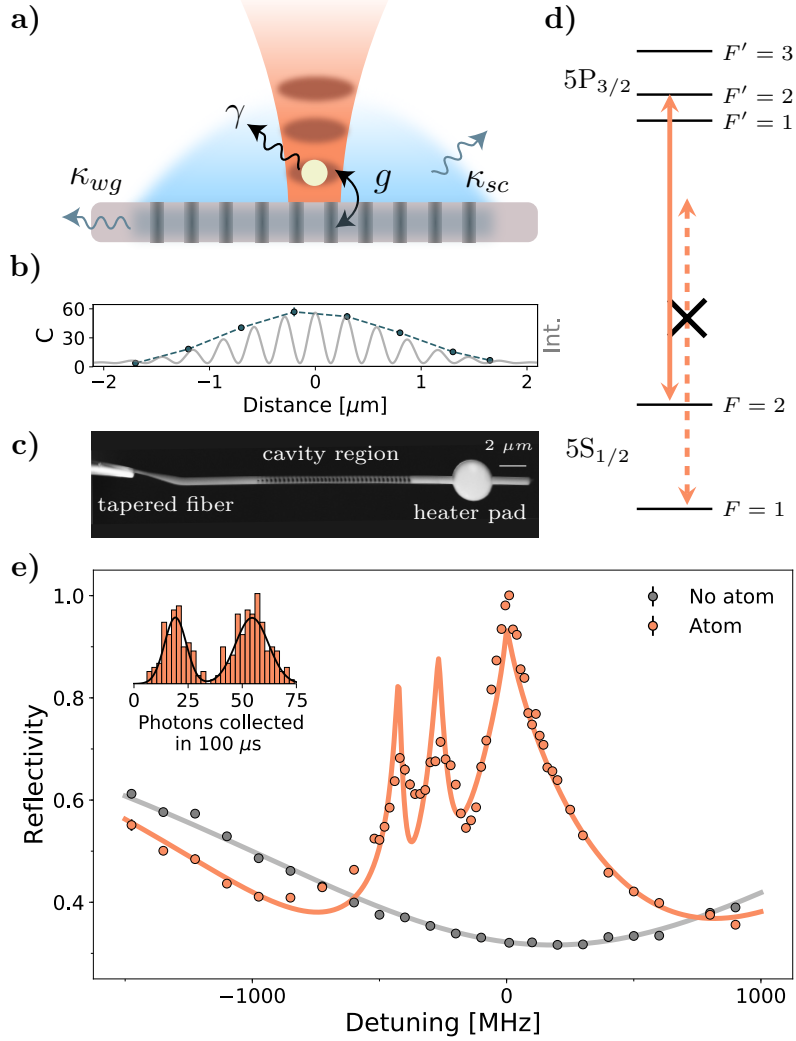


Figure 2.1: High cooperativity atom-photon coupling to a nanophotonic cavity. **a)** Schematic of the experimental setup, showing an atom trapped in the lattice of an optical tweezer coupled to a nanophotonic cavity. The parameters are defined in the main text. **b)** Moving the tweezer along the cavity to map out the mode in terms of cooperativity (blue) and simulated intensity profile of the cavity mode (gray). **c)** SEM image of the nanophotonic cavity suspended on a tapered fiber. **d)** Level diagram for the $5S_{1/2} \rightarrow 5P_{3/2}$ transition. The $F = \{2, 1\}$ manifold is $\{\text{coupled, uncoupled}\}$ to the cavity. The probe detuning is defined relative to the bare $F = 2 \rightarrow F' = 3$ transition. **e)** Measured cavity reflection spectrum with and without an atom coupled to the cavity. The solid lines are from theoretical models. Inset: histogram of counts collected at 0 MHz detuning, showing single-shot atomic detection. 14

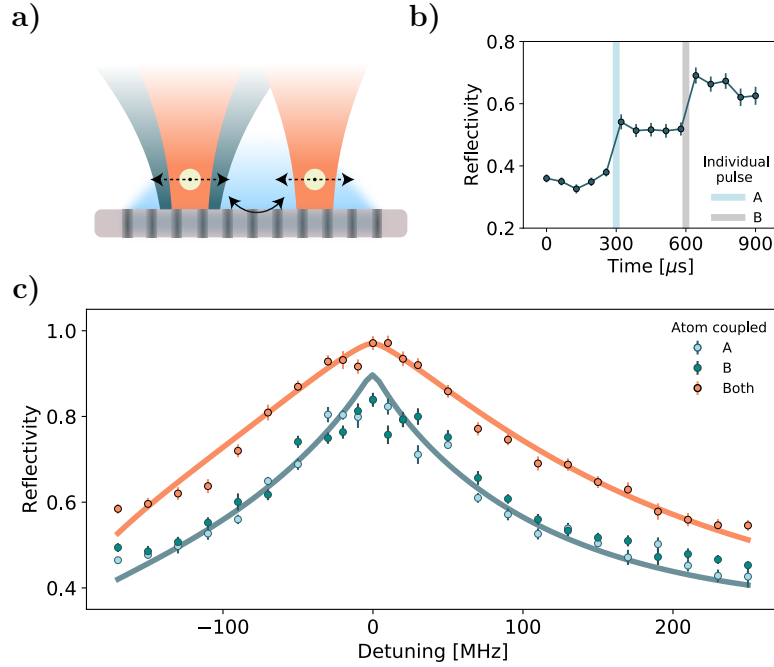


Figure 2.2: Individual control and resonant coupling. **a)** Illustration of the individual position and internal state control with a repumping (blue) beam co-propagating with one of the optical tweezers (orange). **b)** Average reflectivity jumps after pumping each atom to the $F = 2$ manifold, taken at the probe detuning of 100 MHz. **c)** Broadening of the $F = 2 \rightarrow F' = 3$ line. The labels {A, B} denote the atoms in the two tweezers. The spectrum is taken when the tweezers are positioned 1 μm away from the mode center to retain addressability. The solid lines are from theoretical models.

are individually manipulated with light fields co-propagating with the optical tweezers. We interrogate the response of the atom-cavity system by scanning the frequency of the probe field to measure the reflection spectrum. The frequency of the cavity is tuned thermally with a laser beam pointed at the heater pad (Fig. 2.1c).

2.3 Single-atom reflectivity response

We probe the atom-cavity spectrum by tuning the cavity to the $5S_{1/2} \rightarrow 5P_{3/2}$ transition at 780 nm. The spectrum is acquired by scanning the probe field from the ground state manifold $5S_{1/2}, F = 2$ across the excited state manifolds $5P_{3/2}, F' = 1, 2, 3$ (Fig. 2.1d), while the atom is positioned at the center of the cavity mode. We note that for all the spectra presented in this Letter, the probe detuning is relative to the bare $F = 2 \rightarrow F' = 3$ transition, and the error bars are obtained from statistical uncertainties acquired over multiple experimental runs.

Fig. 2.1e shows the reflection spectrum of the cavity with and without an atom present. For the case without an atom, the reflection spectrum is a resonance dip of the empty cavity. The presence of an atom drastically changes the spectrum, and we observe three atomic lines that are significantly broadened due to resonant coupling between the atom and the cavity. This effect is described by the Purcell enhancement. In the resonant regime, the radiative decay rate into the cavity mode is enhanced by the single-atom cooperativity $C = 4g^2/\kappa\gamma$, where g is the single-photon Rabi frequency, γ the atomic spontaneous decay rate. The cavity decays at the rate κ_{wg} into the waveguide and κ_{sc} elsewhere, yielding the total cavity decay rate $\kappa = \kappa_{wg} + \kappa_{sc}$ (Fig. 2.1a). The observed line-shape is accurately described using a model incorporating a distribution of cooperativities, rather than a single-valued one. Taking these considerations into account, we fit the spectrum in Fig. 2.1e and extract the average cooperativity $C = 71(4)$, corresponding

to the cavity QED parameters $\{2g, \gamma, \kappa_{wg}, \kappa_{sc}\} = 2\pi \times \{1.24(4), 0.006, 0.86, 2.77\}$ GHz.

We compare this to an independent theoretical estimate of g based on the geometry of the trapping potential of the tweezer and the evanescent field experienced by the atom. The closest lattice site is at a distance of 260 nm from the surface of the PC [76]. At this distance, an atom at rest experiences a single-photon Rabi of frequency $2g_0 = 2\pi \times 1.7$ GHz, or $2g = 2\pi \times 1.26$ GHz in the presence of position fluctuations (see Appendix A). This estimate is consistent with the single-photon Rabi frequency extracted from our experimental data.

Fluctuations in the atomic position across the spatially-varying cavity field leads to cooperativity distributions. The distribution of cooperativities that produces the spectrum in Fig. 2.1e corresponds to the atomic spatial widths of 190 nm along the PC and 33 nm along the direction of propagation of the tweezer. An independent temperature measurement yields an upper bound estimate of 120 μ K near the PC, accounting for 150 nm and 30 nm in the two directions respectively (see Appendix A). Other contributions include the pointing fluctuations of the tweezer. Both of these fluctuations affect the lineshapes of the spectra shown in this work and make the cavity standing wave profile unresolvable (Fig. 2.1b).

2.3.1 Single-shot detection

The efficient atom-photon interface allows us to determine the presence of an atom in a single shot. We tune the probe frequency to the $F = 2 \rightarrow F' = 3$ line and count reflected photons collected within $100 \mu\text{s}$ (Fig. 2.1e inset). When repeated multiple times, the photon number follows a bimodal normal distribution with 0.7% overlap, which is adequately separable to determine if the atom is coupled to the cavity. The atom becomes uncoupled from the cavity if it falls into the $F = 1$ manifold via off-resonant scattering. We deplete the population in the $F = 1$ manifold by sending in an additional beam co-propagating with the optical tweezer on the $5S_{1/2}, F = 1 \rightarrow 5P_{1/2}, F' = 2$ transition, at 795 nm, which is sufficiently detuned from the cavity and can be filtered out from the collected photons. In addition to the $F = 2 \rightarrow F' = 3$ line, the spectrum in Fig. 2.1e also shows the $F = 2 \rightarrow F' = 1, 2$ transitions, which are not cycling and would not be visible without applying the repumping beam.

2.4 Controlling two atoms near a photonic crystal cavity

The reflection spectrum is used to study the cooperativity dependence on experimental parameters such as the position of the atom. Taking advantage of the individual position control, we scan the tweezer position along the axis of the PC by steering the galvanome-

ter mirrors and acquire a spectrum associated with each position (see Appendix A). We then determine the cooperativity at each location from the Purcell-enhanced linewidth and find that the resulting cooperativity dependence (Fig. 2.1b, blue) traces out the envelope of the numerically simulated field profile intensity (gray).

Having characterized the single-atom coupling, we now turn to the case of two atoms to study their resonant coupling via the cavity (Fig. 2.2a). The two tweezers must be placed away from each other to avoid overlap and cross-talk, hence inevitably lowering their individual cooperativities. The experiments involving two atoms are operated with the tweezers placed $1 \mu\text{m}$ away from the mode center, corresponding to the average single-atom cooperativity $C = 31(2)$ (Fig. 2.1b, blue), well within the strong coupling regime.

In addition to the position control, the two-atom experiments also make use of internal state manipulation of individual atoms. This is achieved by having repumping beams co-propagating with the tweezers, selectively bringing the desired atom into the $F = 2$ manifold. We demonstrate this by applying $3 \mu\text{s}$ long repumping pulses at $300 \mu\text{s}$ on one tweezer and $600 \mu\text{s}$ on the other while constantly probing the spectrum with the probe blue-detuned to 100 MHz and monitoring the collected photon counts in time (Fig. 2.2b). The average collected counts step up following each pulse, indicating the influence of repumping the atoms one at a time. The capability of individual repumping is utilized for detection and postselection on having two atoms coupled to the cavity in each trial of the experiment (see Appendix A).

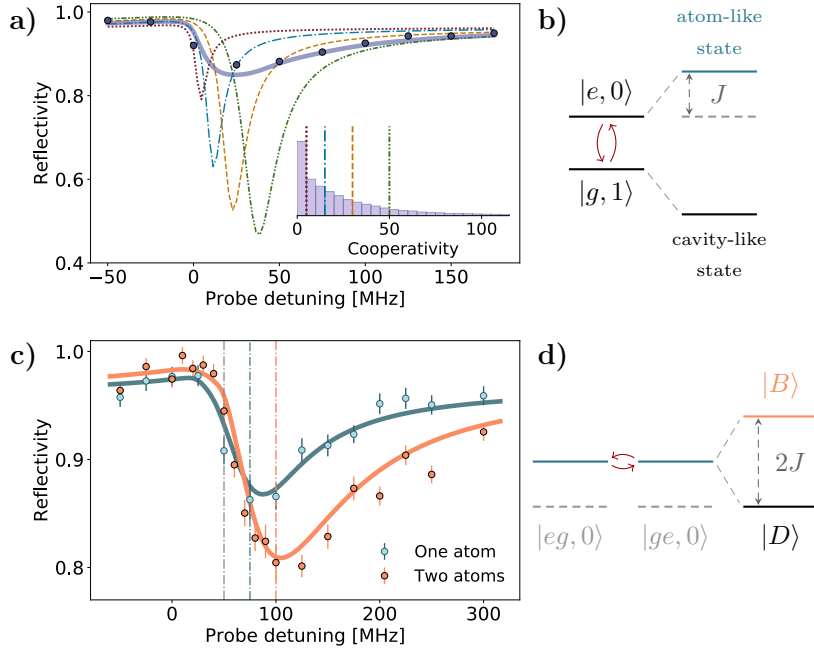


Figure 2.3: Atom-photon interaction in the dispersive regime. **a)** Atom-like spectrum of the $F = 2 \rightarrow F' = 3$ line at cavity detuning $\Delta = 2\kappa$. Theoretical curves (dashed-dotted) generated with single-valued cooperativities (vertical lines, inset). Theoretical curve (solid) constructed using cooperativity distribution (inset). This spectrum is acquired without a light shift from the tweezer. **b)** Level diagram of one atom in the singly-excited manifold. Bare states with {atomic, photonic} excitation $\{|e, 0\rangle, |g, 1\rangle\}$ are dressed by the atom-photon coupling $J = g^2/\Delta$ into the {atom, cavity}-like components. **c)** Single- and two-atom spectra when the two atoms are resonant with each other. The vertical lines delineate the frequency of an atom in a 50 MHz-deep tweezer not coupled to the cavity (gray) and the expected cavity-induced shifts of the {one, two} atom(s) coupled to the cavity {blue, orange}. **d)** Level diagram of two atoms. The two atom-like components hybridize into the {dark, bright} states $\{|D\rangle, |B\rangle\}$ which experience frequency shifts of $\{0, 2J\}$. The solid lines are theoretical models.

2.5 Collective linewidth enhancement

With these capabilities, we explore the collective behavior of two atoms simultaneously coupled to the cavity by acquiring a reflection spectrum centered on the $F = 2 \rightarrow F' = 3$ line (Fig. 2.2c, orange). We observe broadening of the spectrum in the two-atom case. The spectrum is well described by our theoretical model generated using the sum of individual cooperativities extracted from the single-atom spectra with no additional parameters (see Appendix A). We extract the full width at half maximum of $2\pi \times \{170, 300\}$ MHz for the case of {one, two} atom(s) coupled to the cavity. The effect of line broadening can be interpreted as a result of collective enhancement [87, 93].

2.6 Reflectivity response in the dispersive regime

The phenomena described above, such as the Purcell effect and collective enhancement, can also be demonstrated spectroscopically in the dispersive regime. We red-detune the cavity relative to the $F = 2 \rightarrow F' = 3$ line by $\Delta = 2\kappa$ and acquire a single-atom spectrum (Fig. 2.3a). We observe that the atomic line becomes narrower than the resonant case and experiences a frequency shift ¹. The shift is a result of the atom-cavity interaction in the dispersive regime (Fig. 2.3b). In this regime, the atom is dressed by the cavity coupling and experiences a frequency shift of $g^2/\Delta = C\kappa\gamma/4\Delta$ while its Purcell-enhanced linewidth is suppressed by a factor of $1 + 4\Delta^2/\kappa^2$.

¹The shift from 0 MHz detuning is observed in the absence of the light shift from the tweezer.

In the same manner as the resonant case, the experimental data cannot be adequately captured by theoretical curves (Fig. 2.3a, dashed-dotted lines) generated with single-valued cooperativities (Fig. 2.3a inset, vertical lines) but is rather well described using a model involving the cooperativity distribution shown in the inset of Fig. 2.3a. This distribution leads to varying frequency shifts, which result in additional broadening and modified lineshape.

The collective coupling in the dispersive regime can be characterized by probing spectra at a cavity detuning with one and two atom(s) at the same resonance frequency (Fig. 2.3c). The single-atom shift is consistent with the expected value of $J = 2\pi \times 25(4)$ MHz based on our average cooperativity estimate from the theoretical model describing the spectrum in Fig. 2.2c. The two-atom spectrum appears as a single line that experiences a shift twice as large as the single-atom line ².

The twofold enhancement of the frequency shift can be understood as level repulsion between the two collective atomic states (Fig. 2.3d). These states are the symmetric and antisymmetric superpositions of the two-atom states. The symmetric superposition interacts more strongly with the cavity due to constructive interference of coherent scattering into the cavity mode, thereby experiencing the frequency shift of $2g^2/\Delta$, and forming the bright state, $|B\rangle = (|eg,0\rangle + |ge,0\rangle)/\sqrt{2}$. The antisymmetric superposition does not interact with the cavity due to the destructive interference, acquires zero shift,

²The shifts are determined with respect to an offset of $2\pi \times 50$ MHz due to the light shift induced by the tweezer.

and forms the dark state $|D\rangle = (|eg, 0\rangle - |ge, 0\rangle)/\sqrt{2}$. The difference in their frequency shifts results in line-splitting which can be equivalently viewed as an interaction between two atoms with coupling rate $2J = 2g^2/\Delta$ due to an off-resonant exchange of virtual cavity photons [87].

2.6.1 Spectroscopic signature of coupling between atoms

We further illustrate the dynamics of level repulsion by tuning the atoms in and out of resonance with each other. The relative atom detuning $\delta_{AB} = \delta_A - \delta_B$, is tuned with the light shifts induced by the individual tweezers, in our case, within $2\pi \times (\pm 100 \text{ MHz})$ (Fig. 2.4a) (see Appendix A). As we tune from large δ_{AB} towards zero with both atoms coupled to the cavity (Fig. 2.4b, d), we observe avoided crossing in the two atom spectrum. The relative intensities of the lines are modified as the dark and bright components are mixed. At $\delta_{AB} = 0$, the dark component disappears, and the bright component experiences a twofold shift. The frequencies of the lines follow $\sqrt{(2J)^2 + \delta_{AB}^2}$ with the gap that signifies the coupling strength of $2J = 2\pi \times 50(8) \text{ MHz}$, in agreement with the theoretical analysis shown in Fig. 2.4c.

2.7 Summary and outlooks

The observations demonstrate a controllable high-cooperativity interface between atoms and photons, as well as between two atoms mediated by virtual cavity photons, namely

collective enhancement and anti-crossing. These results can be extended along several directions.

First, the photon-mediated interactions can be combined with coherent quantum control of the internal states of the atoms to implement quantum gates for state transfer and entanglement generation [94, 95, 96, 24]. As the errors of many of the protocols for these applications decrease with larger cooperativity, further improvement in cooperativity is an essential prerequisite for scalability. This may be achieved by positioning the atoms closer to the surface to access a larger field strength [97], improving the design and fabrication of the nanophotonic devices [98], or cooling the atoms for tighter localization with respect to the mode maxima [59, 60, 99]. Second, this approach offers a complete toolbox for controlling quantum many-body systems. The number of atoms can be scaled up by generating tweezer arrays [53, 54, 53, 55, 56, 57, 58]. The established techniques for assembling atom arrays can be combined with our approach for the individual addressing and light shift control and recently developed techniques for imaging an array on a nanophotonic structure [73]. Combining these capabilities with the ability to engineer band dispersion may allow for the exploration of novel many-body systems with extensive tunability. Finally, the efficient high-bandwidth atom-photon interface with individual atomic control is naturally suitable for realizing quantum networks with multi-qubit nodes [5, 16, 15]. The nanoscale interface also holds prospects of integration with modular architecture such as on-chip photonic circuits and fiber-optic networks for various applications ranging from quantum repeaters to distributed quantum computing

[100, 12].

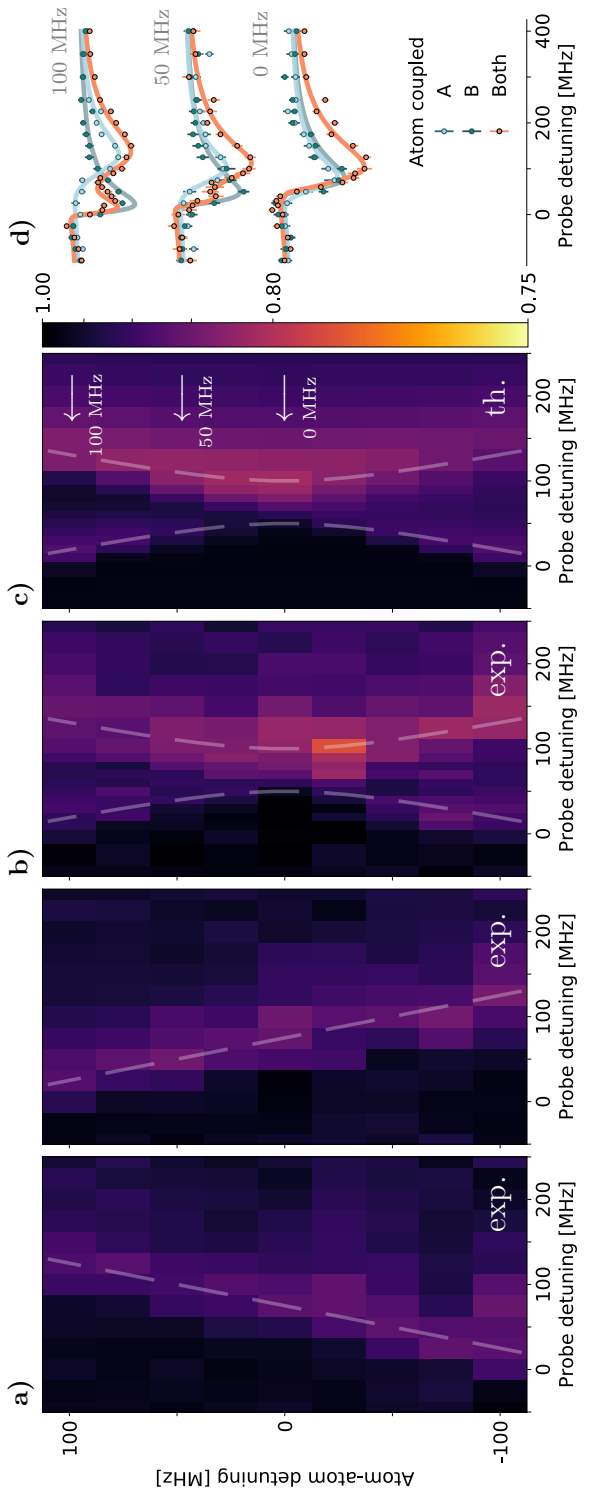


Figure 2.4: Level repulsion of the atomic lines induced by the cavity-mediated interaction. Experimental data of reflectivity map over probe detuning and relative atom detuning δ_{AB} for **a)** individual atoms coupled to the cavity, plotted with their expected light shifted frequencies (dashed lines) and **b)** two atoms simultaneously coupled to the cavity, plotted with frequencies of the bright and dark states (dashed lines), showing level repulsion. **c)** Theoretical calculation for two atoms simultaneously coupled to the cavity. **d)** Cross-sections of the reflectivity map showing single-atom and two-atom spectra at $\delta_{AB} = 2\pi \times \{0, 50, 100\}$ MHz indicated by the white arrows in **c**), plotted with theoretical models (solid lines).

3

A nanophotonic interface for transportable entangled atoms

3.1 Introduction

Realization of an efficient quantum optical interface for multi-qubit systems is an outstanding challenge in science and engineering. We demonstrate a method for interfacing neutral atom arrays with optical photons. In our approach, atomic qubits, trapped in individually controlled optical tweezers, are moved in and out of the near-field of a nanofabricated photonic crystal cavity. With this platform, we demonstrate full quantum control, efficient quantum non-demolition readout and entanglement of atom pairs strongly coupled to the cavity. By encoding the qubits into long-lived states and employ-

ing dynamical decoupling, the entangled state is transported away from the cavity and verified in free space. A combination of a compact, integrated optical link and entanglement transport paves the way for quantum networking with neutral atom quantum processors. A number of promising quantum systems are currently being developed, capable of high-fidelity control and manipulation of dozens of coherent quantum bits [101, 102, 103, 104]. Many potential applications of such systems, ranging from quantum networking to modular quantum computing architectures, require a mechanism for transferring qubit states to optical photons without compromising the ability for multi-qubit control [12, 105]. Neutral atom arrays have recently emerged as a powerful platform for quantum simulations and quantum information processing [104, 106, 107, 108, 109, 110]. In such systems, atom trapping, coherent control and readout is enabled by optical beam arrays, whereas high-fidelity multi-qubit quantum gate operations are enabled by coherent excitation into atomic Rydberg states. To enable quantum networking applications, platforms based on tweezers would need to be integrated with optical interfaces, most commonly implemented as optical cavities [111, 18]. Optical cavity QED systems have demonstrated atom-photon entanglement generation and distribution [77, 18]. However, their integration with atom arrays has remained a challenge due to simultaneous requirements of a small physical footprint, switchable efficient atom-photon interactions and good coherence properties.

In this Report, we experimentally demonstrate a system with a micrometer-size photonic crystal cavity (PCC) coupled to neutral atoms in movable optical tweezers that

can perform high-fidelity single qubit control and measurements as well as generate two-atom entanglement. By moving the individual atoms to and from the near-field of the PCC, this system can be integrated with quantum simulators and quantum information processors based on atom arrays (Fig. 1A). As a step towards this goal, we demonstrate that an entangled state of atoms can be moved away from the PCC and subsequently manipulated and measured. Previous studies have demonstrated coupling between atoms and PCCs [112, 113, 114], but entangled states have not been created and verified. Separately, coherent free space transport of atoms in tweezers was investigated [115, 116]. Here, we extend the previous work and demonstrate both entanglement generation and transport by engineering a compact high-cooperativity photonic node, encoding the qubits into field insensitive states, and utilizing dynamical decoupling sequences synchronized with the atomic transport.

3.2 Nanophotonic interface for atoms in tweezers.

In our experiments two ^{87}Rb atoms are trapped in individually controlled optical tweezers and coupled to a PCC, suspended on an optical fiber leading out of a vacuum chamber (Fig. 1A). The PCC confines single photons to a mode volume $V_m \sim 0.4\lambda^3$, enabling high atom-photon cooperativity [113]. The size of a nanophotonic cavity, more

than three orders of magnitude smaller than of a traditional Fabry-Perot mirror cavity, makes PCCs appealing for integration with atom arrays because the small footprint introduces minimal perturbation. Additionally, the small transverse size allows for switching the photon interactions on and off by simply moving the trapped atoms in and out of the cavity near-field. The atoms are trapped in the near-field by a standing wave created with the retro-reflection of the tweezer, and are confined 260 nm above the PCC surface (see Fig. 1A) [117, 77, 114, 118]. Using polarization gradient cooling in parallel with the tweezer transport, each free space atom is loaded into the near-field with 80% efficiency. The qubits are encoded in the hyperfine ground states as $|0\rangle \equiv |F = 1, m_F = 0\rangle$ and $|1\rangle \equiv |F = 2, m_F = 0\rangle$. The PCC is tuned to be resonant with the $5S_{1/2}, F = 2 \rightarrow 5P_{3/2}, F' = 3$ optical transition. For this transition, we extract the cooperativity from the reflection spectrum and obtain $C = 4g^2/(\kappa\gamma) = 27(1)$, corresponding to cavity QED parameters of $(2g, \gamma, \kappa) = 2\pi \times (786, 6, 3800)$ MHz. Fig. 1B shows the comparison between the reflection spectrum with and without an atom coupled to the cavity. The drastic difference in reflectivity can be used for non-destructive state readout to distinguish between the atoms in the uncoupled $F = 1$ and the coupled $F = 2$ manifolds, and to realize efficient atom-photon logic gates [77, 119]. By measuring the number of the reflected photons over 25 μ s interval, we perform a single shot readout of individual atoms with a fidelity of 0.95(3). When two atoms are present, this readout distinguishes the two-atom uncoupled state $|00\rangle$ from the other two-qubit states (Fig. 1C).

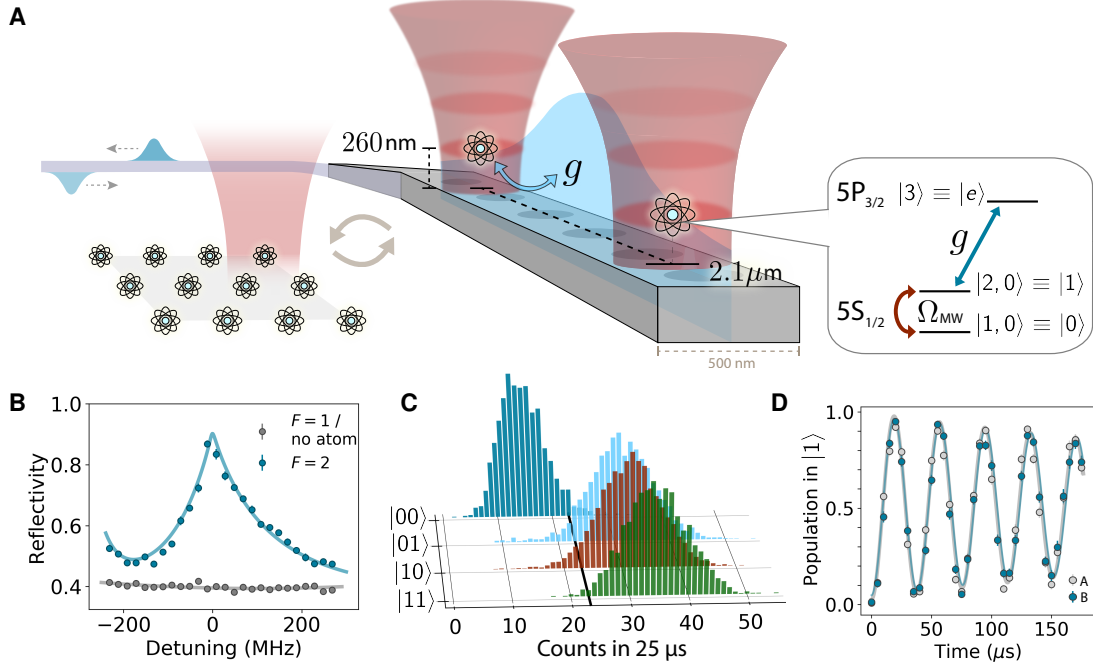


Figure 3.1: Nanophotonic interface for atoms in tweezers. (A) The nanophotonic cavity as a quantum optical interface for atom arrays. Two atoms are trapped in individual tweezers, and can be moved between the cavity near-field and the free space. The cavity is coupled to an optical fiber which can serve as a long-distance photonic link. (B) Cavity reflection spectrum for an atom in a strongly coupled state (blue) and an uncoupled state (grey), from which we extract cooperativity $C = 27(1)$. (C) Readout of different two-qubit basis states using the reflected photon counts. State $|00\rangle$ is distinguished from the other states with fidelity $\mathcal{F} = 0.95(3)$. The atoms, cavity and probe are on resonance. (D) Rabi oscillations showing that the qubit states can be prepared and coherently rotated while in the cavity near-field with a π pulse fidelity $\mathcal{F}_\pi = 0.946(3)$ and the same Rabi frequency for the two atoms.

3.3 Coherent control near the nanostructure

We next explore the coherence properties and control of the atomic qubits. In order to coherently move atoms between the near-field of PCC and free space, their coherence needs to be preserved over a timescale of milliseconds. In our system, the dominant dephasing mechanism is due to the effective magnetic field originating from vector light shifts in optical tweezers [60]. To the leading order, this mechanism is eliminated by encoding the qubits in the Zeeman-insensitive hyperfine sublevels. Using Raman-assisted state preparation (see Appendix A), we initialize an atom in $|0\rangle$ with fidelity $\mathcal{F}_{OP} = 0.98(2)$ and perform qubit rotations with a global microwave field (Fig. 1D). The qubit's coherence time T'_2 is extracted both in the near-field and in free space using a spin-echo sequence ($\pi/2 - \tau - \pi - \tau - \pi/2(\phi)$), yielding $T'_2 = 2.1(1)$ ms and $T'_2 = 9.7(8)$ ms, respectively (Fig. 2A). In the field-insensitive basis, the coherence is typically limited by the thermal motion that samples varying differential AC Stark shift in the trap [120, 121], a model consistent with our measured T'_2 in free space and the trap parameters. The T'_2 at the PCC is likely further reduced by heating, that may be intrinsic to the near-field trapping geometry [122, 118]. Nevertheless, the coherence time at the PCC allows for a protocol length equivalent to 100 microwave π pulses.

Preserving atomic coherence during transport poses additional challenges due to changes in the differential AC stark shift caused by moving from one trapping configuration to another. We measure this change along the $\sim 1 \mu\text{m}$ path from the PCC

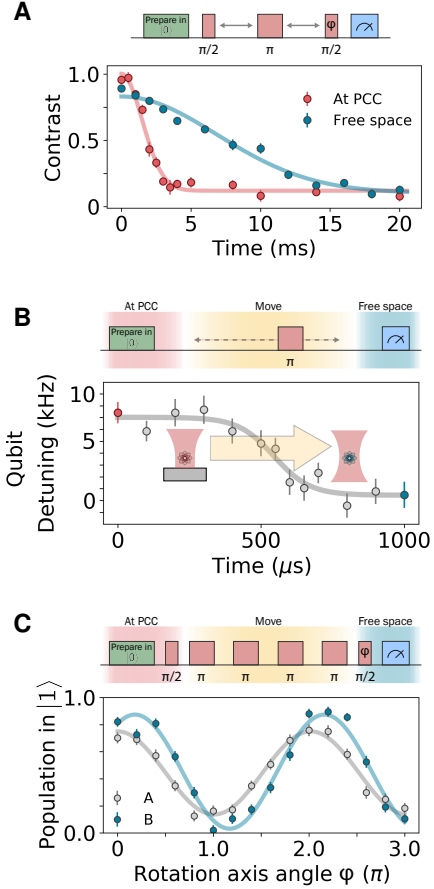


Figure 3.2: Qubit coherence during the transport between the cavity and the free space. (A) Measurement of the irreversible dephasing time in a spin echo sequence for stationary traps at the PCC (red, $T'_2 = 2.1(1)$ ms) and in free space (blue, $T'_2 = 9.7(8)$ ms). (B) Spatial dependence of the qubit frequency during the transport due to the deformation of the trapping potential which causes differences in the light shift. Changes in the qubit frequency can lead to additional dephasing. (C) Single atom coherence for atoms in the two traps (labelled A, B) after transport measured in a Ramsey-type sequence. Light shift variations are largely echoed out with a four-pulse Carr-Purcell sequence symmetric with respect to the profile of the qubit frequency during transport.

by applying a microwave pulse at various times along the trajectory, thereby measuring the instantaneous qubit frequency (see Appendix A). From the obtained ramp profile in Fig. 2B we estimate the minimal time of $650 \mu\text{s}$ to move the atom completely away from the PCC, limited by the mechanical response bandwidth of the scanning mirrors. Fluctuations in the atom trajectory can lead to additional dephasing, which we circumvent by using a Carr-Purcell decoupling pulse sequence [123]. The pulse sequence $(\pi/2 - (\tau - \pi - \tau)^N - \pi/2)$ begins with the atom in a superposition at the PCC and is followed by $N \pi$ pulses applied in parallel with its transport. The sequences with an even N perform better in recovering the Ramsey signal due to the symmetry of the ramp profile in Fig. 2B (see Appendix A). With an optimal $N = 4$, we retain 0.64(3) and 0.88(5) of the initial coherence for the traps A and B, respectively (Fig. 2C). We ascribe the difference between the two traps to the extra fluctuation in the scanning mirror for trap A, given that the traps are otherwise uniform (see Appendix A). For a stationary atom, $N = 4$ gives $T'_2 = 4.9(4) \text{ ms}$ ($17(2) \text{ ms}$) for atoms at (away) from the PCC, indicating that the coherence for trap B is nearly T'_2 -limited. In addition to the decoherence, in our parameter regime, each atom has a $\sim 15\%$ chance of being lost on the way out of the PCC. When we perform free-space readout, we correct for this loss (see Appendix A).

3.4 Entanglement generation

Having demonstrated coherent transport of single-atom states, we explore the ability to create and distribute an entangled state of two atoms generated using the cavity. We first create a two-atom Bell state using a "cavity carving" protocol [124, 125, 96]. This approach consists of the initial preparation in the two-atom state

$$|\Psi_0\rangle = \cos^2\left(\frac{\theta}{2}\right)|00\rangle - \sin^2\left(\frac{\theta}{2}\right)|11\rangle - i \sin\left(\frac{\theta}{2}\right) \cos\left(\frac{\theta}{2}\right) (|01\rangle + |10\rangle) \quad (3.4.1)$$

using a global rotation, and a subsequent quantum non-demolition (QND) measurement through the cavity. For small values of θ , based on the observations shown in Fig. 1C, conditional detection of a single reflected photon projects out $|00\rangle$ from the two-atom Hilbert space, thus leaving the system primarily in $|\Psi^+\rangle = (|01\rangle + |10\rangle)/\sqrt{2}$ (Fig. 3A). We initialize the atoms in $|00\rangle$, rotate the state by $\theta = 0.3 \pi$, send a weak coherent pulse ($\bar{n} = 0.35$) and condition on a detected photon. The finite angle θ is chosen to maximize the overlap with $|\Psi^+\rangle$. It is set to minimize the residual population in $|11\rangle$ while also accounting for a finite projection fidelity out of $|00\rangle$. After the projection, we apply an additional $\pi/2$ pulse and rotate the Bell state $|\Psi^+\rangle$ into $|\Phi^+\rangle$ for ease of characterization.

We first characterize the entangled state *in-situ* using the cavity reflection readout shown in Fig. 1C. We characterize the $|\Phi^+\rangle$ fidelity $\mathcal{F} = \langle \Phi^+ | \rho | \Phi^+ \rangle = \frac{1}{2}(\rho_{00,00} + \rho_{11,11} + 2\rho_{00,11})$ by directly measuring the populations, and by extracting coherence from the parity oscillation contrast upon another $\pi/2$ rotation over different axes [96, 126, 118].

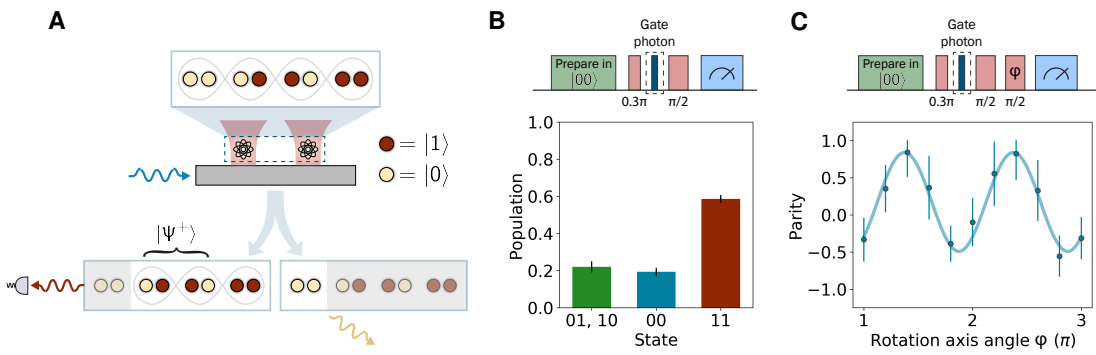


Figure 3.3: **Heralded entanglement at the cavity.** (A) Protocol description. Post-selection on the photon reflection from a superposition state carves out the state component in $|00\rangle$, leaving the atoms predominantly in $|\Psi^+\rangle$. (B) After applying the protocol to two atoms at the cavity, we measure populations in different basis states. Before the measurement, we apply a $\pi/2$ pulse which converts the Bell state $|\Psi^+\rangle$ into $|\Phi^+\rangle$. The readout does not distinguish between $|01\rangle$ and $|10\rangle$. (C) Parity oscillations of the $|\Phi^+\rangle$ state after a rotation over a varying axis ϕ , showing non-classical correlations between the qubits in all the bases. Coherence $\rho_{11,00}$ is extracted from the amplitude. Combining the measured coherence and populations, we arrive at the Bell state fidelity of $\mathcal{F} = 0.72(3)$.

Fig. 3B shows the populations of $\mathcal{P} = 0.78(3)$, where the remaining component of $|\Phi^-\rangle$ causes the asymmetry between $|00\rangle$ and $|11\rangle$ (see Appendix A). The parity oscillation in Fig. 3C corresponds to a coherence of $\rho_{11,00} = 0.33(2)$. From these measurements, we extract a fidelity of $\mathcal{F} = 0.72(3)$, corresponding to a concurrence bound of $\mathcal{C} \geq 0.46(5)$. The majority of the infidelity is accounted for by the finite initial angle θ (24%), with an additional 4% from the initialization imperfections, and less than 1% from incoherent scattering (see Appendix A).

3.5 Entanglement transport

Finally, we transport the entangled atoms away from the cavity while applying the decoupling pulses and analyze the final state in free space via state-selective pushing of the atoms out of the trap followed by atom detection (Fig. 4A) (see Appendix A). We measure the qubit state populations in the ZZ , XX , and YY bases (Fig. 4B), and extract the population in the $|\Phi^+\rangle$ state of $\mathcal{P} = 0.78(6)$, and the coherence $\rho_{11,00} = 0.26(5)$, giving a fidelity of $\mathcal{F} = 0.65(6)$, and a lower bound to concurrence of $\mathcal{C} \geq 0.35(11)$. Since $\mathcal{F} > 0.5$ and $\mathcal{C} > 0$ constitute proofs of entanglement, our measurements demonstrate entanglement after transport at a 98.8% confidence level. The state fidelity is consistent with the decoherence we observe for single atoms during transport shown in Fig. 2C assuming uncorrelated noise baths. This assumption is supported by the hypothesis that the decoherence during transport is dominated by the fluctuations in

the programmed atomic trajectories and atomic thermal motion.

3.6 Conclusion and outlooks

The methods demonstrated here can be improved and extended in several ways. The ability to distinguish the collective uncoupled state $|0\rangle^{\otimes N}$ from the other states with a single photon, essential for cavity carving entanglement method, can be improved by using critically coupled cavity, and by enhancing interferometric stability. This would allow for a smaller initial angle θ , and a consequently higher entanglement fidelity. We project that a moderate improvement in the cavity contrast (from 0.4 to 0.1) would improve two-atom entanglement fidelity to 0.9. Measurement-based protocols rely on the trade off between the success probability and the fidelity [96]. Our parameters (θ, \bar{n}) are selected to optimize entanglement fidelity, resulting in the success probability of heralding the entanglement of 0.6% (see Appendix A). This can be improved with a higher collection efficiency (currently $\eta = 0.28$), by using superconducting nanowire detectors and optimizing PCC-fiber coupling efficiency. To improve the integration with a free space array, higher efficiencies for loading atoms into and out of the cavity near-field are required. Previous work on our platform has shown that atoms cooled to the motional ground state in the radial direction can be loaded into the cavity near-field with the 94(6)% efficiency [117]. Reducing loss at higher initial temperatures could be possible with deeper traps and modified loading methods (see Appendix A).

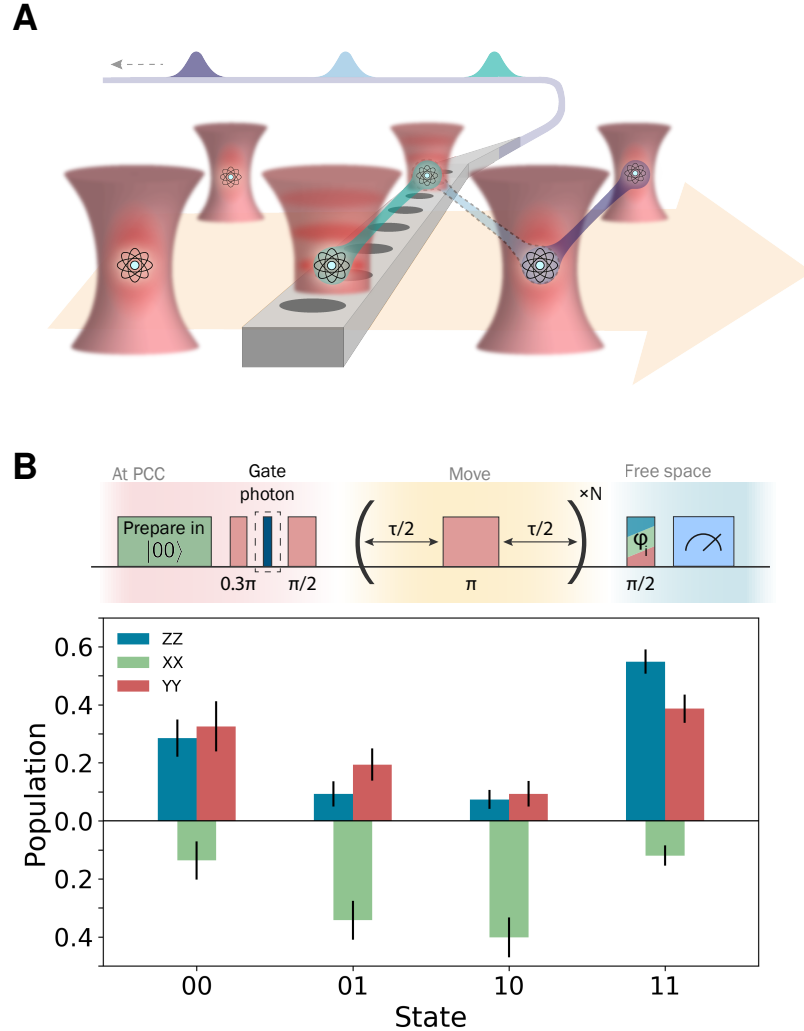


Figure 3.4: Coherent transport of entangled atoms. (A) After entangling the atoms at the cavity, we move the tweezers away while applying dynamical decoupling. Entangled state distribution can be used to connect our system to a free space array, and to generate various many-body entangled states such as cluster states. (B) Free-space readout in different bases after transport shows the persistence of non-classical correlations, giving the entanglement fidelity of $\mathcal{F} = 0.65(6)$.

Furthermore, decoherence during transport could be decreased by a more homogeneous generation of tweezers, for instance with an acousto-optic deflector (AOD). Using an AOD would increase the moving speed by a factor of 100, enabling us to move the atoms for more than $100 \mu\text{m}$ distances, which should be sufficient for a high-fidelity Rydberg state control [127]. Coherence could also be improved by minimizing the sensitivity to the differential light shifts through cooling to the motional ground state.

Our experiments are a promising step in using atom-nanophotonic platforms for quantum networking, and demonstrate essential ingredients for integrating an efficient quantum optical interface with large-scale neutral atom quantum processors based on Rydberg atom arrays. Such an integration could open up several remarkable directions. In particular, it could be used for fast, high-fidelity QND readout of the atomic qubits, essential for feed-forward protocols such as quantum error correction. Combining the atom-photon entanglement capability [77], coherent transport and Rydberg interactions, would enable quantum teleportation of array's states to optical photons as well as entanglement of remote atom arrays. Similar to the corresponding demonstration with trapped ions [128], our approach has added benefits of a completely local atom-photon interaction that would not perturb the qubits stored in the rest of array. Integrating a cavity platform with a Rydberg array could also add completely new functionalities such as the multi-qubit controlled-phase gates (generalization of a Duan-Kimble gate [85]), that could be useful for generating large entangled states and for exploring novel error-correction architectures. Finally, by entangling groups of atoms and arranging them

into arbitrary spatial configurations, one may be able to expand the design space enabled by the more flexible connectivity and create exotic many-body quantum states such as cluster or graph states useful for exploring new applications and fundamental studies [129].

4

Conclusion

This thesis presents an approach to realizing efficient interfaces between atoms and photons. Trapping neutral atoms in optical tweezers within the evanescent field of a photonic crystal cavity, we demonstrate strong atom-photon interactions characterized by the figure of merit cooperativity $C \sim 70$, as well as cavity-mediated atom-atom interactions characterized by level repulsion (Chapter 2). The atomic qubits can be coherently controlled near the nanostructure and maintain the coherence when transported away. Based on the efficient optical interface, we generate Bell pairs and show that they remain entangled away from the cavity (Chapter 3).

As preluded in Chapter 1, these results present a major step towards quantum networks, namely the construction of two-qubit nodes with local operations, adding to the fundamental building blocks for quantum networks along with previous results on atom-photon gates [77, 130]. While scaling up to a large number of qubits per node is not

strictly necessary for quantum networking, higher fidelities on local gates are crucial for a variety of elementary protocols, from entanglement distillation [131, 132] to quantum repeaters [20, 133].

The fidelity of our current implementation of entanglement generation is limited by detection error, which can be addressed with improved interferometric stability as discussed more in detail in Appendix B. Heralded protocols such as the entanglement carving protocol discussed in Chapter 3 trade off success probabilities for fidelities. Within reach of the current technology, we can achieve a more favorable cavity outcoupling ratio, optical throughput from the fiber-waveguide interface to the detector, and detection efficiency that yield an overall increase in the detection efficiency by two orders of magnitude. The fidelities of quantum networking protocols are ultimately limited by the cooperativity, with the errors scale as $\sim 1/C$ for heralded schemes and $\sim 1/\sqrt{C}$ for deterministic schemes. The cooperativity can be improved by positioning the atoms closer to the cavity to for them to experience a stronger evanescent field [76, 97], improving the design and fabrication of the nanophotonic devices [98], or cooling the atoms for tighter localization with respect to the mode maxima [99]. Using single-photon sources will eliminate the need for weak coherent pulses, eliminating the probabilistic nature of photon arrival and reducing errors due to scattering. Achieving near-deterministic operations will lead to a wide variety of applications beyond quantum networks such as the generation of highly entangled states of photons and measurement-based quantum computation [134, 135, 136, 137].

The small footprint of nanophotonic devices offer good prospects for larger and more complex architectures for quantum networks. Several cavity devices can be installed in the same optical setup, presenting possibilities of multiplexing several nodes with minimal modifications to the current vacuum apparatus. Moreover, the current technology for fabricating integrated photonics has become mature enough to produce on-chip photonic circuits with desired capabilities [138, 139, 140], and several efforts have recently explored interfaces between on-chip devices with trapped ions [141] and tweezer arrays [73, 142, 143], miniaturizing and reducing the complexity of cold-atom experiments.

For our system to be operational in quantum networks over geographical distances, there remain several major technical challenges to address. First, although atomic coherences are generally excellent compared with other quantum systems [64, 65], the atomic coherence time close to the nanostructure is measured to be 2 ms in our system with a spin-echo sequence in the absence of illumination. The coherence time is limited by thermal motion through the varying differential light shift (see Appendix B and [144, 145]) and can be extended by choosing a more favorable trap wavelength. We also expect improved cooling [59, 60] to result in longer coherence times, as well as less thermal averaging of cooperativity (Appendix A). Second, the near-infrared atomic transition suffers from fiber attenuation ($\sim 3.5 - 4.0$ dB/km at 780 nm) that become considerable over kilometers. Accessing telecom wavelengths will extend the range by an order of magnitude due to more favorable attenuation (~ 0.5 dB/km at 1550 nm) and open up possibilities of using integrated on-chip silicon-based devices [46, 47].

The ability to coherently transport quantum states (Chapter 3) presents prospects for integrating our system to large-scale quantum systems of Rydberg arrays, a rapidly-developing platform with high-fidelity operations on hundreds of qubits [63, 146]. Optical interfaces will add capabilities to address some of the major challenges of the platform, namely the lack of rapid non-destructive readout and the inherently short range of the Rydberg interactions. To realize such interfaces, there remains a number of technical questions remain to be investigated.

First, while the transport results in Chapter 3 rely on the transport survival to be near-deterministic upon departure from the nanostructure, future applications will require deterministic survival upon arrival. The survival probability upon arrival strongly depends on the temperature (see Appendix B). For a temperature of $15 \mu\text{K}$ reached after polarization gradient cooling, we observe a survival probability of 0.55 during transport with no cooling upon arrival. Performing extra polarization gradient cooling upon arrival will remedy losses, yielding a survival probability of 0.8, but scattering from the cooling and repumping light will erase the information stored in the internal state of the atoms. Ultimately, cooling the atoms close to the ground state [59, 60] will result in deterministic survival [76]. The deterministic survival upon departure at the current implementation is nevertheless readily suitable for protocols that rely on one-way transport. For example, in entanglement purification, one can generate entangled pairs at two distant cavities and transport them out to perform local Rydberg operations with a target pair away from the cavity with.

Second, Rydberg atoms are required to maintain distance from any object that may introduce stray electric field [147]. Compared to macroscopic cavities, we predict a nanoscale cavity to be advantageous due to its small footprint and the absence of a large electric field usually present in piezoelectric tuning. Nevertheless, the minimum required distance from the small footprint of the nanophotonic device assembly remains unknown. For coherent transport to work in conjunction with Rydberg arrays, this distance must be within the product between the speed of beam steering and the coherence time.

Beyond quantum networks, there are other scientific directions to be explored with our platform. In Chapter 2, we have observed a strong dependence of the atom-cavity response to position fluctuations. Combined with the strong quantum nonlinearity [77] and the internal degrees of freedom of neutral atoms, the strong response may open up possibilities for studying optomechanics from new perspectives [74]. Finally, the platform is also suitable for designing interactions for quantum simulators to study many-body physics, enabled by photonic band engineering [75].

Looking forward, the aforementioned applications enabled by efficient atom-photon interfaces pave the way towards additional capabilities for quantum systems. Not only do quantum networks allow for secure communication between parties, they also present prospects for scaling up otherwise near-term systems, in particular those of neutral atoms based on tweezer arrays, a versatile platform with applications in quantum simulation, quantum information processing, and metrology. Optical interfaces enable systems to operate in concert and benefit from collective performances. Introducing

rapid non-destructive detection to the atomic platform will enable new abilities such as quantum error correction, a cornerstone operation for fault-tolerant quantum computing. Incorporating excellent quantum control of atoms to nanophotonic devices will also enable applications in multiple directions. The vast design possibilities and developed fabrication techniques will enable engineering quantum devices based on photonic integrated circuits interfaced with atoms as well as explorations of novel atom-photon interactions for studying fundamental physics.

A

Apparatus and methods used in chapter 2

A.1 Apparatus

The apparatus consists of a confocal microscope that images a photonic crystal (PC) installed in the glass cell of the vacuum chamber (Fig. A.1). The microscope objective (Mitutoyo G Plan Apo 50X) is used for focusing optical tweezers (beam waist $w_0 \sim 900$ nm) and for fluorescence imaging of single atoms. The two tweezers are generated by combining two optical paths on a 50:50 non-polarizing beam splitter at the focus of a 4f-microscope configuration. Each path also has two dichroic mirrors, to combine the trap light (815 nm) with individual repumping light (795 nm) and to separate the collected fluorescence light (780 nm).

The ultra-high vacuum (UHV) system consists of a glass cell mounted to a compact vacuum cube (Kimball Physics MCF450-SphSq-E2C4) and a combination of a non-

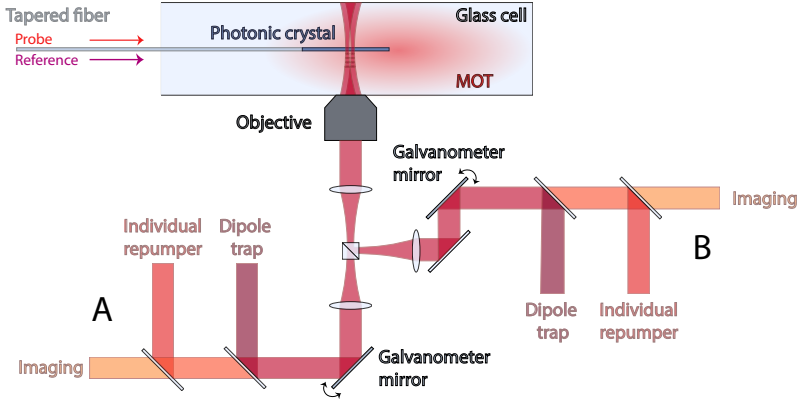


Figure A.1: Schematic of experimental setup (not to scale) detailing how the trap paths are combined and focused by the objective onto the PC. Resonant light is sent through the tapered fiber to the PC to probe the atom-cavity response, along with far-detuned light for cavity stabilization, which is continuously monitored in reflection.

evaporable getter and an ion pump (NEXTorr D300-5). The entire system is mounted on a translation stage that can be retracted for device exchange without disturbing the optical paths around the chamber. The small and moveable vacuum system allows for speed-up of typically extensive procedures such as device replacement and pumping to UHV, which in our system can take less than one week in total. The PC is suspended at the tip of a tapered fiber [92], which is mounted on a rod assembly and led to the outside of the vacuum through a fiber feedthrough [148]. The probe light is sent to the cavity through a beam-sampler and coupled into the fiber, where the reflection is collected through the transmission port and onto a single-photon counter (PerkinElmer SPCM-AQR-16-FC). The reference light for cavity stabilization is combined with the

probe on a dichroic before coupling into the fiber and is monitored in reflection with a high-bandwidth avalanche photodiode (Menlo Systems APD210).

A.2 Photonic crystal cavities

A.2.1 Design and fabrication

The design of the cavity follows that in [149, 150]. The cavity used in this work is designed to operate near the critical coupling regime ($\kappa_{wg} \approx \kappa_{sc}$) for a minimal total loss rate $\kappa = \kappa_{wg} + \kappa_{sc}$. Since κ_{sc} is limited by fabrication imperfections, we decrease κ_{wg} by controlling the loss from the first Bragg mirror with the number of holes that define it, as shown in Fig. A.2. To reach the critical coupling regime, κ_{wg} is tuned to be comparable to the loss from the cavity into free space κ_{sc} which has typical values of several gigahertz. The device used in this work has $\kappa_{wg} = 2\pi \times 0.86$ GHz and $\kappa_{sc} = 2\pi \times 2.77$ GHz.

The fabrication process begins with a 200 nm layer of silicon nitride (bulk index of refraction = 2.02) on a silicon wafer (Silicon Valley Microelectronics, Inc.). A pattern of 500 devices is created by exposing a layer of resist (ZEP520A) on the wafer to a scanning electron beam (Elionix F125). The pattern is then transferred to the silicon nitride layer using reactive ion etching. The silicon underneath is removed in a wet etch process with KOH. At the end of the process, we deposit an absorptive material

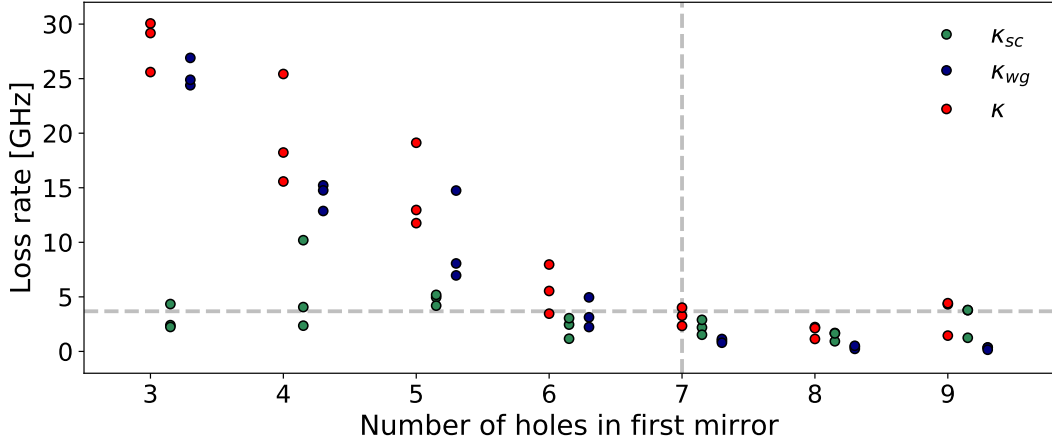


Figure A.2: Modifying the first mirror loss with the number of holes in the first mirror of the PC and comparing the loss rates for several devices with each hole number. Grey lines are drawn to indicate the number of holes chosen for the current cavity and its total loss of $\kappa = 2\pi \times 3.68$ GHz.

(amorphous silicon) onto the disk-shaped heater pad region for thermal tuning of the resonance.

A.2.2 Frequency stabilization of the cavity

The resonance of the fundamental mode of the nanophotonic cavity sits near the $5S_{1/2} \rightarrow 5P_{3/2}$ transition at 780 nm, but there exist higher-order modes at longer wavelengths as shown in Fig. A.3a. For the device used in this work, the second-order mode has a resonance near 810 nm, which is off-resonant for the atoms, and has a linewidth of $2\pi \times 17$ GHz. A laser pointed at the heater pad region heats up the device and changes the index of refraction, tuning the resonances by the same increment, as shown

in Fig. A.3b. The bandwidth of the feedback loop is limited by this thermal tuning process at several milliseconds.

We stabilize the cavity monitoring the second-order mode and feeding back to the tuning laser power. The error signal is generated by modulating the phase of the reference light at 810 nm continuously sent to the cavity at 1 GHz. The reflected signal from the monitoring avalanche photodiode is demodulated at the same frequency, creating a low-modulation Pound-Drever-Hall error signal (Fig. A.3c) [151]. In the experimental sequence described in the next section, the cavity resonance must be tuned in and out of resonance during each trial for different probe pulses. We achieve this by jumping the setpoint and waiting for several milliseconds for the cavity to settle before probing. We have observed no degradation in the quality factor after inserting our current device within the vacuum system and continuously tuning and stabilizing its resonance for over one year.

A.3 Experimental sequence

We load atoms into the optical tweezers from a magneto-optical trap around the PC. Operating in the collisional blockade regime [152], we monitor the fluorescence from each of the tweezers with our detector (Excelitas SPCM-AQRH-14-FC) and distinguish between having zero and one atom in each tweezer with fidelity of $> 99\%$. Every repetition of the experiment begins by triggering on the successful loading of both

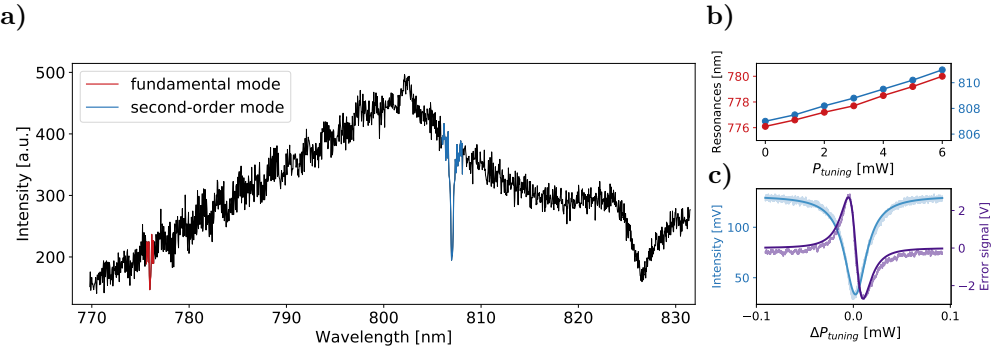


Figure A.3: **a)** Different resonances of the PC cavity observed by sending broadband light and collecting in reflection on a spectrometer. **b)** Simultaneous tuning of the first (red) and second (blue) order resonant wavelengths by increasing the tuning laser power incident on the heater pad. **c)** A reflection spectrum of the second order resonance (blue) and the PDH signal from the spectrum (purple) obtained from sweeping the tuning laser power over the resonance.

atoms (Fig. A.4), followed by a 20 ms period of polarization gradient cooling to bring the atom's temperature down from $50 \mu\text{K}$ after loading to $15 \mu\text{K}$.

The atoms are transported to the final positions on the PC by steering the individual galvanometer mirrors. Given that our cavity mode is 500 nm wide and 4 μm long, accurate positioning of the traps relative to the mode is crucial for the experiment. The position of the PC on the fiber tip can drift at a rate of $\sim 100 \text{ nm/hour}$ relative to the microscope objective. To correct for this drift, we pause the experiment every 20 minutes and acquire confocal images of the PC at different focal planes. The images are processed to determine the new position of the PC in three dimensions. In addition, every few days, we calibrate the atomic coupling strengths versus position and reposition the atoms such that they have equal coupling strength.

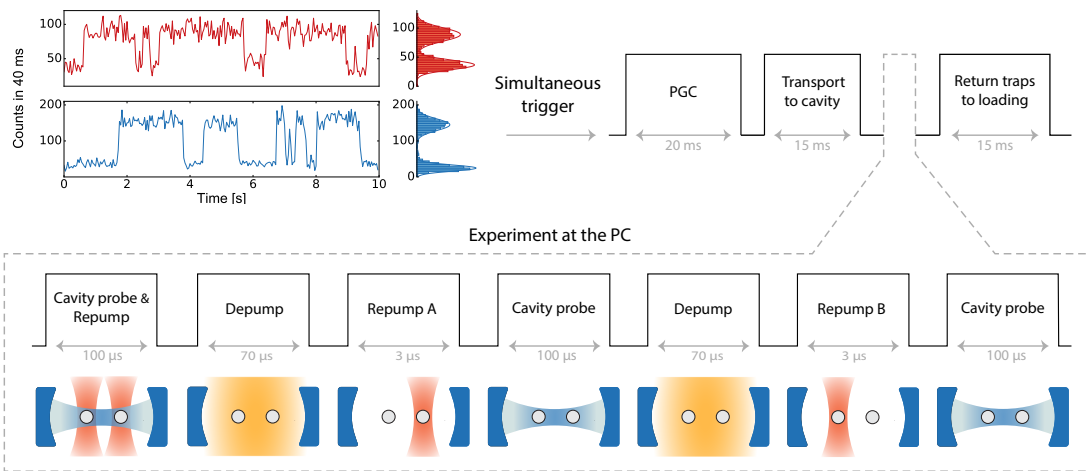


Figure A.4: Experimental run is triggered upon rising edges of fluorescence counts from the atoms, followed by polarization gradient cooling (PGC). The sequence when the atoms are loaded next to the PC is depicted below, indicating which beams are global and which are local. The individual repumping beams are tuned to the $5S_{1/2}, F = 1 \rightarrow 5P_{1/2}, F' = 2$ transition, the global depumping beam to the $5S_{1/2}, F = 2 \rightarrow 5P_{3/2}, F' = 1$ transition. The data for spectra is taken from the first probe phase, while the second and third probe phases are used for individual atom post-selection.

To take the reflection spectra, we probe the cavity with light resonant with $2 \rightarrow 3'$ transition while constantly depleting the $F = 1$ manifold with the individual repumpers. After acquiring the spectrum, we post-select the data for which an atom was loaded next to the cavity, which occurs with $\sim 70\%$ probability and is mainly limited by the initial temperature in the traps. We first prepare both atoms in the uncoupled ground state level $F = 1$ with a global beam resonant with the $5S_{1/2}$, $F = 2 \rightarrow 5P_{3/2}$, $F' = 1$ transition. Then we individually pump a single atom into the coupled ground state $F = 2$ with a beam resonant with the $5S_{1/2}$, $F = 1 \rightarrow 5P_{1/2}$, $F' = 2$ transition, co-propagating with the optical tweezers. After this selective pumping, we probe the cavity on resonance to determine the atom's presence in a single shot (Fig. 1d, main text). Repeating this procedure for the other atom allows us to select for data where one, the other, or both atoms are present. Once the experiment at the PC is finished, the tweezers are transported back to the original loading positions. The sequence is outlined in Fig. A.4.

The probe experiment taking place at the cavity typically takes $500 \mu\text{s}$, much shorter than the lifetime of atoms in the trap next to the PC of $\sim 100 \text{ ms}$. Compared with the lifetime of 1.5 s away from the PC, the reduced lifetime next to the PC indicates additional heating mechanism, as previously observed by [153]. Understanding the sources of extra heating and developing cooling techniques while next to the PC is a subject for future exploration.

A.4 Individual tuning of the atomic resonances

The independent optical tweezer paths in our setup allow for individual manipulation of the internal atomic states. In this work, we change the relative atomic detuning δ_{12} through light shifts from the individual tweezers. This is done by modulating their intensities out of phase. Tuning the contrast of the modulation then shifts the atoms in and out of resonance with respect to each other. Note that we choose the modulation frequency $\Delta_{\text{mod}} \approx 2\pi \times 5 \text{ MHz}$, which is faster than the motional frequencies of the traps, thereby subjecting the two atoms to the same average trapping potential. The intensity modulation is generated using a Mach-Zehnder interferometer, with an acousto-optic modulator (AOM) driven at $\omega_{\text{AOM}} \pm \Delta_{\text{mod}}/2$ in each arm, where $\omega_{\text{AOM}} = 2\pi \times 80 \text{ MHz}$ is the central frequency of the AOMs. The relative phase between the two tweezers can be tuned by sending one of the outputs of the interferometer through a delay line ($\sim 100 \text{ m}$) and fine tuning the relative drive frequency Δ_{mod} to match the path difference. The modulated optical signal is also used to trigger the probe light sent to the cavity. Calibrating the delay of the triggered probe pulse allows us to probe the atoms at their maximum/minimum light shifts. When operating with the traps out of phase, changing the contrast of this modulation changes the individual lightshift of each atom and is used to sweep the atom-atom detuning as depicted in Fig. A.5.

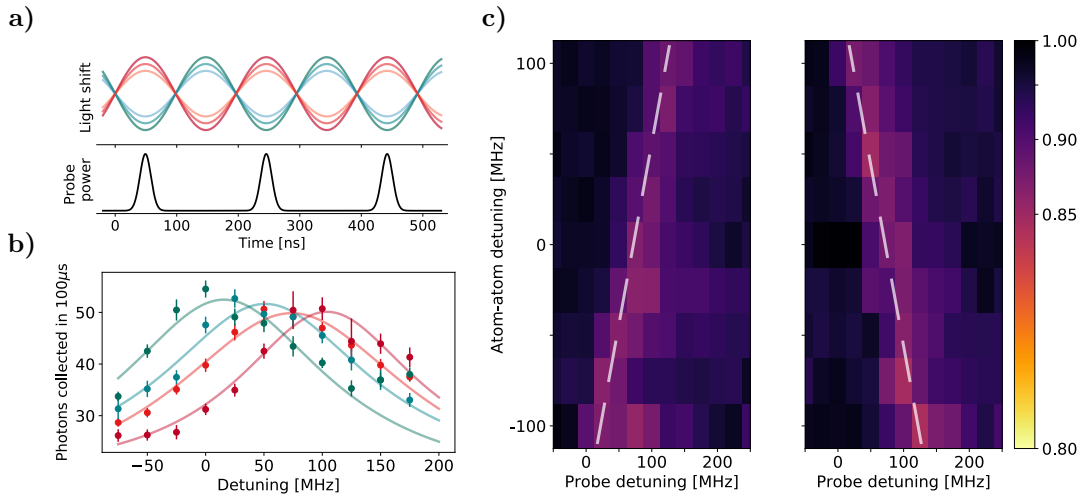


Figure A.5: **a)** Illustration of the instantaneous light shift experienced by each atom probed while modulating the individual tweezer intensity. **b)** Reflection spectra in the resonant regime at two different modulation contrasts (light/dark) for one atom (greens) and the other (reds) to show how the individual light shifting can be tuned simultaneously. **c)** Experimental data of reflectivity map over probe detuning and atom detuning in the dispersive regime showing light shift tuning. Fig.4a in the main text is generated from the average of these two plots.

A.5 Theoretical models

To model the reflection spectra, we study the transitions between the $5S_{1/2}$, $F = 2$ ground state manifold, labeled $|g\rangle$, and the relevant excited states in $5P_{3/2}$ i.e. $F' = 1, 2, 3$, labeled $|e_i\rangle$, where $i = 1, 2, 3$. For the on-resonance measurements (FIGs. 1 and 2 in the main text), the cavity frequency ω_c is resonant with the $2 \rightarrow 3'$ transition. The cavity field decay rate ($\kappa = 2\pi \times 3.7$ GHz) is smaller than the hyperfine splitting between the $F = 1$ and $F = 2$ ($\Delta_{HF} = 2\pi \times 6.8$ GHz), so we neglect the cavity coupling to $F = 1$ manifold. Experimentally, we confirm this by noting that when the atom is in $F = 1$, the cavity reflectivity is the same as if there were no atom coupled to it.

A system consisting of a cavity and a multi-level atom is described by the Hamiltonian [154]:

$$H = \omega_c a^\dagger a + \sum_i \omega_i \sigma_i^\dagger \sigma_i + \sum_i g_i (a^\dagger \sigma_i + a \sigma_i^\dagger) \quad (\text{A.5.1})$$

where $\sigma_i = |g\rangle \langle e_i|$ and a are the lowering operators for the atomic and cavity excitations respectively, g_i is the single-photon Rabi frequency between the cavity and the excited state $|e_i\rangle$, and ω_i is the resonance frequency between $|g\rangle$ and $|e_i\rangle$. Each excited state decays into free space at a rate γ , and cavity decays at a total rate κ , out of which κ_{wg} is into the collected waveguide mode.

To model the incoherent population decays from the atomic excited states and the cavity mode, we define the Lindblad jump operators $L_0 = \sqrt{\kappa}a$ and $L_i = \sqrt{\gamma}\sigma_i$. We use individual decay operators L_i instead of the cumulative decay operator $\sum_i L_i$ because

$\gamma = 2\pi \times 6$ MHz is much smaller than the hyperfine splittings in the excited states of $2\pi \times \{267, 157\}$ MHz, so we can neglect the interference between the spontaneously emitted photons. We confirm this by numerically modelling and comparing both cases.

The system dynamics can be described with Heisenberg-Langevin equations of the form

$$\dot{A} = i[H, A] + \sum_i \left(L_i^\dagger A L_i - \frac{1}{2} (A L_i^\dagger L_i + L_i^\dagger L_i A) \right) \quad (\text{A.5.2})$$

where $A \in \{a, \sigma_i\}$. After solving for a , the reflectivity can be obtained from the input-output relation:

$$a_{out} + a_{in} = \sqrt{\kappa_{wg}} a \quad (\text{A.5.3})$$

$$r = \frac{a_{out}}{a_{in}} = \sqrt{\kappa_{wg}} \frac{a}{a_{in}} - 1 \quad (\text{A.5.4})$$

The resulting system of equations reads:

$$\dot{a} = -i\omega_c a - i \sum_j g_j \sigma_j - \frac{\kappa}{2} a + \sqrt{\kappa_{wg}} a_{in} \quad (\text{A.5.5})$$

$$\dot{\sigma}_i = -i\omega_i \sigma_i + ia \sum_j g_j \left(|e_j\rangle \langle e_i| - \delta_{i,j} |g\rangle \langle g| \right) - \frac{\gamma}{2} \sigma_i \quad (\text{A.5.6})$$

We are interested in the frequency response of the reflection to a weak drive of frequency ω . Since the steady-state population in $|e_i\rangle$ is negligible in this weak excitation limit,

we can substitute $|e_j\rangle\langle e_i| - \delta_{i,j}|g\rangle\langle g| \approx -1$. Solving these equations, we obtain the reflectivity

$$r = \kappa_{wg} \left(\frac{\kappa}{2} - i\delta_c + \sum_i \frac{g_i^2}{\gamma/2 - i\delta_i} \right)^{-1} - 1, \quad (\text{A.5.7})$$

where $\delta_c = \omega - \omega_c$ and $\delta_i = \omega - \omega_i$. The expression has the same format as the one for multiple emitters coupled to the same cavity mode [155] and can be extended by modifying the sum to include multiple emitters. The cooperativity associated with the i -th transition is $C_i = 4g_i^2/\kappa\gamma$. The reflection spectra are measured as $|r(\omega)|^2$.

A.5.1 Atomic motion in the cavity mode

Nanophotonic structures confine photons to sub-wavelength mode volumes. The longitudinal confinement is a $\sim 4 \mu\text{m}$ long gaussian envelope, and the transverse confinement is given by the evanescent field of decay with the characteristic length of $z_0 = 120 \text{ nm}$ [76]. Moreover, the mode intensity is longitudinally modulated with the lattice constant of $a = 290 \text{ nm}$. Due to these spatial variations, an atom in motion will be subjected to a fluctuating coupling strength.

The variation of the atomic position depends on its temperature and confinement length scale. Given the motional radial frequency measured to be $2\pi \times 115 \text{ kHz}$, we obtain the size of the atomic spatial width of 50 nm in the radial direction of the tweezer at 15 μK (the temperature reached after polarization gradient cooling). As the atoms are transported to the cavity, the trapping potential gains additional axial

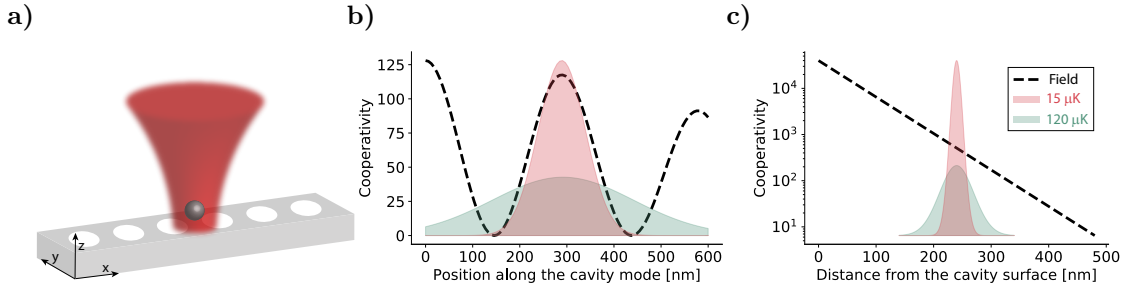


Figure A.6: a) Illustration of an atom trapped in a tweezer above the photonic crystal and definition of axes. b) Cooperativity variation in the longitudinal (x-axis) direction. The green and red dashed lines correspond to the atomic spatial width at $120 \mu\text{K}$ and $15 \mu\text{K}$, respectively. c) Cooperativity variation and atomic spatial widths in the z direction.

confinement from the reflection of the tweezer off of the structure [76]. The process of potential distortion from a gaussian beam to a standing wave can introduce heating to the atom. From separate measurements of the coherence times between two magnetic sublevels in the ground state at varying tweezer depths similar to [120], we estimate the upper bound for our temperature at the cavity to be $120 \mu\text{K}$, corresponding to a spatial width of 150 nm in the radial direction of the tweezer.

The standing wave formed in the axial direction results in a higher axial frequency of $2\pi \times 550 \text{ kHz}$. This tight confinement is crucial for the operation since the evanescent field decays sharply in the axial direction. Fig. A.6 shows the variation of the cavity mode in the x- and z- directions, overlapped with our estimates of the {lower, upper} bound on spatial width at $\{15, 120\} \mu\text{K}$, corresponding to the axial widths of $\{12, 30\} \text{ nm}$.

To account for the cavity field sampling, we model the cooperativity C , which is

proportional to the field intensity I , to vary in the two directions as

$$C(x, z) = C_0 \cos^2\left(\frac{\pi x}{a}\right) e^{-2z/z_0} \quad (\text{A.5.8})$$

where $a = 290$ nm, $z_0 = 120$ nm, and C_0 is the cooperativity the atom would experience in the absence of motion at its center position $(x, z) = (0, 0)$. Note that we have neglected the slowly-varying envelope in the direction along the standing wave with the characteristic mode length of 4 μm as well as the variation in the y direction.

A.5.2 Cooperativity estimation

To model our experimental reflection spectrum (e.g. Fig. 1d, main text) and extract an estimate for the associated cooperativity, we combine the expression for reflectivity in Eq.(A.5.7) with the spatial dependence of the cooperativity in Eq.(A.5.8). To produce a spectrum, we sample atomic positions in the x and z directions (as defined in Fig. A.6a) from normal distributions with standard deviations w_x and w_z respectively and generate a reflectivity averaged over multiple values of the resulting cooperativities. The fit parameters consist of w_x , w_z , and the cooperativity amplitude $C_{0,i}$ in Eq.(A.5.8) associated with transition to each excited state $|e_i\rangle$.

The best fit (Fig. A.7a) for the data according to this model yields $w_x = 190$ nm, $w_z = 33$ nm. The cooperativity associated with the 3' line of interest is $C_{0,i=3} = 128(6)$ in the absence of motion. The histogram of the cooperativity distribution associated

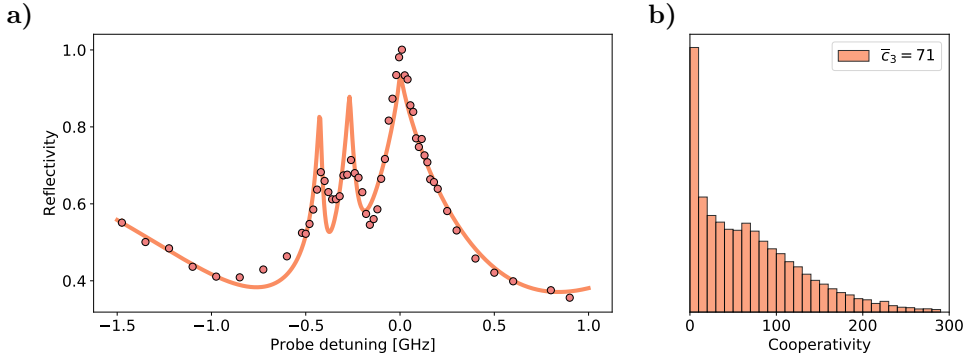


Figure A.7: **a)** Theoretical model for the single-atom reflection spectrum at the mode maximum overlapped with experimental data. **b)** Associated cooperativity distribution with the mean of 71(4) and standard deviation of 66(4).

with the spectrum is shown in Fig. A.7b, yielding the mean of $\langle C_{i=3} \rangle = 71(4)$, and the standard deviation of 66(4). The uncertainties are determined by bootstrapping.

The value of C_0 extracted is consistent with our independent estimate of the field strength at the surface of the PC of $2g_{\max} \approx 2\pi \times 15$ GHz which evanescently decays down to $2g_0 \approx 2\pi \times 1.7$ GHz at 260 nm away from the PC. The single-photon Rabi frequency at the surface $2g_{\max}$ (corresponding to the maximum cooperativity of $C_{\max} \approx 40,000$) is calculated from the single-photon electric field of $E_{\max} \approx 2$ kV/cm, estimated for the mode volume $V_{\text{mode}} = 0.4\lambda^3$ [76]. The biggest deviation from the model occurs in the height of the 1' and 2' lines. Some of the effects neglected in this model include decays to $F = 1$ ground state and repumping from it (which could explain the reduced heights), the motion in the y direction, heating during probing, and trap pointing uncertainty.

The two-atom spectrum (FIG 2, main text) is taken with atoms placed 1 μm away

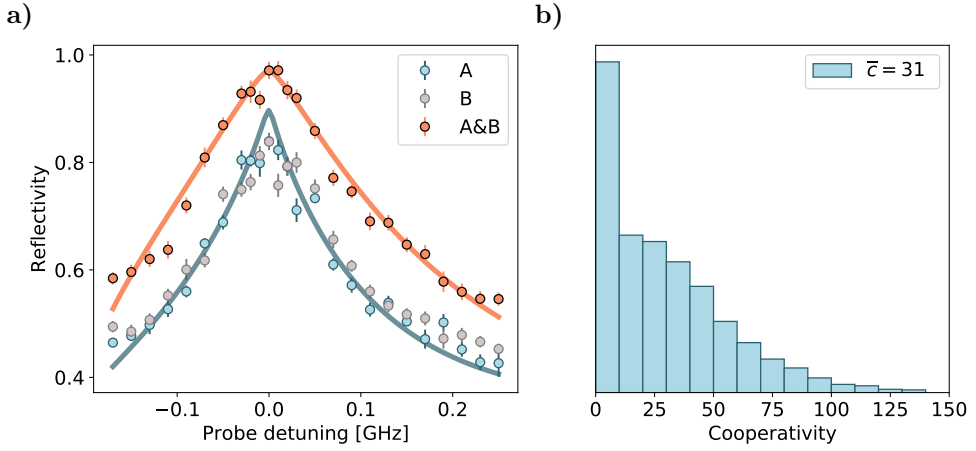


Figure A.8: **a)** Theoretical model for the single-atom reflection spectrum $1 \mu\text{m}$ away from the mode center (blue) and for the two-atom reflection spectrum (red) generated using the same cooperativity distribution. **b)** Distribution of single-atom cooperativity for the $2 \rightarrow 3'$ transition.

from the mode center. We now focus on the $3'$ line, which is also the transition we use in the dispersive regime. The fit to the single-atom reflectivity at this position is shown in Fig. A.8. The spatial widths $w_x = 190 \text{ nm}$, $w_z = 33 \text{ nm}$, are the same as those in Fig. A.7, whereas $C_{0,i=3} = 56(3)$, corresponding to the mean single-atom cooperativity of $\langle C_{i=3} \rangle = 31(2)$ and the standard deviation of $28(2)$, averaged over two atoms. The reduction of the mean cooperativity is expected from the mode profile shown in Fig. 2c in the main text. The two-atom reflection spectrum is generated based on both single-atom spectra with no additional parameters.

The spectra in the dispersive regime taken with nonzero light shifts (Fig. 3b, 4, main text) are analyzed with the same model. In addition, we take into account the effect of fluctuating light shift $\delta_{A,B}$ due to atomic motion. We extract $J = 2\pi \times 25(4) \text{ MHz}$ at

$\Delta = 2\kappa$, consistent with our cooperativity estimate for the resonant regime.

B

Apparatus and methods used in chapter 3

B.1 Cooperativity estimate

The reflectivity amplitude of an atom-cavity system driven at a frequency ω can be calculated as [114]:

$$r = \kappa_{wg} \left(\frac{\kappa}{2} - i\Delta_c + \frac{g^2}{\frac{\gamma}{2} - i\Delta_a} \right)^{-1} - 1 \quad (\text{B.1.1})$$

where γ is the atomic spontaneous decay rate, g is the single-photon Rabi frequency, $\Delta_a = \omega - \omega_a$ is the atomic detuning, and $\Delta_c = \omega - \omega_c$ is the cavity detuning. The cavity decay rate κ is the sum of decay into the waveguide κ_{wg} , and the decay elsewhere at κ_{sc} . The single atom cooperativity is defined as $C = 4g^2/(\kappa\gamma)$. The measured reflection spectra correspond to $|r(\omega)|^2$. The entanglement protocol implemented in

this work is done with the atom, cavity and probe photons on resonance, in which case the reflectivity simplifies to

$$R = |r|^2 = \left| 1 - \frac{2\kappa_{wg}}{\kappa} \frac{1}{C} \right|^2 \quad (\text{B.1.2})$$

showing highly nonlinear dependence on cooperativity. For our measured cooperativity, the atom-cavity system acts as a near-perfect mirror already with a single coupled atom.

The reflection spectrum in Fig. 1B is fitted using the theoretical model described in [114]. According to this model, the thermal motion of a trapped atom next to the cavity results in a distribution of cooperativities sampled by the atom. Using the independently measured radial trap frequency of $2\pi \times 115$ kHz, axial trap frequency of $2\pi \times 550$ kHz, and final temperature of $T = 70$ μK , we fit for the cooperativity an atom would experience if it were stationary and obtain $C_0 = 47(1)$. The distribution of the cooperativities an individual atom samples has a mean value of $27(1)$, and a standard deviation of $25(2)$. We adjust the trap positions relative to the cavity mode to match the mean cooperativities for each atom while not overlapping their traps, resulting in a 2.1 μm distance between the atoms centered around the mode maximum. At the mode maximum of the cavity the mean single-atom cooperativity is measured to be $71(4)$ [114].

B.2 Experimental sequence

The total run time can be separated into periods of experimental run ($\sim 85\%$ of the total time), equipment programming, and setup calibration. Confocal tracking of the cavity position accounts for most of the setup calibration and is needed to consistently move atoms to the same position in the cavity mode. This is achieved by imaging the cavity in different focal planes for 2 minutes every 25 minutes and recalibrating the coordinates for each dipole trap.

A typical experimental sequence is outlined in Fig. B.1. We load atoms from a magneto-optical trap with the tweezers positioned $50 \mu\text{m}$ from the cavity [114]. Each experimental trial begins upon detection of atomic fluorescence indicating presence of both atoms. At this position, we perform polarization gradient cooling (PGC) and bring the temperature of the atoms down to $15 \mu\text{K}$. The dipole traps are subsequently moved to the cavity with galvanometer mirrors. During transport, the trap transforms from a Gaussian beam into a 1D optical lattice with tight axial confinement due to its reflection from the PCC. The increase in the trap frequencies results in a higher atomic temperature. To counteract this heating, we apply PGC again while attempting to load the atoms into the first lattice site closest to the PCC. We achieve 80% single atom loading probability with a final temperature of $70 \mu\text{K}$, up from a 50% loading probability without cooling during loading. While at the cavity, the atoms experience a higher heating rate than in free space, reducing their trap lifetime to 180 ms. Photon

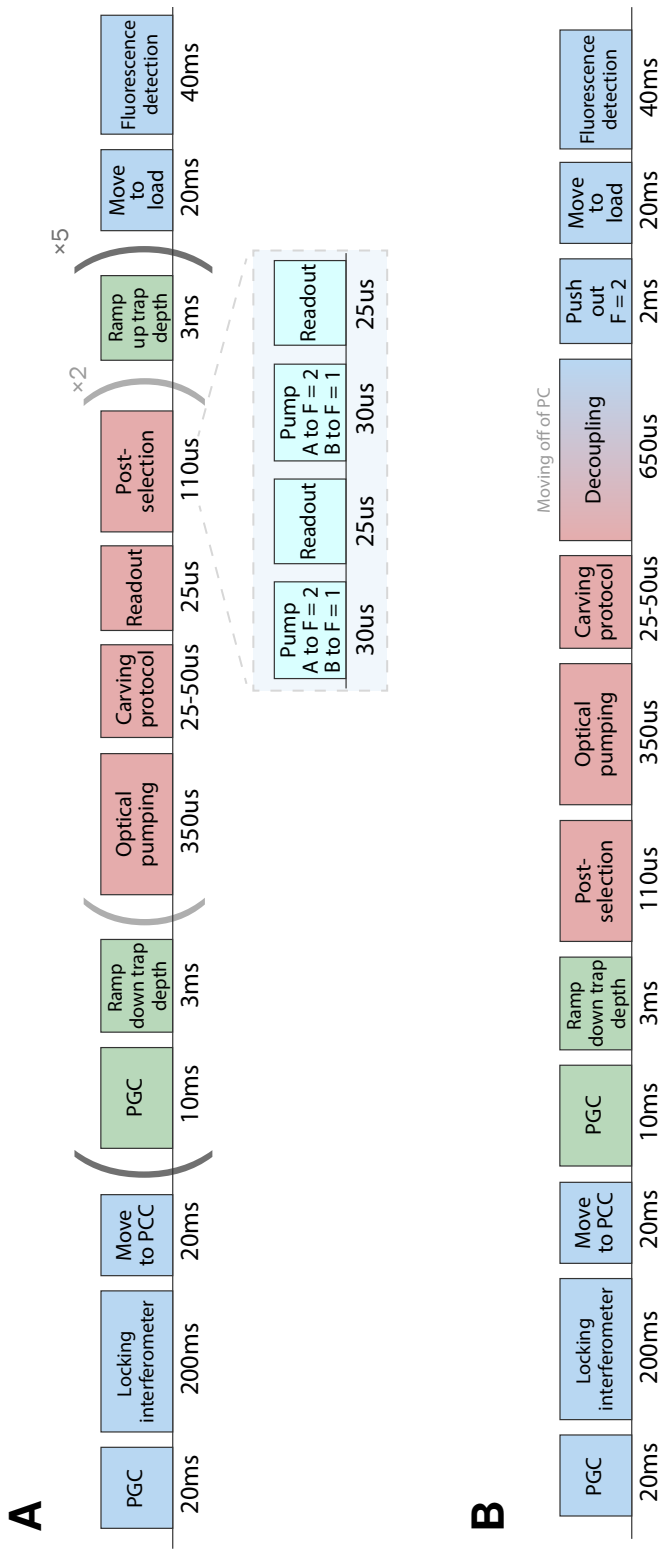


Figure B.1: Experimental sequence. **(A)** Time breakdown of a typical two-atom entanglement sequence between atom-A and atom-B. **(B)** An experimental sequence for the coherent transport of the atomic states that incorporates phases both at the cavity (red and green) and in free space (blue).

scattering due to state readout through the cavity causes additional heating, limiting the number of experimental repetitions at the cavity. We extend this by re-cooling the atoms every two repetitions. To reduce light shift-induced inhomogeneities, we reduce the trap depth from $2\pi \times 50$ MHz to $2\pi \times 32$ MHz before preparing the qubit state (see Section 2.1 below). While we repeat the qubit preparation and entanglement protocol 10 times, an atom on average is present for 4 of those iterations.

Since the atoms can be heated out of the traps during the experimental attempts, we postselect the experiments based on atomic presence detected via the cavity. As shown in Fig. 1C, the cavity reflection cannot distinguish the number of coupled atoms. By adding individual addressing beams, co-propagating with the dipole traps and resonant with the $5S_{1/2} \rightarrow 5P_{1/2}$ transition, we can selectively pump either atom to the coupled state ($F = 2$) while leaving the other in the uncoupled state ($F = 1$). This allows us to perform entanglement experiments where both atoms are loaded with >99%, and to overcome the common problem of probabilistic loading from which all nanophotonic platforms suffer [87, 73, 156].

Combining the probabilistic loading at the cavity, the two-atom initial trigger rate, and the single photon detection rate for the entanglement experiments gives a Bell pair generation rate of 0.5 events/min. The largest contribution to the low data rate is the number of collected photons from the coupled level during the gate pulse. The total number of collected photons is equal to $N_{collected} = T_{int}\eta N_{sent}$, where $\eta = 0.28$ is the total detection efficiency, $N_{sent} = 0.35$ is the number of photons sent to the cavity,

and $T_{int} = 0.1$ is the throughput from the interferometer in the undercoupled cavity regime. We discuss the interferometer throughput T_{int} in detail in the section about the entanglement scheme implementation. The total detection efficiency η consists of the single-photon counter (PerkinElmer SPCM-AQR-16-FC) quantum efficiency (0.6), fiber taper coupling efficiency (0.6), and loss from the optical path (0.8).

B.2.1 State preparation

To prepare an atom in the qubit state $|F, m_F\rangle = |1, 0\rangle \equiv |0\rangle$ we perform a frequency-selective Raman-assisted optical pumping protocol. The protocol consists of sequentially pumping the atomic population into the $F = 1$ ground state manifold followed by driving $|1, \pm 1\rangle \rightarrow |2, \pm 1\rangle$, leaving the target qubit state dark. The latter is accomplished through driving Raman transitions between the two ground state hyperfine manifolds with a circularly polarized beam. This beam is 100 GHz detuned from the $5S_{1/2} \rightarrow 5P_{1/2}$ transition and contains two frequency components detuned by the hyperfine splitting of 6.8 GHz generated by an amplitude modulator (Jenoptik AM785). It co-propagates with one of the dipole traps through the objective and is large enough to equally address both atoms which are separated by $2.1 \mu\text{m}$. We begin the optical pumping cycle with the atomic population coarsely pumped to $F = 1$, prepared with the MOT beams tuned to the $F = 2 \rightarrow F' = 2$ transition. The Raman beat note is generated by IQ up-conversion of direct digital synthesizers (Novatech 409B) mixed with the microwave

source (SRS SG384). The DDS pulses can be switched rapidly to sequentially drive the $|1, \pm 1\rangle \rightarrow |2, \pm 1\rangle$ ground state transitions, thus leaving the final population in $|1, 0\rangle$ (Fig. B.2). Afterwards, we apply the global MOT beams again to pump the population from $F = 2$ back to $F = 1$. We repeat this cycle 40 times, with each Raman pulse taking 2 μs and the MOT pumping pulse taking 2.2 μs . The optical pumping sequence takes 340 μs in total and results in 0.98(2) preparation fidelity in $|1, 0\rangle$. The optical pumping fidelity estimation is extracted via the Rabi oscillation contrast (Fig. 1D), where the $|1, 0\rangle \rightarrow |2, 0\rangle$ transition is driven and the resulting $F = 2$ population is read out with the cavity. This optical pumping fidelity is corrected for the cavity readout infidelity. Our optical pumping scheme overcomes the challenge of maintaining polarization purity near the PCC, where the atom samples near-field polarization variation of an optical field reflected from the nanostructure. This makes other polarization-based optical pumping schemes inapplicable for high-fidelity state preparation. However, our scheme only relies on frequency selectivity between the different magnetic sublevels, enabled by a Zeeman shift of 12 MHz ($B = 17$ Gauss).

B.2.2 Two-atom readout in free space

The experiments described in the main text performed with tweezers positioned away from the PCC rely on the standard push-out state detection. We apply pulses resonant with the $F = 2 \rightarrow F' = 3$ transition that remove atoms in $F = 2$ and record fluorescence

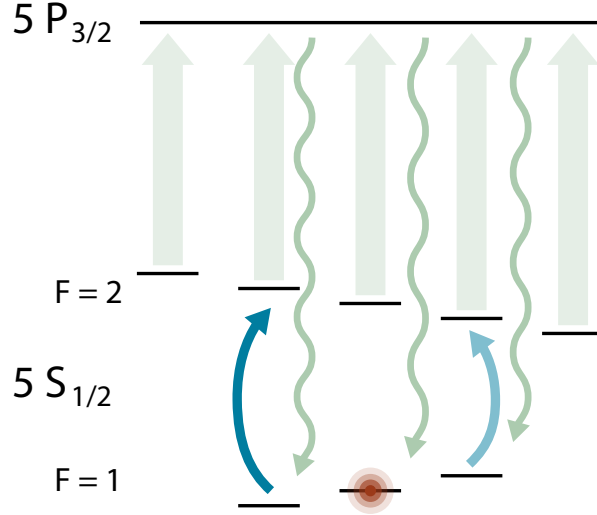


Figure B.2: An illustration of the Raman-assisted state preparation. Cycling between repumping the atom into $F = 1$ (green), depleting the population in $m_F = \{-1, 1\}$ (blue), and leaving the atom in $|1, 0\rangle$.

to detect atoms remaining in $F = 1$. The push-out pulses and fluorescence detection are performed $\sim 1 \mu\text{m}$ and $50 \mu\text{m}$ away from the PCC respectively. We characterize the readout contrast by preparing the atoms in the $F = \{1, 2\}$ manifolds at the PCC, moving away the tweezers at a trap depth of $2\pi \times 32 \text{ MHz}$, and performing the push-out readout, obtaining the retention probability of $\sim \{0.80, 0.05\}$. We recalibrate the retention levels every half an hour in parallel with running the entanglement experiments. The finite retention of $F = 2$ is limited by imperfections in the push-out procedure. The retention of $F = 1$ is primarily limited by transport loss ($\sim 15\%$) and loss from collisions with the MOT atoms during the imaging ($\sim 5\%$). The transport loss depends on the trap depth and initial temperature, and for our parameters can be suppressed at a trap depth of

$2\pi \times 50$ MHz.

As the finite contrast of the push-out detection limits the single-shot detection fidelity, we infer the population components from the readout probability after collecting meaningful statistics based on the readout calibration described above. In the case of two-atom experiments, the probabilities of retention \mathcal{R} are given by

$$\mathcal{R} = \begin{pmatrix} R_{00} \\ R_{01} \\ R_{10} \\ R_{11} \end{pmatrix} = \mathcal{K} \begin{pmatrix} P_{00} \\ P_{01} \\ P_{10} \\ P_{11} \end{pmatrix}, \quad (\text{B.2.1})$$

where R_{ij} denotes the results corresponding to the four possibilities of retention of the two atoms, P_{ij} are the populations in the corresponding two-atom states, and \mathcal{K} is a correction matrix given by

$$\begin{aligned} \mathcal{K} &= \mathcal{K}_{\mathcal{A}} \otimes \mathcal{K}_{\mathcal{B}} \\ &= \begin{pmatrix} h_A h_B & h_A(1 - h_B) & (1 - h_A)h_B & (1 - h_A)(1 - h_B) \\ h_A l_B & h_A(1 - l_B) & (1 - h_A)l_B & (1 - h_A)(1 - l_B) \\ l_A h_B & l_A(1 - h_B) & (1 - l_A)h_B & (1 - l_A)(1 - h_B) \\ l_A l_B & l_A(1 - l_B) & (1 - l_A)l_B & (1 - l_A)(1 - l_B) \end{pmatrix}^T \end{aligned} \quad (\text{B.2.2})$$

where $\{h_i, l_i\}$ denote the retention probabilities of atom i prepared in $F = \{1, 2\}$. For

State	Mean	Confidence interval
$ 00\rangle$	0.956	[0.936, 0.975]
$ 01\rangle$	0.949	[0.922, 0.964]
$ 10\rangle$	0.948	[0.921, 0.961]
$ 11\rangle$	0.991	[0.987, 0.996]

Table B.1: Readout fidelities of different two-atom states

a generic two-atom measurement, we multiply the inverse of the correction matrix with the measurement result to obtain the populations [157].

B.2.3 Readout through the cavity

The measurements in Fig. 1 and 3 in the main text were done by reading the atomic states using the cavity reflection. As shown in the Fig. 1C, readout through the PCC distinguishes the state $|00\rangle$ from the rest of the states in the two qubit manifold. By integrating for 25 μ s and choosing a photon count threshold, we perform a single shot readout which distinguishes $|00\rangle$ from the other states with the fidelities reported in Table B.1. The confidence intervals for the fidelities were obtained by changing the threshold by ± 1 photon.

B.3 Fidelity extraction from parity

To characterize the state after the carving protocol and its overlap with $|\Phi^+\rangle$, we perform two sets of measurements. In the first we measure the populations P_{00} and P_{11} and in the

second we measure the parity oscillations of the state $|\Phi^+\rangle$. The populations in $|00\rangle$ and $|11\rangle$ are extracted by reading out the states without and with a global π pulse applied before the cavity reflection detection respectively. Using the normalization condition $\sum P_{ij} = 1$, we also extract the population in the odd states, $P_{odd} = P_{01} + P_{10} = 1 - (P_{00} + P_{11})$. We can therefore measure the parity of the state, defined as

$$\Pi \equiv P_{00} - P_{01} - P_{10} + P_{11} = 2(P_{00} + P_{11}) - 1 \quad (\text{B.3.1})$$

We calculate the fidelity of preparing the Bell state $|\Phi^+\rangle$ as $\mathcal{F} = \langle\Phi^+|\rho|\Phi^+\rangle = \frac{1}{2}(\rho_{00,00} + \rho_{11,11} + \rho_{00,11} + \rho_{11,00})$ by measuring the populations $\{\rho_{00,00}, \rho_{11,11}\}$ and the coherences $\{\rho_{11,00} = \rho_{00,11}^*\}$. The total population is directly measured from the cavity readout. The coherence is recorded after a $\pi/2$ rotation over a variable axis ϕ [126, 96] and is extracted from the amplitude of the parity oscillation as

$$\Pi(\phi) = 2 \operatorname{Re}(\rho_{10,01}) + 2 \operatorname{Im}(\rho_{11,00}) \sin(2\phi) + 2 \operatorname{Re}(\rho_{11,00}) \cos(2\phi) \quad (\text{B.3.2})$$

Combining these two measurements gives the reported fidelity of $\mathcal{F} = 0.72(3)$. Note that the data in Fig. 3 and the reported entanglement fidelity at the PCC are not corrected for the finite readout fidelity.

The fidelity measurement after the transport is done in an analogous way. All four populations P_{ij} are extracted from the free space fluorescence detection. The phase of

the coherence term $2\phi_0 = \arg(\rho_{11,00})$ is calibrated using each individual atom's Ramsey fringes, after which the resulting two-atom state coherence is extracted from the difference in the parity measurements $\Pi(\pi/2) - \Pi(0)$ between the bases {parallel, orthogonal} to ϕ_0 , labeled { XX , YY } (Fig. 4B). Combining this measurement with the populations (ZZ basis) gives the measured fidelity of $\mathcal{F} = 0.65(5)$.

B.4 Concurrence bound

Concurrence is a basis-independent measure of how entangled a state is, and is therefore a more general entanglement measure than the fidelity of preparing a certain state. In practice, measuring the concurrence requires knowledge of the full density matrix of the prepared state and, therefore, a lower bound is often used to check if a state is entangled [158]. A concurrence of $C > 0$ proves entanglement.

Given the amplitude of the parity oscillations we obtain a lower bound on the concurrence, following [119]. In the ZZ basis, we primarily prepare $|\Phi^+\rangle = 1/\sqrt{2}(|00\rangle + |11\rangle)$. The lower bound for the concurrence is then

$$\mathcal{C} \geq 2(|\rho_{00,11}| - \sqrt{\rho_{01,01}\rho_{10,10}}) \quad (\text{B.4.1})$$

Using the Eqn. B.4.1, we directly extract concurrence after moving of $\mathcal{C} \geq 0.35(11)$. At the cavity we only measure the sum of the two populations $P_{01} + P_{10} = 0.22 \pm 0.03$.

To get a lower bound, we want the maximum of their product, which occurs when they are equal $P_{01} = P_{10}$. Using this, we extract $\mathcal{C} \geq 0.46(5)$.

B.5 Entanglement scheme using the interferometer

The entanglement fidelity of the coherent photon reflection protocol is determined by the reflection amplitudes of different two-atom basis states. In turn, the reflection amplitudes determine the optimal initial rotation angle θ . The four qubit states have reflectivities given by equation B.1.2, which for our parameters are $R_{00} = 0.40$, $R_{01} = R_{10} = 0.94$, $R_{11} = 0.97$. Since the entanglement protocol relies on distinguishing $|01\rangle$, $|10\rangle$ and $|11\rangle$ from $|00\rangle$ as well as possible, we add an interferometer to the detection path to eliminate the uncoupled reflectivity R_{00} . The cancellation is achieved using a Mach-Zehnder interferometer, with the relative phase tuned for destructive interference of the uncoupled reflectivity (Fig. B.3). In this way, any cavity with a finite reflectivity on resonance can be used to implement entanglement via photon carving. The interferometer can be switched on and off during an experiment by changing the AOM driving amplitudes to allow for both the single photon gating (interferometer on) and atomic state detection (interferometer off).

In the case of a perfect interferometer, we would have $R_{00} \rightarrow 0$, yielding a fidelity of

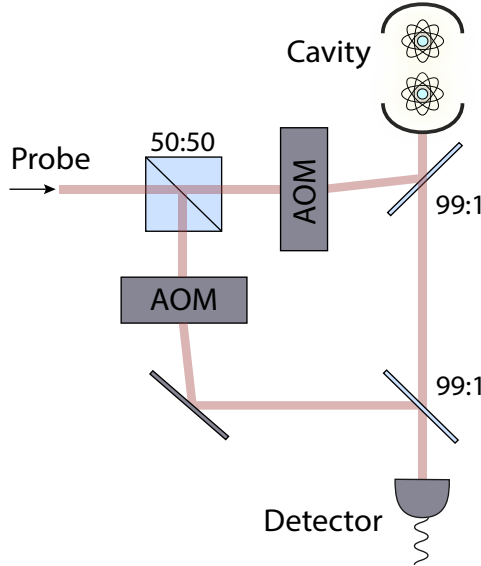


Figure B.3: Sketch of the interferometer in the detection path used to improve the reflection contrast between an empty and a coupled cavity.

$\mathcal{F} = 1/(1 + \tan(\theta/2))^2$, which in principle can be $\mathcal{F} \rightarrow 1$ with an infinitesimally small angle θ . The contrast of our interferometer is limited by the noise on the cavity lock to $(R_{max} - R_{min})/(R_{max} + R_{min}) = 0.96$. This gives finite reflectivities to all the states, such that after a postselection on the reflected photon, we are left with the components of both states $|00\rangle$ and $|11\rangle$ as error terms. For a given interferometer contrast, there is an optimal initial rotation angle that balances the infidelities. The dependence of the maximal Bell state fidelity on the interferometer contrast and the initial angle is shown in Fig. B.4 (left panel). For our interferometer contrast, we choose the initial angle of 0.3π , and expect the maximal fidelity of 0.76. Given an initial angle and interferometer contrast, one can calculate the probability of having a photon reflected

from the atom-cavity system, which for our parameters is $T_{int} = 0.1$.

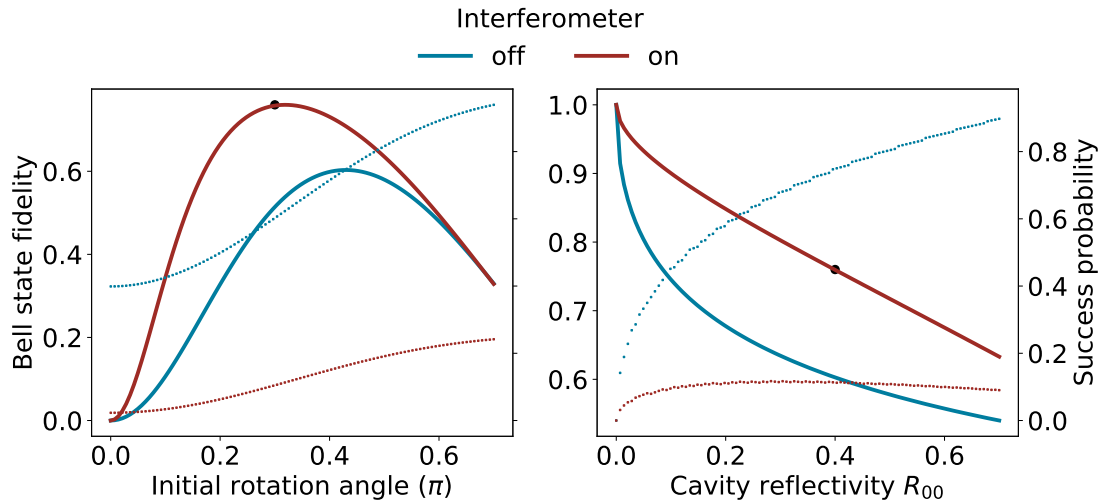


Figure B.4: Parameters that determine the entanglement fidelity. (Left) Dependence of the maximal Bell state fidelity (solid lines, left y axis) and protocol success probability (dotted lines, right y axis) on the initial angle and interferometer contrast. Not using the interferometer would limit the maximal fidelity to ~ 0.6 . With our measured interferometer contrast of 0.96, the fidelity is limited to 0.76 (black dot). (Right) Keeping the interferometer contrast the same, the protocol maximal fidelity can be improved by using a cavity with a smaller reflectivity R_{00} .

The protocol can be improved using a cavity with a smaller R_{00} , given that the maximal fidelity is intrinsically bounded by this value. Note that for our cavity linewidth the uncoupled reflectivity R_{00} is equivalent to the empty cavity reflectivity. Fig. B.4 (right panel) shows the dependence of the maximal fidelity and success probability on R_{00} . Assuming that the interferometer contrast stays the same, the fidelity can be improved to 0.9 by reducing R_{00} from 0.4 (our parameter, black dot in the figure) to 0.1. Finally, the tradeoff between the fidelity and the success probability is demonstrated by

the opposite slopes of the solid and dotted curves in Fig. B.4.

B.6 Theoretical models for the entanglement protocol

B.6.1 Coherent model

Ideally, the carving protocol for entanglement generation is fully coherent and results in a pure state. Here we model the effect of a coherent photon reflection and post-selection on detection. The model assumes that the photons reflected from different two-atom states differ by the reflection probability but are otherwise completely indistinguishable. Under this assumption, throughout the experiment the two atoms are in pure states, which are different superpositions of the Bell triplet states $|\Phi^\pm\rangle$ and $|\Psi^+\rangle$. The target entangled state from the main text is $|\Phi^+\rangle$, and we define the entanglement fidelity as the overlap $\mathcal{F} = \langle \Phi^+ | \rho | \Phi^+ \rangle$.

We define the phase of our rotations such that a native rotation is over the axis x, so that after a rotation by angle θ we obtain $R_{0,\theta}|00\rangle = |\Psi_\theta\rangle$:

$$|\Psi_\theta\rangle = \cos^2\left(\frac{\theta}{2}\right)|00\rangle - \sin^2\left(\frac{\theta}{2}\right)|11\rangle - i \sin\left(\frac{\theta}{2}\right) \cos\left(\frac{\theta}{2}\right) (|01\rangle + |10\rangle) \quad (\text{B.6.1})$$

After preparing the state $|\Psi_\theta\rangle$, we reflect a photon and post-selecting on its detection.

Given the reflection amplitudes for each state (r_{00} , r_{01} , r_{10} , r_{11}), we are left with

$$|\Psi^{cond}\rangle = \frac{1}{N} (r_{00} \cos^2\left(\frac{\theta}{2}\right) |00\rangle - r_{11} \sin^2\left(\frac{\theta}{2}\right) |11\rangle - i r_{01} \sin\left(\frac{\theta}{2}\right) \cos\left(\frac{\theta}{2}\right) (|01\rangle + |10\rangle)) \quad (\text{B.6.2})$$

where N is a normalization factor. If we relabel different state amplitudes as $\epsilon_0 = r_{00} \cos^2\left(\frac{\theta}{2}\right) / N$, $\epsilon_1 = r_{11} \sin^2\left(\frac{\theta}{2}\right) / N$, and $f = r_{01} \sqrt{2} \sin\left(\frac{\theta}{2}\right) \cos\left(\frac{\theta}{2}\right) / N$, we can rewrite the state $|\Psi^{cond}\rangle$ as

$$\begin{aligned} |\Psi^{cond}\rangle &= \epsilon_0 |00\rangle - \epsilon_1 |11\rangle - i f |\Psi^+\rangle \\ &= \left(\frac{\epsilon_0 - \epsilon_1}{\sqrt{2}} \right) |\Phi^+\rangle + \left(\frac{\epsilon_0 + \epsilon_1}{\sqrt{2}} \right) |\Phi^-\rangle - i f |\Psi^+\rangle \end{aligned} \quad (\text{B.6.3})$$

Before analyzing the state, we apply $R_{0,\pi/2}$ and get the final state in the ZZ basis

$$\begin{aligned} |\Psi_{zz}\rangle &= R_{0,\pi/2} \otimes R_{0,\pi/2} |\Psi^{cond}\rangle \\ &= -i \left(\frac{\epsilon_0 - \epsilon_1}{\sqrt{2}} \right) |\Psi^+\rangle + \left(\frac{\epsilon_0 + \epsilon_1}{\sqrt{2}} \right) |\Phi^-\rangle - f |\Phi^+\rangle \end{aligned} \quad (\text{B.6.4})$$

Based on equation B.6.4, the entanglement fidelity is given by $\mathcal{F} = |f|^2$. The idea of the "cavity carving" protocol is to maximize the amplitude f . This can be done by 1) having ($r_{00} \ll r_{01} \approx r_{11}$), which would result in a small ϵ_0 , and 2) using a small initial rotation angle θ , which would result in a small ϵ_1 .

From equation B.6.4 we can determine the population in the four basis states:

$$P_{00} = \frac{1}{2} \left| \frac{\epsilon_0 + \epsilon_1}{\sqrt{2}} - f \right|^2 \quad (\text{B.6.5})$$

$$P_{11} = \frac{1}{2} \left| \frac{\epsilon_0 + \epsilon_1}{\sqrt{2}} + f \right|^2 \quad (\text{B.6.6})$$

$$P_{01} = P_{10} = \frac{1}{4} |\epsilon_0 - \epsilon_1|^2 \quad (\text{B.6.7})$$

Note that finite values of ϵ_0 and ϵ_1 cause the populations in $|00\rangle$ and $|11\rangle$ to be unbalanced (as seen in Fig. 3b).

B.6.2 Mixed model

The coherent model above assumes that the post-selection on the reflected photon leaves the system in a pure state. However, spontaneous scattering and temporal mismatch can both reveal the which-path information of photons reflected from $|00\rangle$. When the photons reflected from the uncoupled and coupled states are distinguishable, the system is left in a mixed state. Spontaneous scattering from the gate photons in the coherent pulses containing more than one photon leave the atom in a different hyperfine level within the $F = 2$ manifold. In addition, while the response from the state $|0\rangle$ is instantaneous, the bandwidth of the response from the state $|1\rangle$ is $C\gamma$ and may lead to a temporal mismatch. The atom samples a distribution of cooperativities due to thermal motion, which for $C \sim 1$ results in a 26 ns delay in the atomic response. This

is longer than the pulse duration of 20 ns (FWHM), which would make the photons distinguishable.

We can model distinguishability by assuming that a photon reflection corresponds to the following projections:

$$M_u = |00\rangle \langle 00| \quad (\text{B.6.8})$$

$$M_c = \mathbb{1} - M_u \quad (\text{B.6.9})$$

If the probability that a detected photon was reflected from $|00\rangle$ is p_u , and from the coupled manifold is $p_c = 1 - p_u$, post-selection on a photon detection projects the system into

$$\rho' = p_u M_u \rho M_u^\dagger + p_c M_c \rho M_c^\dagger \quad (\text{B.6.10})$$

where ρ is the density matrix of the state before reflection, $\rho = |\Psi_\theta\rangle \langle \Psi_\theta|$ (Eqn. B.6.1). The probability p_u can be calculated as the ratio of effective reflectivities of the uncoupled and coupled states (assuming that $R_{10} \approx R_{11}$):

$$p_u = \frac{R_{00}}{R_{00} + R_{01}} \quad (\text{B.6.11})$$

In the case of using an interferometer, R_{00} and R_{01} would correspond to reflectivities with the interferometer engaged. For our measured interferometer contrast of 0.96, $p_u = 0.087$.

The mixed model differs from the coherent model in that the reflection post-selection destroys the initial coherences between $|00\rangle$ and the coupled states: $\rho_{00,01}$, $\rho_{00,10}$, $\rho_{00,11}$. When the state is further rotated and analyzed, such as in the populations and parity oscillation measurement, this will result in different theoretical predictions. However, we note that the entanglement fidelity prediction of the two models is identical, since the entanglement relies on the reflection preserving the initial coherence between $|01\rangle$ and $|10\rangle$ ($\rho_{01,10}$) after the gate pulse, which happens in both models. We confirm this statement numerically, by calculating the overlap with $|\Phi^+\rangle$ with different models, and arriving at the same values.

Given that both the coherent and the mixed model give predictions for the state populations and measured parity, we now compare them with the measured data. Figure B.5 shows the experimental measurement (blue), predictions from the coherent model (green) and mixed model (red) for the parity oscillation (left panel) and ZZ basis populations (right panel). The mixed model agrees better with the measurements in both datasets.

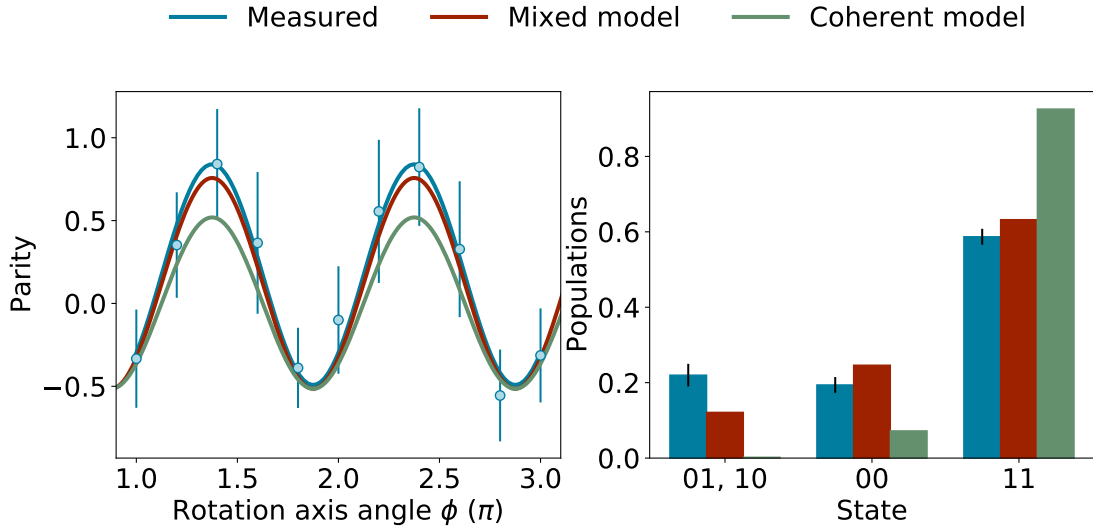


Figure B.5: Comparison of the experimental measurements (blue), mixed model predictions (red) and coherent model predictions (green) for the parity measurement (left panel) and the ZZ basis populations (right panel).

B.7 Coherence properties of atoms next to the photonic crystal cavity

The qubit relaxation time T_1 in our system is limited by contributions of various scattering processes. The tweezer depth next to the PCC (32 MHz) would limit T_1 to 60 ms. However, with the cavity tuned into resonance with the atom, we observe additional scattering significantly reducing T_1 to 1.2 ms. With the cavity tuned 14κ away from the atomic resonance, we recover the expected T_1 . For the experiments that require long coherence, such as for atomic state transport, we detune the cavity right after the gate by jumping the cavity lock in sequence. The source of the resonant scattering remains

under investigation.

Magnetic-field-insensitive qubit encoding minimizes the influence from vector light shifts, a near-field effect intrinsic to tightly-focused light, and further exacerbated by the standing wave potential next to the PCC [60]. The spin dephasing is characterized by the transverse decay time T_2 and is primarily limited by thermal motion leading to varying differential AC Stark shifts. This dephasing can be decomposed into the reversible (T_2^*) and the irreversible (T_2') component as $1/T_2 = 1/T_2' + 1/T_2^*$. Shown in Fig. B.6A is a Ramsey decay measurement ($\pi/2 - \tau - \pi/2$) of an atom next to the PCC, giving a $T_2 = 0.35(4)$ ms. As discussed in [120, 121], the main source of reversible dephasing in optical dipole traps is atomic motion coupled with a finite differential light shift. If we assume that the energy distribution of atoms in the trap obeys the Boltzmann distribution with temperature T , the reversible dephasing time T_2^* can be expressed as $T_2^* = 2\hbar/(\zeta k_B T)$ [120]. The factor ζ depends on the dipole trap wavelength and the atomic energy spectrum. We experimentally confirm the linear dependence of $1/T_2$ on the temperature, and measure $\zeta = 5.4 \times 10^{-4}$ (Fig. B.6B). The dephasing induced by a constant temperature can be reversed with a spin echo sequence.

Using the spin echo sequence ($\pi/2 - \tau - \pi - \tau - \pi/2$), we measure $T_2' = 9.7(8)$ ms in free-space, and $T_2' = 2.1(1)$ ms at the cavity. The difference cannot be explained with the sources common to the free space and the PCC such as fluctuating magnetic fields, microwave power and pulse duration, and we attribute it to extra heating at the cavity. Any heating process would translate to irreversible dephasing, in the same way constant

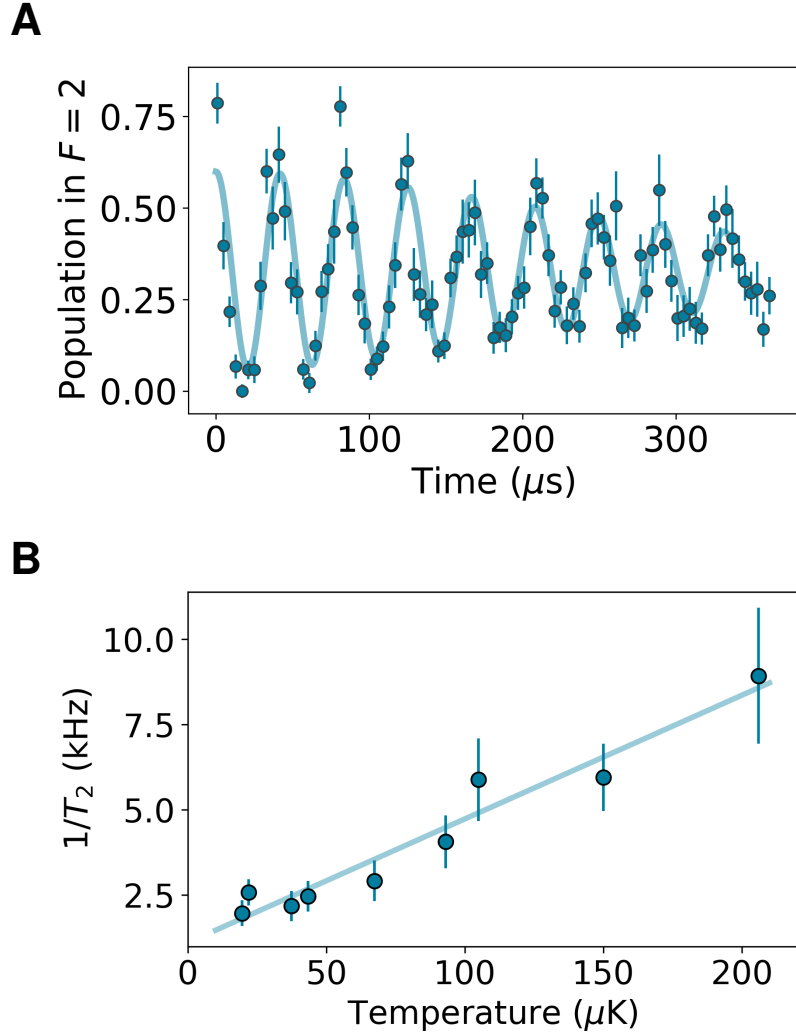


Figure B.6: Temperature-limited Ramsey decay. **(A)** Ramsey decay of an atom next to the PCC fitted using the model described in [120], giving $T_2 = 0.35(4)$ ms. **(B)** Linear dependence of the Ramsey dephasing rate on the initial temperature.

temperature causes reversible dephasing. At the cavity, we measure a lifetime of 180(7) ms at a trap depth of 2.7 mK (Fig. B.7), giving a heating rate of 14.6 mK/s, an order of magnitude higher than in free space. The irreversible dephasing time depends on the

heating rate as $T'_2 \propto (dT/dt)^{-1/2}$ [120].

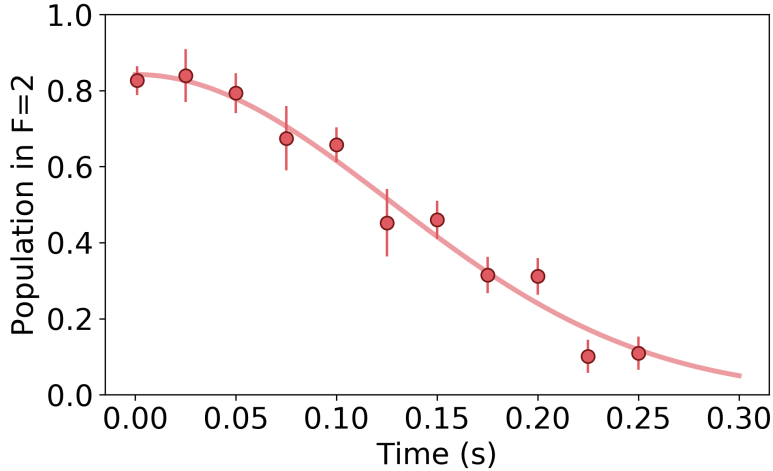


Figure B.7: Measured lifetime of $180(7)$ ms at a trap depth of 2.7 mK next to the photonic crystal cavity.

Two main sources of heating we consider are the trap potential fluctuations and the atomic recoil due to scattering. To estimate the heating rate due to atomic recoil, we use the scattering rate given by $1/T_1$, and obtain $dT/dt = 4.1 \cdot 10^{-3}$ mK/s (cavity out of lock) and 0.15 mK/s (cavity in lock). Both estimates are orders of magnitude away from the lifetime-deduced heating rate. Therefore, we speculate that the contributions to additional heating near the nanophotonic cavity include the trap fluctuations due to mechanical vibrations of the nanostructure [122] and the higher sensitivity of the axial trap frequency to the fast intensity noise [159].

B.8 Phase accumulation while moving

B.8.1 Dipole potential for different trap configurations

The potential energy of a two-level system in a detuned optical field in the rotating-wave approximation is given by:

$$U(r) = \frac{3\pi c^2 \gamma}{2\omega_0^3 \Delta} I(r)$$

where Δ is the field detuning, γ the spontaneous emission rate, and $I(r)$ the intensity of the field [160]. When the field is red-detuned ($\Delta < 0$), the atoms are attracted to the maximum of the field intensity $I(r)$. Based on the different configurations of the laser beams, $I(r)$ can have different spatial dependence, resulting in different effective trap frequencies. In our experiment, we change the trapping configuration from a focused Gaussian beam to a standing wave, and here we will explore how the potential changes for those two configurations.

A focused Gaussian beam creates a potential

$$U(r, z) = U_0 \exp \frac{-2r^2}{w(z)^2} \quad (\text{B.8.1})$$

where $w(z) = w_0 \sqrt{1 + \frac{z^2}{z_r^2}}$, w_0 is the beam waist, and $z_r = \pi w_0^2 / \lambda$ is the Rayleigh range.

Expanding this expression around $r, z = 0$ gives

$$U(r, z) \approx -U_0 \left(1 - 2 \left(\frac{r}{w_0} \right)^2 - \left(\frac{z}{z_r} \right)^2 \right) \quad (\text{B.8.2})$$

which can be rewritten as a harmonic potential in the radial and axial direction

$$U(r, z) \approx -U_0 + \frac{1}{2} m \omega_r^2 r^2 + \frac{1}{2} m \omega_z^2 z^2 \quad (\text{B.8.3})$$

with the oscillator frequencies $\omega_r = \sqrt{\frac{4U_0}{mw_0^2}}$ and $\omega_z = \sqrt{\frac{2U_0}{mz_r^2}}$. When the atoms are near the nanophotonic cavity, part of the tweezer beam is reflected back and interferes with the forward-propagating beam. The tweezer then forms a standing wave potential of the form

$$U(r, z)' = -\alpha U_0 \cos(kz)^2 \left(1 - 2 \left(\frac{r}{w_0} \right)^2 - \left(\frac{z}{z_r} \right)^2 \right) \quad (\text{B.8.4})$$

where α is the interference contrast (measured to be $\alpha = 1.2$ in our experiment), and $k = 2\pi/\lambda_0$. Expanding this expression and rewriting it as a harmonic potential gives the oscillator frequencies $\omega'_r = \sqrt{\frac{4\alpha U_0}{mw_0^2}}$ and $\omega'_z = \sqrt{\frac{2\alpha U_0}{mz_\lambda^2}}$, where $z_\lambda = \lambda_0/(2\pi)$. Therefore, moving from the focused beam to a standing wave changes the oscillator frequencies from $\omega_r \rightarrow \omega'_r$ and $\omega_z \rightarrow \omega'_z$.

B.8.2 Differential light shift during the transport

The main contribution to the shift of the qubit resonance for the magnetic field insensitive states is the differential light shift. For a given maximal light shift U_0 , the differential light shift δ_0 is given by

$$\hbar\delta_0 = \zeta(-U_0 + \overline{E_p}) \quad (\text{B.8.5})$$

where $\zeta \propto \omega_{HFS}/\Delta$ ($\zeta = 5.4 \times 10^{-4}$ for our system), and $\overline{E_p}$ is the average potential energy of the atom in the trap. From the virial theorem, $\overline{E_p} = \overline{E}/2$. For the three-dimensional harmonic oscillator, the average total energy is given by

$$\overline{E} = \sum_{i=x,y,z} \hbar\omega_i \left(\frac{1}{2} + \frac{1}{\exp \frac{\hbar\omega_i}{k_b T} - 1} \right) = \sum_{i=x,y,z} \hbar\omega_i \left(\frac{1}{2} + n_i \right) \quad (\text{B.8.6})$$

where T is the temperature of the atom, and n_i is the average occupation number in the direction i . Combining the equations B.8.5 and B.8.6, we arrive at the expression for the differential light shift of a moving atom:

$$\delta_0(t) = -\zeta \frac{U_0(t)}{\hbar} + \frac{\zeta}{2} \left(2\omega_r(t) \left(\frac{1}{2} + n_r(t) \right) + \omega_z(t) \left(\frac{1}{2} + n_z(t) \right) \right) \quad (\text{B.8.7})$$

As seen in the previous section, $U_0(t)$, $\omega_r(t)$ and $\omega_z(t)$ necessarily vary in time as the trap potential changes. The average occupation number $n_i(t)$ depends on whether the

atom makes motional state transitions during the transport. If the trap deformation is adiabatic, the atom does not change the motional energy level and $n_i = \text{const}$. This is equivalent to $\omega(t)/T(t) = \text{const}$, which would imply an increase in temperature as the trap frequency increases (adiabatic heating) and vice-versa (adiabatic cooling)[161]. The entire time dependence of $\delta_0(t)$ would then be in $U_0(t)$, $\omega_r(t)$ and $\omega_z(t)$. If the atom does make motional state transitions because of the noise in the trapping potential, $\delta_0(t)$ will stochastically vary and cause qubit dephasing.

B.8.3 Phase accumulation and cancellation

Given that δ_0 varies in time as shown in the equation B.8.7, a moving atom will acquire a phase shift $\phi(T) = \int_0^T \delta_0(t) dt$. If the detuning ramp during transport is the same for every atom, i.e. if the acquired phase is constant, it can be corrected for with a local σ_z gate.

We apply a voltage ramp $V(t) \propto \tanh(t)$ to the scanning mirrors to move the atoms. If the atoms were following the mirror position instantaneously, the detuning ramp would have a shape plotted in Fig. B.8. The ramp is symmetric with respect to $T/2$. An even number of π pulses in a Carr-Purcell (CP: $\pi/2 - (\tau - \pi - \tau)^N - \pi/2$) sequence would cancel out the acquired phase. The statistical variations in the total energy in one experimental run coming from a finite temperature would make the detuning ramp have a varying offset (Fig B.8A), the same as the variation that limits the free precession

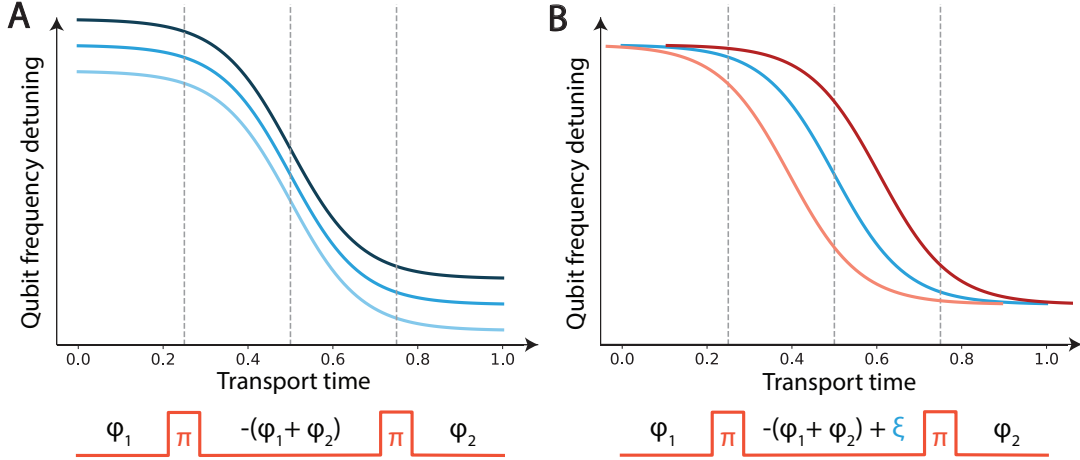


Figure B.8: Sketches of the ways variations in detuning could cause dephasing. **(A)** Vertical variations, coming from a finite temperature, can be echoed out with an even number of CP pulses. **(B)** Horizontal variations, coming from trap pointing instabilities, cannot be echoed out exactly, and contribute to extra dephasing.

time in a Ramsey sequence. Analogously to echoing out the phase with one spin echo in a static case, an even number of spin echo pulses would echo it out in the symmetrically changing case. Importantly, this configuration would echo out the phase variation due to the finite temperature, thus reverting qubit dephasing. If the trap pointing varies in time such that the detuning symmetry axis varies (Fig B.8B), the symmetric echo would not correct for the temperature-induced variations, and the moving atoms would have an extra dephasing channel. The pointing variations are minimized by tracking the cavity position periodically. To move the traps, we use different scanning mirrors (trap A: Cambridge Technology 8310K, trap B: Physik Instrumente S-330.4SL). We have observed differences in coherence properties between the two traps after transport,

which we attribute to the larger fluctuations in trap A.

In order to distribute the pulses symmetrically, we map out the detuning profile during the transport. We probe each of the atoms by starting in the state $|0\rangle$ and applying a detuned π pulse at a variable point during the transport. The population transfer to $|1\rangle$ will depend on the qubit frequency at the time of the π pulse according to the Rabi lineshape. We measure and account for the delay in response for each galvanometer mirror and calibrate their input voltage to symmetrize the ramp with respect to the moving time, as shown in Fig. 2B. Furthermore, the bandwidth of the trap B mirror limits the step response time to $\sim 650 \mu\text{s}$, and we program the ramp of trap A to match. This is the time over which the CP sequence is applied as described in the main text.

We optimize the number of pulses in the CP sequence by preparing an atom in a superposition state at the PCC, moving it away while applying CP, and studying the remaining coherence contrast after a variable number of pulses, as shown in Fig. B.9. The even number of pulses performs better than the odd one, as expected, and we find the optimal number to be four for our system parameters. Higher frequency noise components could be addressed by having faster π pulses (in our system $T_\pi = 20 \mu\text{s}$).

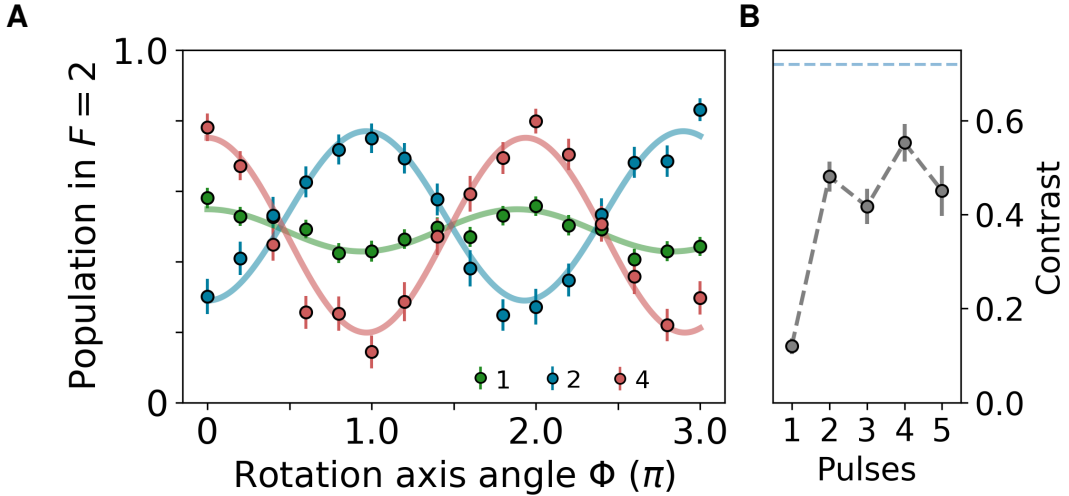


Figure B.9: Optimizing the number of pulses in the CP sequence for a moving atom. **(A)** CP sequences of $N = (1, 2, 4)$ pulses that begin with an atom at the cavity and end with an atom in free space. Decoupling pulses are applied in parallel with the transport. **(B)** Fitted contrast of the CP sequences versus the number of CP pulses.

B.9 Modeling losses upon loading into the cavity near-field

Integration of our platform with a free space Rydberg atom array would require low losses upon loading into the cavity near-field. Here, we theoretically model what those losses depend on, and derive requirements for lossless loading. For the experiments in this work, the survival probability was 0.8 due to polarization gradient cooling (PGC) applied in parallel with the transport. PGC could not be applied if we would want to preserve the state of atoms prepared in free space before loading, so in this section we

investigate the survival probability without cooling during transport.

We numerically study classical trajectories of a single particle in an evolving gaussian potential and observe that an adiabatic increase in the trap frequency introduces heating that ultimately leads to losses, the reverse process of adiabatic cooling (see Section 8.1) [161, 162]. Thermal loss fraction can be determined by averaging trajectories over the phase space weighted by the Boltzmann factor. As there are two relevant axes that transform upon tweezer arrival $(\omega_r, \omega_z) \rightarrow (\omega'_r, \omega'_z)$ [117], we generate the loss fraction as a function of the temperature for the principal axes separately and deduce the survival from the joint probability. Our model assumes separability between the two principal axes, continuity of the trap deformation, and no extra heating caused by the trap rotation. The losses as functions of temperature are generated with parameters extracted from independent trap frequency measurements.

Figure B.10 shows the theoretical predictions for the loading survival probability as a function of the initial atomic temperature and trap depth. Our survival measurements without cooling at different initial temperatures and a trap depth $U_0 = k_B \times 1.6$ mK are marked with yellow circles. The initial temperature is varied by changing the free space PGC parameters, and the temperature values are extracted from drop-recapture measurements. Our observations follow the same trend as the theoretical model.

Our numerical results suggest several ways in which the arrival losses can be remedied. The most immediate one is cooling to the motional ground state, which would also improve coherence properties of atoms by reducing the sensitivity to light shifts.

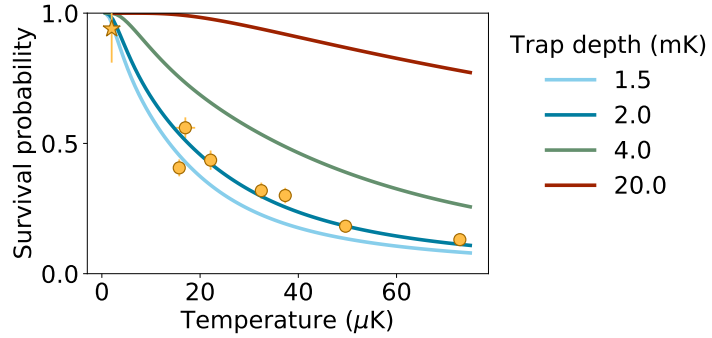


Figure B.10: The effects of temperature and trap depth on the survival probability upon tweezer loading into the cavity near-field. The theoretical curves are generated by averaging over classical trajectories weighted by the Boltzmann factor with no free parameters. Our experimental observations (yellow circles) are taken at a trap depth of 1.6 mK. Previous work on our platform with Raman sideband cooling before transport observed 0.94(6) survival probability (yellow star) [117].

Previous work on our platform utilizing Raman sideband cooling prior to transport (Fig. B.10, yellow star) has achieved a survival probability of 0.94(6) at $T = 2 \mu\text{K}$ and a trap depth $U_0 = k_B \times 2.1 \text{ mK}$ [117]. Without additional cooling, ramping the trap depth up could increase the survival probability, but at the expense of reduced coherence due to higher light shifts. Finally, in our model the losses come from the change in trap frequencies, and applying additional light shift during transport could compensate for that change. This could be achieved with additional trapping beams perpendicular to the current traps that would increase the initial motional frequencies, and that would be ramped down as the traps approached the cavity.

Based on the model presented here, there should be no loss upon departure from the cavity since the trap frequencies decrease. Yet, at a trap depth of $U_0 = k_B \times 1 \text{ mK}$ we

observe a 15% loss. Further investigation is needed to model the loss at low trap depths, but we observe a lossless transport at a trap depth of $U_0 = k_B \times 1.6$ mK, making our system already suitable for protocols that rely on one-way transport.

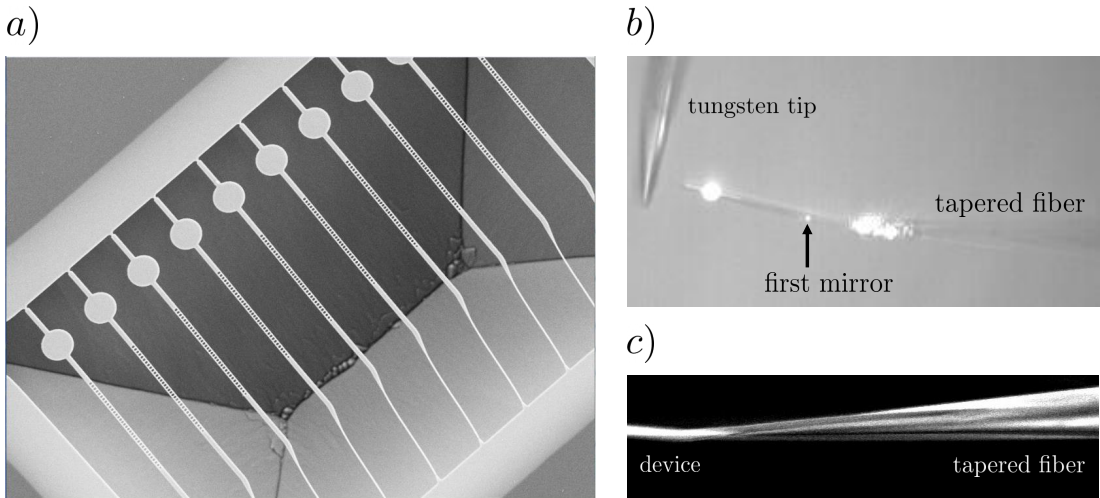
C

Construction of an ultra-high vacuum system for integration with nanophotonics

We outline the procedures for installing the photonic crystal cavity in a ultra-high vacuum (UHV) apparatus presented in Fig. A.1. The procedures have been streamlined for fast switching of cavity devices to accommodate design improvements or replacements in case of device failures. The procedures consist of four major steps: 1. characterizing nanofabricated devices 2. installing a device on a tapered fiber 3. assembling the fiber tip in the vacuum system 4. vacuum pump-down. These steps, detailed below, are conducted in sequence and can be completed within the course of two weeks.

C.1 Device fabrication and characterization

The fabrication process presented in Section A.2.1 primarily consists of electron beam lithography and reactive ion etching, yielding arrays of 500 silicon nitride devices on a silicon substrate divided in sets of tens devices with identical design parameters (Fig. C.1a). The sample then undergoes wet etching in potassium hydroxide (KOH) for the silicon underneath the silicon nitride layer to be removed, leaving the devices suspended on two supporting notches.



The relevant parameters of the cavity devices, namely the resonance frequencies and

the quality factors, can then be extracted from reflection spectra. We taper a fiber (Thorlabs 780 HP) with a flame-pulling method, mount the fiber tip on a nanopositioner (Thorlabs MAX312D), and coupling to a desired device to acquire its reflection spectrum. The methods for achieving the high-efficiency fiber interface is elaborated in [92]. The fabrication imperfections typically yield systematic uncertainties on cavity resonances of $\sim \pm 2$ nm and quality factors ranging between $\sim 50,000 - 500,000$.

Samples that pass the characterization are then taken to an electron beam evaporator for amorphous silicon deposition onto the disk-shaped heater pad region used for thermal tuning of the resonance. The tuning range is limited by the damage threshold of $\sim \pm 2 - 4$ nm, comparable to the fabrication imperfections. To circumvent this, we vary the photonic crystal hole sizes across different sets in the design and typically obtain 10-20 useful devices per sample.

C.2 Installation of a photonic crystal device in a vacuum system

A desired device is broken off at the supporting notches with a tungsten tip controlled by a nanopositioner. Once detached, the device sticks to the tip under the presence of van der Waals forces and can be transferred onto the fiber (Fig. C.1b). Achieving high-efficiency fiber coupling at this stage is a particularly delicate process that remains

the bottleneck for the rest of the installation process. The fiber-waveguide junction is imaged under a scanning electron microscope (SEM) to deposit sticky hydrocarbon junk serving as glue.

The fiber tip is held in the vacuum system by a steel rod assembly (Fig. C.2a). The fiber is threaded through and glued with vacuum compatible epoxy (EPO-TEK H77) to the 23-gauge inner needle, which is glued to the 18-gauge outer needle that fits into a steel mount (Fig. C.2b).

In practice, we pre-assemble the needle mount with a bare fiber tip before attaching the cavity device. This helps minimize unnecessary movements and exposure during gluing for better throughput yield. The long end of the fiber is led to the outside of the vacuum through a fiber feedthrough [148]. Once a cavity is attached and SEM-imaged, we install the needle assembly under a microscope to ensure the correct orientation and position of the cavity of the fiber tip relative to the steel mount.

C.3 Pump-down of the ultra-high vacuum system for atom trapping

The fully-assembled system is depicted in Fig. C.2a. The glass cell provides ample optical access to high-resolution imaging and cooling beams. The entire system is rested on a translational stage, allowing the vacuum preparation to be carried out away from

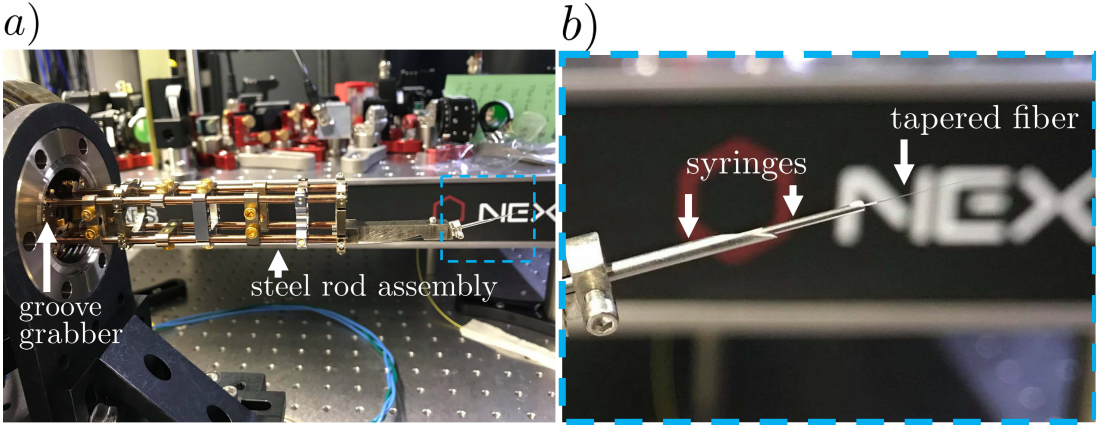


Figure C.2: a) A steel rod assembly attached to groove grabbers holding the needle mount. b) A zoomed-in view of the needle mount with a fiber glued to the 23-gauge inner needle with the tip is 7 mm away from the end of the needle.

the optical setup for minimal readjustments (Fig. C.2b). Fig. C.2c shows the interior of the chamber, as well as the line of sight between the back viewport and the fiber tip.

We follow the standard procedures for reaching UHV [163]. A temporary oven is constructed around the chamber used in vacuum bake-out (Fig. C.2b) with a turbo pump connected to the valve mounted on the top flange. We monitor the pressure and the temperature at various places throughout the process, paying close attention to the temperature gradient at the glass-to-metal transition of the glass cell, which should not exceed a 5 °C difference between glass and metal. The system is left to an average temperature of 105-110 °C for over 24 hours to reach the final ion pump reading of $\sim 10^{-10}$ Torr. In addition, the cavity resonance is monitored and is observed to shift with the temperature. As long as the rubidium dispensers are sufficiently degassed by slowly turning the current through them to 5 A and down to zero, we observe a minimal

resonance shift once the system is cooled down to room temperature.

Once a UHV pressure is reached, we disassemble the oven and transfer the chamber back to the optical setup (Fig. C.2d). The device is then imaged within the field of view of the objectives (Mitutoyo G Plan Apo 50X). No further alignment is required to resume atomic physics experiments described in Sections A.3 and B.2.

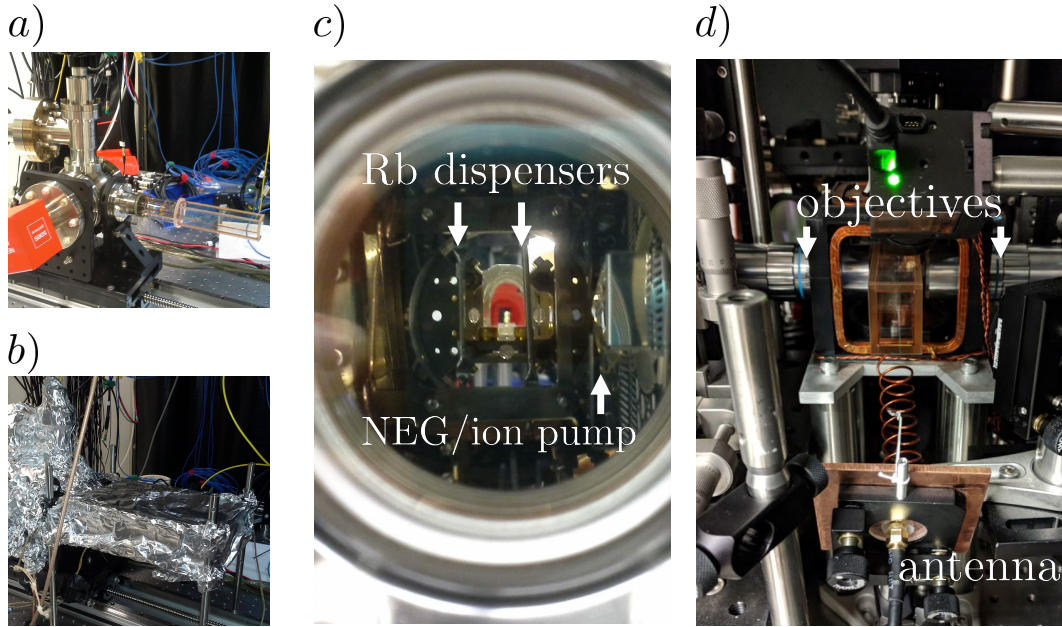


Figure C.3: a) The fully-assembled vacuum system sitting on a translational stage. b) The bake-out process carried out with a temporary oven built away from the optical setup. Layers of aluminum foils and heating tapes are wrapped around a rectangular frame surrounding the glass cell. c) An image of the chamber taken through the back viewport showing a line of sight through the glass cell. d) The vacuum system in normal operations. The glass cell is inserted at the center of the atomic physics apparatus, with two objectives for tweezer generation and alignment relative to the cavity. The bias magnetic fields are generated with the square coils mounted on a 3D-printed cube surrounding the setup. Microwave signals are delivered via a helical antenna.

D

Laser system for individual addressing

D.1 List of laser systems

The experiments described in this thesis require seven laser systems running simultaneously. We briefly describe their functions as follows:

1. **Dipole trap:** 815 nm Ti:sapphire laser (Coherent) for generation of the tweezer light.
2. **Repumper:** 780 nm distributed Bragg reflector (DBR) laser diode (Photodigm PH780DBR) locked and upshifted to produce the repumping frequency resonant with the $5S_{1/2}$, $F = 1 \rightarrow 5P_{1/2}$, $F' = 2$ transition.
3. **Probe laser:** 780 nm DBR laser (D2-100-DBR-780) beat-locked to the repumper at 6.8 GHz and split into cooling beams and cavity probe.
4. **Cavity reference:** 810 nm external-cavity diode laser (ECDL, Toptica DL100) locked to a wavemeter (HighFinesse WS6) and used as a reference for cavity stabilization, the details of which are described in Section [A.2.2](#).

5. **Cavity heater:** 850 nm laser diode (Thorlabs L850P) used for thermal tuning of the cavity resonance (see Section [A.2.2](#)).
6. **Raman laser:** 795 nm ECDL (Toptica DL pro) locked to the wavemeter and used for fast qubit manipulation, complementary with microwave drive.
7. **Individual addressing:** 795 nm DBR laser diode (Photodigm PH795DBR) used in ground state pumping of the individual atoms. The details of this system are elaborated in the following sections.

D.2 Experimental requirements for the individual addressing beams

The ability to control the internal states of the individual atoms is crucial for performing cavity experiments with two or more atoms. While cavity readout is rapid and efficient for detecting one atom and probing its state, obtaining information on multiple atoms with a single readout port is less straightforward.

The lack of individual readout must therefore be supplemented individual control. One approach is to tune the frequency of each atom (Fig. [2.4b](#)) and selectively detect the atom that is on resonance with the probe. In our regime, we achieve good frequency selectivity in the dispersive regime in which the signal strength is sacrificed due to motional averaging.

The approach used in this work is to manipulate the internal atomic states and

selectively bring them in and out of the coupled $F = 2$ manifold. This can be done by taking advantage of the spatial separation between the tweezers and sending resonant light overlapped with the individual trap to perform incoherent pumping into a desired manifold. It is beneficial to filter out the pumping light from the cavity probe detection at 780 nm, hence our choice of wavelength at 795 nm. We implement this method to sequentially detect the presence of each atom in post-selection discussed in Section A.3.

While the entanglement protocol presented in Chapter 3 utilizes only global coherent control and parity measurements, single-qubit manipulation and individual readout of atomic states are required for complete quantum operations in future experiments. We note the distinction between atomic detection and readout, the latter of which poses a more stringent requirement, namely the information about the state must not be erased by the pumping light before a readout pulse. This is achieved by individual coherent rotations of the two-atom states into e.g. $|00\rangle$, which has a distinct dark response in the resonant regime.

The individual rotation can be either achieved by directly driving with focused Raman beams [164], or by combining global e.g. microwave control with individual differential light shifts [165, 166]. The second method can be implemented with a laser frequency tuned between the two hyperfine manifolds. As the frequency separation between the required frequency is several gigahertz from the pumping frequencies, we can satisfy all of the requirements listed above for the individual addressing beams with one laser system and an electro-optic modulator (EOM).

D.3 Generation of laser frequencies

The setup for frequency generation is depicted in Fig. D.1. A laser diode A laser diode (Photodigm PH795DBR) is referenced to a rubidium vapor cell. We place an electro-optic phase modulator (Thorlabs EO-PM-R-20-C1) driven at 20 MHz in the spectroscopy path so as not to modulate the light sent to the experiment and generate the error signal for frequency stabilization by demodulating the response of the photodetector (Thorlabs DET36A2).

The laser frequency is referenced to the $5S_{1/2}$, $F = 2 \rightarrow 5P_{1/2}$, $F' = 2 \times 3$ crossover transition of ^{85}Rb (not the isotope used in this work), conveniently spaced between the $F = \{1, 2\} \rightarrow F' = 1 \times 2$ crossover transitions of ^{87}Rb , away by $\{2.506, 4.329\}$ GHz respectively. These microwave tones, generated from synthesizers (Analog Devices ADF4350), are used to drive another electro-optic phase modulator (EOSpace PM-0S5-10-PFA-PFA-780) to generate resonant pumping light from the corresponding transitions. The shifts are matched with the drive frequency applied to the acousto-optic modulators (AOMs) further down in the path. We split the phase modulator output into two paths, each of which contains an AOM to modulate the amplitude of the individual addressing beam for each tweezer. With the microwave tones switched off, the carrier frequency is suitable for implementing differential light shifts on the qubit states $|F = 1, m_F = 0\rangle$ and $|F = 2, m_F = 0\rangle$ for individual coherent addressing when combined with a global drive.

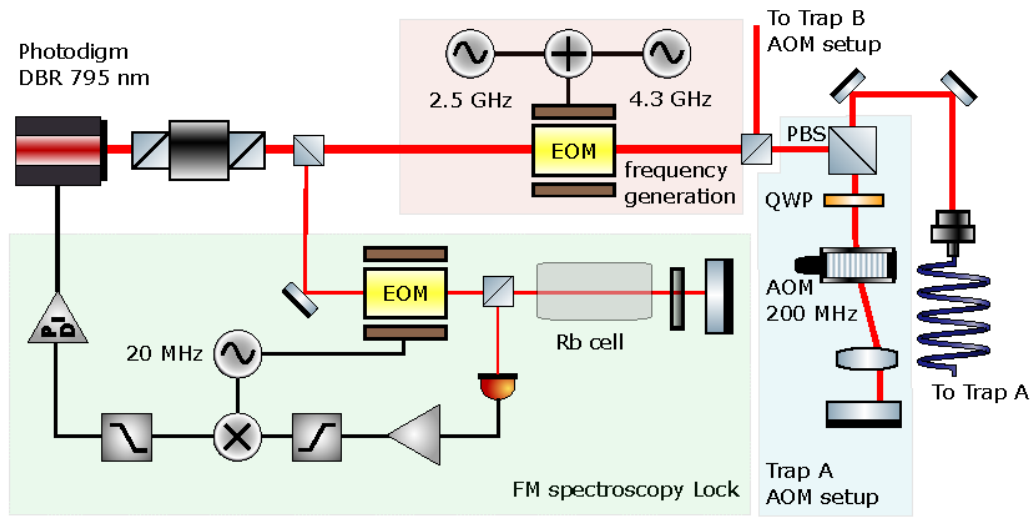


Figure D.1: **Schematic of a laser system for individual addressing.** A DBR laser is locked to the $5S_{1/2}$, $F = 2 \rightarrow 5P_{1/2}$, $F' = 2 \times 3$ crossover transition of ^{85}Rb with error signal derived from FM spectroscopy. The frequencies resonant to the pumping transitions of transitions of ^{87}Rb are generated with shifts from a phase modulator and an AOM in the double-passed configuration. The following abbreviations are used: DBR for distributed Bragg reflector, EOM for electro-optic modulator, AOM for acousto-optic modulator PBS for polarizing beamsplitter, and QWP for quarter-wave plate.

Bibliography

- [1] I. Bloch, J. Dalibard, and W. Zwerger. “Many-body physics with ultracold gases”. *Reviews of modern physics* 80.3 (2008), p. 885 (cited on p. 1).
- [2] F. Arute, K. Arya, R. Babbush, D. Bacon, J. C. Bardin, R. Barends, S. Boixo, M. Broughton, B. B. Buckley, D. A. Buell, B. Burkett, N. Bushnell, Y. Chen, Z. Chen, B. Chiaro, R. Collins, W. Courtney, S. Demura, A. Dunsworth, E. Farhi, A. Fowler, B. Foxen, C. Gidney, M. Giustina, R. Graff, S. Habegger, M. P. Harrigan, A. Ho, S. Hong, T. Huang, W. J. Huggins, L. Ioffe, S. V. Isakov, E. Jeffrey, Z. Jiang, C. Jones, D. Kafri, K. Kechedzhi, J. Kelly, S. Kim, P. V. Klimov, A. Korotkov, F. Kostritsa, D. Landhuis, P. Laptev, M. Lindmark, E. Lucero, O. Martin, J. M. Martinis, J. R. McClean, M. McEwen, A. Megrant, X. Mi, M. Mohseni, W. Mruczkiewicz, J. Mutus, O. Naaman, M. Neeley, C. Neill, H. Neven, M. Y. Niu, T. E. O’Brien, E. Ostby, A. Petukhov, H. Putterman, C. Quintana, P. Roushan, N. C. Rubin, D. Sank, K. J. Satzinger, V. Smelyanskiy, D. Strain, K. J. Sung, M. Szalay, T. Y. Takeshita, A. Vainsencher, T. White, N. Wiebe, Z. J. Yao, P. Yeh, and A. Zalcman. “Hartree-Fock on a superconducting qubit quantum computer”. *Science* 369.6507 (2020), pp. 1084–1089 (cited on pp. 1, 5).
- [3] Y. Nam, J.-S. Chen, N. C. Pisenti, K. Wright, C. Delaney, D. Maslov, K. R. Brown, S. Allen, J. M. Amini, J. Apisdorf, K. M. Beck, A. Blinov, V. Chaplin, M. Chmielewski, C. Collins, S. Debnath, K. M. Hudek, A. M. Ducore, M. Keesan, S. M. Kreikemeier, J. Mizrahi, P. Solomon, M. Williams, J. D. Wong-Campos, D. Moehring, C. Monroe, and J. Kim. “Ground-state energy estimation of the water molecule on a trapped-ion quantum computer”. *npj Quantum Information* 6.1 (2020), p. 33 (cited on p. 1).
- [4] A. D. Ludlow, M. M. Boyd, J. Ye, E. Peik, and P. O. Schmidt. “Optical atomic clocks”. *Reviews of Modern Physics* 87.2 (2015), p. 637 (cited on p. 1).
- [5] H. J. Kimble. “The quantum internet”. *Nature* 453 (2008), 1023 EP - (cited on pp. 1, 2, 24).

- [6] D. Awschalom, K. K. Berggren, H. Bernien, S. Bhave, L. D. Carr, P. Davids, S. E. Economou, D. Englund, A. Faraon, M. Fejer, S. Guha, M. V. Gustafsson, E. Hu, L. Jiang, J. Kim, B. Korzh, P. Kumar, P. G. Kwiat, M. Lončar, M. D. Lukin, D. A. B. Miller, C. Monroe, S. W. Nam, P. Narang, J. S. Orcutt, M. G. Raymer, A. H. Safavi-Naeini, M. Spiropulu, K. Srinivasan, S. Sun, J. Vučković, E. Waks, R. Walsworth, A. M. Weiner, and Z. Zhang. *Development of Quantum InterConnects for Next-Generation Information Technologies*. 2020 (cited on p. 1).
- [7] C. Monroe and J. Kim. “Scaling the ion trap quantum processor”. *Science* 339.6124 (2013), pp. 1164–1169 (cited on p. 1).
- [8] M. K. Bhaskar, R. Riedinger, B. Machielse, D. S. Levonian, C. T. Nguyen, E. N. Knall, H. Park, D. Englund, M. Lončar, D. D. Sukachev, and M. D. Lukin. “Experimental demonstration of memory-enhanced quantum communication”. *Nature* 580.7801 (2020), pp. 60–64 (cited on pp. 2, 4).
- [9] J. Yin, Y.-H. Li, S.-K. Liao, M. Yang, Y. Cao, L. Zhang, J.-G. Ren, W.-Q. Cai, W.-Y. Liu, S.-L. Li, R. Shu, Y.-M. Huang, L. Deng, L. Li, Q. Zhang, N.-L. Liu, Y.-A. Chen, C.-Y. Lu, X.-B. Wang, F. Xu, J.-Y. Wang, C.-Z. Peng, A. K. Ekert, and J.-W. Pan. “Entanglement-based secure quantum cryptography over 1,120 kilometres”. *Nature* 582.7813 (2020), pp. 501–505 (cited on p. 2).
- [10] Y.-A. Chen, Q. Zhang, T.-Y. Chen, W.-Q. Cai, S.-K. Liao, J. Zhang, K. Chen, J. Yin, J.-G. Ren, Z. Chen, S.-L. Han, Q. Yu, K. Liang, F. Zhou, X. Yuan, M.-S. Zhao, T.-Y. Wang, X. Jiang, L. Zhang, W.-Y. Liu, Y. Li, Q. Shen, Y. Cao, C.-Y. Lu, R. Shu, J.-Y. Wang, L. Li, N.-L. Liu, F. Xu, X.-B. Wang, C.-Z. Peng, and J.-W. Pan. “An integrated space-to-ground quantum communication network over 4,600 kilometres”. *Nature* 589.7841 (2021), pp. 214–219 (cited on p. 2).
- [11] J. I. Cirac, A. K. Ekert, S. F. Huelga, and C. Macchiavello. “Distributed quantum computation over noisy channels”. *Phys. Rev. A* 59 (6 1999), pp. 4249–4254 (cited on p. 2).
- [12] N. H. Nickerson, Y. Li, and S. C. Benjamin. “Topological quantum computing with a very noisy network and local error rates approaching one

percent”. *Nature Communications* 4 (2013), 1756 EP - (cited on pp. 2, 25, 28).

- [13] N. Leung, Y. Lu, S. Chakram, R. K. Naik, N. Earnest, R. Ma, K. Jacobs, A. N. Cleland, and D. I. Schuster. “Deterministic bidirectional communication and remote entanglement generation between superconducting qubits”. *npj Quantum Information* 5.1 (2019), p. 18 (cited on p. 2).
- [14] Y. Zhong, H.-S. Chang, A. Bienfait, É. Dumur, M.-H. Chou, C. R. Conner, J. Grebel, R. G. Povey, H. Yan, D. I. Schuster, and A. N. Cleland. *Deterministic multi-qubit entanglement in a quantum network*. 2020 (cited on p. 2).
- [15] P. Kómár, E. M. Kessler, M. Bishof, L. Jiang, A. S. Sørensen, J. Ye, and M. D. Lukin. “A quantum network of clocks”. *Nature Physics* 10 (2014), 582 EP - (cited on pp. 2, 24).
- [16] E. T. Khabiboulline, J. Borregaard, K. De Greve, and M. D. Lukin. “Quantum-assisted telescope arrays”. *Phys. Rev. A* 100 (2 2019), p. 022316 (cited on pp. 2, 24).
- [17] D. Gottesman, T. Jennewein, and S. Croke. “Longer-Baseline Telescopes Using Quantum Repeaters”. *Phys. Rev. Lett.* 109 (7 2012), p. 070503 (cited on p. 2).
- [18] A. Reiserer and G. Rempe. “Cavity-based quantum networks with single atoms and optical photons”. *Rev. Mod. Phys.* 87 (4 2015), pp. 1379–1418 (cited on pp. 2, 12, 28).
- [19] L. .-M. Duan, M. D. Lukin, J. I. Cirac, and P. Zoller. “Long-distance quantum communication with atomic ensembles and linear optics”. *Nature* 414.6862 (2001), pp. 413–418 (cited on pp. 3, 12).
- [20] H.-J. Briegel, W. Dür, J. I. Cirac, and P. Zoller. “Quantum Repeaters: The Role of Imperfect Local Operations in Quantum Communication”. *Phys. Rev. Lett.* 81 (26 1998), pp. 5932–5935 (cited on pp. 3, 12, 43).
- [21] D. E. Chang, V. Vuletić, and M. D. Lukin. “Quantum nonlinear optics—photon by photon”. *Nature Photonics* 8.9 (2014), p. 685 (cited on p. 3).

- [22] R. J. Thompson, G. Rempe, and H. J. Kimble. “Observation of normal-mode splitting for an atom in an optical cavity”. *Phys. Rev. Lett.* 68 (8 1992), pp. 1132–1135 (cited on p. 4).
- [23] Y. Colombe, T. Steinmetz, G. Dubois, F. Linke, D. Hunger, and J. Reichel. “Strong atom–field coupling for Bose–Einstein condensates in an optical cavity on a chip”. *Nature* 450 (2007), pp. 272–276 (cited on p. 4).
- [24] S. Welte, B. Hacker, S. Daiss, S. Ritter, and G. Rempe. “Photon-Mediated Quantum Gate between Two Neutral Atoms in an Optical Cavity”. *Phys. Rev. X* 8 (1 2018), p. 011018 (cited on pp. 4, 24).
- [25] S. Daiss, S. Langenfeld, S. Welte, E. Distante, P. Thomas, L. Hartung, O. Morin, and G. Rempe. “A quantum-logic gate between distant quantum-network modules”. *Science* 371.6529 (2021), pp. 614–617 (cited on p. 4).
- [26] P. Siyushev, M. H. Metsch, A. Ijaz, J. M. Binder, M. K. Bhaskar, D. D. Sukachev, A. Sipahigil, R. E. Evans, C. T. Nguyen, M. D. Lukin, P. R. Hemmer, Y. N. Palyanov, I. N. Kupriyanov, Y. M. Borzdov, L. J. Rogers, and F. Jelezko. “Optical and microwave control of germanium-vacancy center spins in diamond”. *Phys. Rev. B* 96 (8 2017), p. 081201 (cited on p. 4).
- [27] L. J. Rogers, K. D. Jahnke, M. H. Metsch, A. Sipahigil, J. M. Binder, T. Teraji, H. Sumiya, J. Isoya, M. D. Lukin, P. Hemmer, and F. Jelezko. “All-Optical Initialization, Readout, and Coherent Preparation of Single Silicon-Vacancy Spins in Diamond”. *Phys. Rev. Lett.* 113 (26 2014), p. 263602 (cited on p. 4).
- [28] A. E. Rugar, S. Aghaeimeibodi, D. Riedel, C. Dory, H. Lu, P. J. McQuade, Z.-X. Shen, N. A. Melosh, and J. Vučković. *A Quantum Photonic Interface for Tin-Vacancy Centers in Diamond*. 2021 (cited on p. 4).
- [29] D. D. Sukachev, A. Sipahigil, C. T. Nguyen, M. K. Bhaskar, R. E. Evans, F. Jelezko, and M. D. Lukin. “Silicon-Vacancy Spin Qubit in Diamond: A Quantum Memory Exceeding 10 ms with Single-Shot State Readout” (2017) (cited on p. 4).
- [30] C. T. Nguyen, D. D. Sukachev, M. K. Bhaskar, B. Machielse, D. S. Levonian, E. N. Knall, P. Stroganov, C. Chia, M. J. Burek, R. Riedinger, H.

- Park, M. Lončar, and M. D. Lukin. “An integrated nanophotonic quantum register based on silicon-vacancy spins in diamond”. *Physical Review B* 100.16 (2019), p. 165428 (cited on p. 4).
- [31] C. E. Bradley, J. Randall, M. H. Abobeih, R. C. Berrevoets, M. J. Degen, M. A. Bakker, M. Markham, D. J. Twitchen, and T. H. Taminiau. “A Ten-Qubit Solid-State Spin Register with Quantum Memory up to One Minute”. *Phys. Rev. X* 9 (3 2019), p. 031045 (cited on p. 4).
- [32] M. Ruf, M. J. Weaver, S. B. van Dam, and R. Hanson. *Resonant Excitation and Purcell Enhancement of Coherent Nitrogen-Vacancy Centers Coupled to a Fabry-Pérot Micro-Cavity*. 2020 (cited on p. 4).
- [33] S. B. van Dam, M. Ruf, and R. Hanson. “Optimal design of diamond-air microcavities for quantum networks using an analytical approach”. *New Journal of Physics* 20.11 (2018), p. 115004 (cited on p. 4).
- [34] S. Bogdanovic. “Diamond-based Fabry-Perot microcavities for quantum networks”. PhD thesis. Delft University of Technology, 2017 (cited on p. 4).
- [35] E. Janitz, M. Ruf, M. Dimock, A. Bourassa, J. Sankey, and L. Childress. “Fabry-Perot microcavity for diamond-based photonics”. *Physical Review A* 92.4 (2015), p. 043844 (cited on p. 4).
- [36] A. Sipahigil, R. E. Evans, D. D. Sukachev, M. J. Burek, J. Borregaard, M. K. Bhaskar, C. T. Nguyen, J. L. Pacheco, H. A. Atikian, C. Meuwly, R. M. Camacho, F. Jelezko, E. Bielejec, H. Park, M. Lončar, and M. D. Lukin. “An integrated diamond nanophotonics platform for quantum-optical networks”. *Science* 354.6314 (2016), pp. 847–850 (cited on p. 4).
- [37] C. T. Nguyen, D. D. Sukachev, M. K. Bhaskar, B. Machielse, D. S. Levonian, E. N. Knall, P. Stroganov, R. Riedinger, H. Park, M. Lončar, and M. D. Lukin. “Quantum Network Nodes Based on Diamond Qubits with an Efficient Nanophotonic Interface”. *Physical Review Letters* 123 (2019) (cited on p. 4).
- [38] N. Kalb, A. A. Reiserer, P. C. Humphreys, J. J. W. Bakermans, S. J. Kamerling, N. H. Nickerson, S. C. Benjamin, D. J. Twitchen, M. Markham,

and R. Hanson. “Entanglement distillation between solid-state quantum network nodes”. *Science* 356.6341 (2017), pp. 928–932 (cited on p. 4).

- [39] M. Pompili, S. L. N. Hermans, S. Baier, H. K. C. Beukers, P. C. Humphreys, R. N. Schouten, R. F. L. Vermeulen, M. J. Tiggelman, L. dos Santos Martins, B. Dirkse, S. Wehner, and R. Hanson. *Realization of a multi-node quantum network of remote solid-state qubits*. 2021 (cited on p. 4).
- [40] W. Redjem, A. Durand, T. Herzog, A. Benali, S. Pezzagna, J. Meijer, A. Yu Kuznetsov, H. S. Nguyen, S. Cueff, J.-m. Gérard, I. Robert-Philip, B. Gil, D. Caliste, P. Pochet, M. Abbarchi, V. Jacques, A. Dréau, and G. Cassabois. “Single artificial atoms in silicon emitting at telecom wavelengths”. *Nature Electronics* (2020) (cited on p. 4).
- [41] M. Raha, S. Chen, C. M. Phenicie, S. Ourari, A. M. Dibos, and J. D. Thompson. “Optical quantum nondemolition measurement of a single rare earth ion qubit” () (cited on pp. 4, 5).
- [42] M. Zhong, M. P. Hedges, R. L. Ahlefeldt, J. G. Bartholomew, S. E. Beavan, S. M. Wittig, J. J. Longdell, and M. J. Sellars. “Optically addressable nuclear spins in a solid with a six-hour coherence time” (2014) (cited on p. 4).
- [43] T. Zhong, J. M. Kindem, E. Miyazono, and A. Faraon. “Nanophotonic coherent light–matter interfaces based on rare-earth-doped crystals”. *Nature communications* 6 (2015), p. 8206 (cited on pp. 5, 7).
- [44] L. Weiss, A. Gritsch, B. Merkel, and A. Reiserer. “Erbium dopants in silicon nanophotonic waveguides” (2020), pp. 1–7 (cited on p. 5).
- [45] S. Chen, M. Raha, C. M. Phenicie, S. Ourari, and J. D. Thompson. *Parallel single-shot measurement and coherent control of solid-state spins below the diffraction limit*. Tech. rep. 2020 (cited on p. 5).
- [46] J. P. Covey, A. Sipahigil, S. Szoke, N. Sinclair, M. Endres, and O. Painter. “Telecom-Band Quantum Optics with Ytterbium Atoms and Silicon Nanophotonics”. *Phys. Rev. Applied* 11 (3 2019), p. 034044 (cited on pp. 5, 44).

- [47] S. G. Menon, K. Singh, J. Borregaard, and H. Bernien. “Nanophotonic quantum network node with neutral atoms and an integrated telecom interface”. *New Journal of Physics* 22.7 (2020), p. 073033 (cited on pp. 5, 44).
- [48] F. Arute, K. Arya, R. Babbush, D. Bacon, J. C. Bardin, R. Barends, R. Biswas, S. Boixo, F. G. S. L. Brando, D. A. Buell, B. Burkett, Y. Chen, Z. Chen, B. Chiaro, R. Collins, W. Courtney, A. Dunsworth, E. Farhi, B. Foxen, A. Fowler, C. Gidney, M. Giustina, R. Graff, K. Guerin, S. Habegger, M. P. Harrigan, M. J. Hartmann, A. Ho, M. Hoffmann, T. Huang, T. S. Humble, S. V. Isakov, E. Jeffrey, Z. Jiang, D. Kafri, K. Kechedzhi, J. Kelly, P. V. Klimov, S. Knysh, A. Korotkov, F. Kostritsa, D. Landhuis, M. Lindmark, E. Lucero, D. Lyakh, S. Mandrà, J. R. McClean, M. McEwen, A. Megrant, X. Mi, K. Michelsen, M. Mohseni, J. Mutus, O. Naaman, M. Neeley, C. Neill, M. Y. Niu, E. Ostby, A. Petukhov, J. C. Platt, C. Quintana, E. G. Rieffel, P. Roushan, N. C. Rubin, D. Sank, K. J. Satzinger, V. Smelyanskiy, K. J. Sung, M. D. Trevithick, A. Vainsencher, B. Villalonga, T. White, Z. J. Yao, P. Yeh, A. Zalcman, H. Neven, and J. M. Martinis. “Quantum supremacy using a programmable superconducting processor”. *Nature* 574.7779 (2019), pp. 505–510 (cited on p. 5).
- [49] M. Mirhosseini, A. Sipahigil, M. Kalaei, and O. Painter. *Quantum transduction of optical photons from a superconducting qubit*. Tech. rep. 2020 (cited on p. 5).
- [50] M. Reagor, W. Pfaff, C. Axline, R. W. Heeres, N. Ofek, K. Sliwa, E. Holland, C. Wang, J. Blumoff, K. Chou, M. J. Hatridge, L. Frunzio, M. H. Devoret, L. Jiang, and R. J. Schoelkopf. “Quantum memory with millisecond coherence in circuit QED”. *Phys. Rev. B* 94 (1 2016), p. 014506 (cited on p. 5).
- [51] A. P. M. Place, L. V. H. Rodgers, P. Mundada, B. M. Smitham, M. Fitzpatrick, Z. Leng, A. Premkumar, J. Bryon, S. Sussman, G. Cheng, T. Madhavan, H. K. Babla, B. Jaeck, A. Gyenis, N. Yao, R. J. Cava, N. P. de Leon, and A. A. Houck. *New material platform for superconducting transmon qubits with coherence times exceeding 0.3 milliseconds*. 2020 (cited on p. 5).

- [52] A. Somoroff, Q. Ficheux, R. A. Mencia, H. Xiong, R. V. Kuzmin, and V. E. Manucharyan. *Millisecond coherence in a superconducting qubit*. 2021 (cited on p. 5).
- [53] H. Kim, W. Lee, H.-g. Lee, H. Jo, Y. Song, and J. Ahn. “In situ single-atom array synthesis using dynamic holographic optical tweezers”. *Nature Communications* 7 (2016), 13317 EP - (cited on pp. 6, 12, 24).
- [54] M. Endres, H. Bernien, A. Keesling, H. Levine, E. R. Anschuetz, A. Krajenbrink, C. Senko, V. Vuletic, M. Greiner, and M. D. Lukin. “Atom-by-atom assembly of defect-free one-dimensional cold atom arrays”. *Science* 354.6315 (2016), pp. 1024–1027 (cited on pp. 6, 12, 24).
- [55] D. Barredo, S. de Léséleuc, V. Lienhard, T. Lahaye, and A. Browaeys. “An atom-by-atom assembler of defect-free arbitrary two-dimensional atomic arrays”. *Science* 354.6315 (2016), pp. 1021–1023 (cited on pp. 6, 12, 24).
- [56] D. Barredo, V. Lienhard, S. de Léséleuc, T. Lahaye, and A. Browaeys. “Synthetic three-dimensional atomic structures assembled atom by atom”. *Nature* 561.7721 (2018), pp. 79–82 (cited on pp. 6, 12, 24).
- [57] A. Kumar, T.-Y. Wu, F. Giraldo, and D. S. Weiss. “Sorting ultracold atoms in a three-dimensional optical lattice in a realization of Maxwell’s demon”. *Nature* 561.7721 (2018), pp. 83–87 (cited on pp. 6, 12, 24).
- [58] D. Ohl de Mello, D. Schäffner, J. Werkmann, T. Preuschoff, L. Kohfahl, M. Schlosser, and G. Birkl. “Defect-Free Assembly of 2D Clusters of More Than 100 Single-Atom Quantum Systems”. *Phys. Rev. Lett.* 122 (20 2019), p. 203601 (cited on pp. 6, 12, 24).
- [59] A. M. Kaufman, B. J. Lester, and C. A. Regal. “Cooling a Single Atom in an Optical Tweezer to Its Quantum Ground State”. *Phys. Rev. X* 2 (4 2012), p. 041014 (cited on pp. 6, 24, 44, 45).
- [60] J. D. Thompson, T. G. Tiecke, A. S. Zibrov, V. Vuletić, and M. D. Lukin. “Coherence and Raman Sideband Cooling of a Single Atom in an Optical Tweezer”. *Phys. Rev. Lett.* 110 (13 2013), p. 133001 (cited on pp. 6, 24, 32, 44, 45, 87).

- [61] H. Bernien, S. Schwartz, A. Keesling, H. Levine, A. Omran, H. Pichler, S. Choi, A. S. Zibrov, M. Endres, M. Greiner, et al. “Probing many-body dynamics on a 51-atom quantum simulator”. *Nature* 551.7682 (2017), p. 579 (cited on p. 6).
- [62] S. de Léséleuc, V. Lienhard, P. Scholl, D. Barredo, S. Weber, N. Lang, H. P. Büchler, T. Lahaye, and A. Browaeys. “Observation of a symmetry-protected topological phase of interacting bosons with Rydberg atoms”. *Science* 365.6455 (2019), pp. 775–780 (cited on p. 6).
- [63] S. Ebadi, T. T. Wang, H. Levine, A. Keesling, G. Semeghini, A. Omran, D. Bluvstein, R. Samajdar, H. Pichler, W. W. Ho, S. Choi, S. Sachdev, M. Greiner, V. Vuletic, and M. D. Lukin. *Quantum Phases of Matter on a 256-Atom Programmable Quantum Simulator*. 2020 (cited on pp. 6, 45).
- [64] I. S. Madjarov, A. Cooper, A. L. Shaw, J. P. Covey, V. Schkolnik, T. H. Yoon, J. R. Williams, and M. Endres. “An Atomic-Array Optical Clock with Single-Atom Readout”. *Phys. Rev. X* 9 (4 2019), p. 041052 (cited on pp. 6, 44).
- [65] M. A. Norcia, A. W. Young, W. J. Eckner, E. Oelker, J. Ye, and A. M. Kaufman. “Seconds-scale coherence on an optical clock transition in a tweezer array”. *Science* 366.6461 (2019), pp. 93–97 (cited on pp. 6, 44).
- [66] H. Levine, A. Keesling, A. Omran, H. Bernien, S. Schwartz, A. S. Zibrov, M. Endres, M. Greiner, V. Vuletić, and M. D. Lukin. “High-Fidelity Control and Entanglement of Rydberg-Atom Qubits”. *Phys. Rev. Lett.* 121 (12 2018), p. 123603 (cited on p. 6).
- [67] H. Levine, A. Keesling, G. Semeghini, A. Omran, T. T. Wang, S. Ebadi, H. Bernien, M. Greiner, V. Vuletić, H. Pichler, and M. D. Lukin. “Parallel Implementation of High-Fidelity Multiqubit Gates with Neutral Atoms”. *Phys. Rev. Lett.* 123 (17 2019), p. 170503 (cited on p. 6).
- [68] I. S. Madjarov, J. P. Covey, A. L. Shaw, J. Choi, A. Kale, A. Cooper, H. Pichler, V. Schkolnik, J. R. Williams, and M. Endres. “High-fidelity entanglement and detection of alkaline-earth Rydberg atoms”. *Nature Physics* 16.8 (2020), pp. 857–861 (cited on p. 6).

- [69] P. Lodahl, S. Mahmoodian, and S. Stobbe. “Interfacing single photons and single quantum dots with photonic nanostructures”. *Rev. Mod. Phys.* 87 (2 2015), pp. 347–400 (cited on pp. 7, 12).
- [70] K. P. Nayak, P. N. Melentiev, M. Morinaga, F. L. Kien, V. I. Balykin, and K. Hakuta. “Optical nanofiber as an efficient tool for manipulating and probing atomic fluorescence”. *Opt. Express* 15.9 (2007), pp. 5431–5438 (cited on p. 7).
- [71] E. Vetsch, D. Reitz, G. Sagué, R. Schmidt, S. T. Dawkins, and A. Rauschenbeutel. “Optical Interface Created by Laser-Cooled Atoms Trapped in the Evanescent Field Surrounding an Optical Nanofiber”. *Phys. Rev. Lett.* 104 (20 2010), p. 203603 (cited on pp. 7, 12).
- [72] A. Goban, C.-L. Hung, S.-P. Yu, J. D. Hood, J. A. Muniz, J. H. Lee, M. J. Martin, A. C. McClung, K. S. Choi, D. E. Chang, O. Painter, and H. J. Kimble. “Atom–light interactions in photonic crystals”. *Nature Communications* 5.1 (2014), p. 3808 (cited on p. 7).
- [73] M. E. Kim, T.-H. Chang, B. M. Fields, C.-A. Chen, and C.-L. Hung. “Trapping single atoms on a nanophotonic circuit with configurable tweezer lattices”. *Nature Communications* 10.1 (2019), p. 1647 (cited on pp. 7, 12, 24, 44, 70).
- [74] D. E. Chang, J. S. Douglas, A. González-Tudela, C.-L. Hung, and H. J. Kimble. “Colloquium: Quantum matter built from nanoscopic lattices of atoms and photons”. *Rev. Mod. Phys.* 90 (3 2018), p. 031002 (cited on pp. 8, 12, 46).
- [75] J. S. Douglas, H. Habibian, C. -L. Hung, A. V. Gorshkov, H. J. Kimble, and D. E. Chang. “Quantum many-body models with cold atoms coupled to photonic crystals”. *Nature Photonics* 9 (2015), 326 EP - (cited on pp. 8, 12, 46).
- [76] J. D. Thompson, T. G. Tiecke, N. P. de Leon, J. Feist, A. V. Akimov, M. Gullans, A. S. Zibrov, V. Vuletić, and M. D. Lukin. “Coupling a Single Trapped Atom to a Nanoscale Optical Cavity”. *Science* 340.6137 (2013), pp. 1202–1205 (cited on pp. 8, 12, 13, 17, 43, 45, 60, 61, 63).

- [77] T. G. Tiecke, J. D. Thompson, N. P. de Leon, L. R. Liu, V. Vuletić, and M. D. Lukin. “Nanophotonic quantum phase switch with a single atom”. *Nature* 508 (2014), 241 EP - (cited on pp. 8, 28, 30, 40, 42, 46).
- [78] D. P. DiVincenzo. “The Physical Implementation of Quantum Computation”. *Fortschritte der Physik* 48.9-11 (2000), pp. 771–783 (cited on p. 12).
- [79] P. Lodahl, A. Floris van Driel, I. S. Nikolaev, A. Irman, K. Overgaag, D. Vanmaekelbergh, and W. L. Vos. “Controlling the dynamics of spontaneous emission from quantum dots by photonic crystals”. *Nature* 430.7000 (2004), pp. 654–657 (cited on p. 12).
- [80] D. Englund, A. Majumdar, A. Faraon, M. Toishi, N. Stoltz, P. Petroff, and J. Vu čović. “Resonant Excitation of a Quantum Dot Strongly Coupled to a Photonic Crystal Nanocavity”. *Phys. Rev. Lett.* 104 (7 2010), p. 073904 (cited on p. 12).
- [81] A. Sipahigil, R. E. Evans, D. D. Sukachev, M. J. Burek, J. Borregaard, M. K. Bhaskar, C. T. Nguyen, J. L. Pacheco, H. A. Atikian, C. Meuwly, R. M. Camacho, F. Jelezko, E. Bielejec, H. Park, M. Lončar, and M. D. Lukin. “An integrated diamond nanophotonics platform for quantum-optical networks”. *Science* 354.6314 (2016), pp. 847–850 (cited on p. 12).
- [82] E. Miyazono, T. Zhong, I. Craiciu, J. M. Kindem, and A. Faraon. “Coupling of erbium dopants to yttrium orthosilicate photonic crystal cavities for on-chip optical quantum memories”. *Applied Physics Letters* 108.1 (2016), p. 11111 (cited on p. 12).
- [83] A. M. Dibos, M. Raha, C. M. Phenicie, and J. D. Thompson. “Atomic Source of Single Photons in the Telecom Band”. *Phys. Rev. Lett.* 120 (24 2018), p. 243601 (cited on p. 12).
- [84] A. González-Tudela, C. .-L. Hung, D. E. Chang, J. I. Cirac, and H. J. Kimble. “Subwavelength vacuum lattices and atom–atom interactions in two-dimensional photonic crystals”. *Nature Photonics* 9 (2015), 320 EP - (cited on p. 12).

- [85] L.-M. Duan and H. J. Kimble. “Scalable Photonic Quantum Computation through Cavity-Assisted Interactions”. *Phys. Rev. Lett.* 92 (12 2004), p. 127902 (cited on pp. 12, 40).
- [86] L.-M. Duan and H. J. Kimble. “Efficient Engineering of Multiatom Entanglement through Single-Photon Detections”. *Phys. Rev. Lett.* 90 (25 2003), p. 253601 (cited on p. 12).
- [87] A. Goban, C.-L. Hung, J. D. Hood, S.-P. Yu, J. A. Muniz, O. Painter, and H. J. Kimble. “Superradiance for Atoms Trapped along a Photonic Crystal Waveguide”. *Phys. Rev. Lett.* 115 (6 2015), p. 063601 (cited on pp. 12, 21, 23, 70).
- [88] M. Antezza, L. P. Pitaevskii, and S. Stringari. “Effect of the Casimir-Polder force on the collective oscillations of a trapped Bose-Einstein condensate”. *Phys. Rev. A* 70 (5 2004), p. 053619 (cited on p. 12).
- [89] J. M. Obrecht, R. J. Wild, and E. A. Cornell. “Measuring electric fields from surface contaminants with neutral atoms”. *Phys. Rev. A* 75 (6 2007), p. 062903 (cited on p. 12).
- [90] J. Majer, J. M. Chow, J. M. Gambetta, J. Koch, B. R. Johnson, J. A. Schreier, L. Frunzio, D. I. Schuster, A. A. Houck, A. Wallraff, A. Blais, M. H. Devoret, S. M. Girvin, and R. J. Schoelkopf. “Coupling superconducting qubits via a cavity bus”. *Nature* 449 (2007), 443 EP - (cited on p. 13).
- [91] R. E. Evans, M. K. Bhaskar, D. D. Sukachev, C. T. Nguyen, A. Sipahigil, M. J. Burek, B. Machielse, G. H. Zhang, A. S. Zibrov, E. Bielejec, H. Park, M. Lončar, and M. D. Lukin. “Photon-mediated interactions between quantum emitters in a diamond nanocavity”. *Science* 362.6415 (2018), pp. 662–665 (cited on p. 13).
- [92] T. G. Tiecke, K. P. Nayak, J. D. Thompson, T. Peyronel, N. P. de Leon, V. Vuletić, and M. D. Lukin. “Efficient fiber-optical interface for nanophotonic devices”. *Optica* 2.2 (2015), pp. 70–75 (cited on pp. 13, 49, 102).

- [93] J. A. Mlynek, A. A. Abdumalikov, C. Eichler, and A. Wallraff. “Observation of Dicke superradiance for two artificial atoms in a cavity with high decay rate”. *Nature Communications* 5 (2014), 5186 EP - (cited on p. 21).
- [94] J. I. Cirac, P. Zoller, H. J. Kimble, and H. Mabuchi. “Quantum State Transfer and Entanglement Distribution among Distant Nodes in a Quantum Network”. *Phys. Rev. Lett.* 78 (16 1997), pp. 3221–3224 (cited on p. 24).
- [95] L.-M. Duan and H. J. Kimble. “Scalable Photonic Quantum Computation through Cavity-Assisted Interactions”. *Phys. Rev. Lett.* 92 (12 2004), p. 127902 (cited on p. 24).
- [96] S. Welte, B. Hacker, S. Daiss, S. Ritter, and G. Rempe. “Cavity Carving of Atomic Bell States”. *Phys. Rev. Lett.* 118 (21 2017), p. 210503 (cited on pp. 24, 35, 38, 76).
- [97] C.-L. Hung, S. M. Meenehan, D. E. Chang, O. Painter, and H. J. Kimble. “Trapped atoms in one-dimensional photonic crystals”. *New Journal of Physics* 15.8 (2013), p. 083026 (cited on pp. 24, 43).
- [98] X. Ji, F. A. S. Barbosa, S. P. Roberts, A. Dutt, J. Cardenas, Y. Okawachi, A. Bryant, A. L. Gaeta, and M. Lipson. “Ultra-low-loss on-chip resonators with sub-milliwatt parametric oscillation threshold”. *Optica* 4.6 (2017), pp. 619–624 (cited on pp. 24, 43).
- [99] Y. Meng, A. Dareau, P. Schneeweiss, and A. Rauschenbeutel. “Near-Ground-State Cooling of Atoms Optically Trapped 300 nm Away from a Hot Surface”. *Phys. Rev. X* 8 (3 2018), p. 031054 (cited on pp. 24, 43).
- [100] J. Borregaard, P. Kómár, E. M. Kessler, M. D. Lukin, and A. S. Sørensen. “Long-distance entanglement distribution using individual atoms in optical cavities”. *Phys. Rev. A* 92 (1 2015), p. 012307 (cited on p. 25).
- [101] M. Kjaergaard, M. E. Schwartz, J. Braumüller, P. Krantz, J. I. Wang, S. Gustavsson, and W. D. Oliver. “Superconducting Qubits: Current State of Play”. *Annual Review of Condensed Matter Physics* 11 (2020), pp. 369–395 (cited on p. 28).

- [102] C. D. Bruzewicz, J. Chiaverini, R. McConnell, and J. M. Sage. “Trapped-ion quantum computing: Progress and challenges”. *Applied Physics Reviews* 6.2 (2019), p. 21314 (cited on p. 28).
- [103] A. Chatterjee, P. Stevenson, S. De Franceschi, A. Morello, N. P. de Leon, and F. Kuemmeth. “Semiconductor qubits in practice”. *Nature Reviews Physics* (2021) (cited on p. 28).
- [104] M. Saffman, T. G. Walker, and K. Mølmer. “Quantum information with Rydberg atoms”. *Rev. Mod. Phys.* 82 (3 2010), pp. 2313–2363 (cited on p. 28).
- [105] C. Monroe, R. Raussendorf, A. Ruthven, K. R. Brown, P. Maunz, L.-M. Duan, and J. Kim. “Large-scale modular quantum-computer architecture with atomic memory and photonic interconnects”. *Phys. Rev. A* 89 (2 2014), p. 022317 (cited on p. 28).
- [106] H. Bernien, S. Schwartz, A. Keesling, H. Levine, A. Omran, H. Pichler, S. Choi, A. S. Zibrov, M. Endres, M. Greiner, V. Vuletic, and M. D. Lukin. “Probing many-body dynamics on a 51-atom quantum simulator”. *Nature* 551 (2017), pp. 579–584 (cited on p. 28).
- [107] S. de Léséleuc, V. Lienhard, P. Scholl, D. Barredo, S. Weber, N. Lang, H. P. Büchler, T. Lahaye, and A. Browaeys. “Observation of a symmetry-protected topological phase of interacting bosons with Rydberg atoms”. *Science* 365.6455 (2019), pp. 775–780 (cited on p. 28).
- [108] H. Levine, A. Keesling, G. Semeghini, A. Omran, T. T. Wang, S. Ebadi, H. Bernien, M. Greiner, V. Vuletić, H. Pichler, and M. D. Lukin. “Parallel Implementation of High-Fidelity Multiqubit Gates with Neutral Atoms”. *Phys. Rev. Lett.* 123 (17 2019), p. 170503 (cited on p. 28).
- [109] I. S. Madjarov, J. P. Covey, A. L. Shaw, J. Choi, A. Kale, A. Cooper, H. Pichler, V. Schkolnik, J. R. Williams, and M. Endres. “High-fidelity entanglement and detection of alkaline-earth Rydberg atoms”. *Nature Physics* 16.8 (2020), pp. 857–861 (cited on p. 28).
- [110] A. W. Young, W. J. Eckner, W. R. Milner, D. Kedar, M. A. Norcia, E. Oelker, N. Schine, J. Ye, and A. M. Kaufman. “Half-minute-scale atomic

coherence and high relative stability in a tweezer clock”. *Nature* 588.7838 (2020), pp. 408–413 (cited on p. 28).

- [111] T. Northup and R. Blatt. “Quantum information transfer using photons.” *Nature Photonics* 8 (2014), pp. 356–363 (cited on p. 28).
- [112] J. D. Hood, A. Goban, A. Asenjo-Garcia, M. Lu, S.-P. Yu, D. E. Chang, and H. J. Kimble. “Atom–atom interactions around the band edge of a photonic crystal waveguide”. *Proceedings of the National Academy of Sciences* 113.38 (2016), pp. 10507–10512 (cited on p. 29).
- [113] D. E. Chang, J. S. Douglas, A. González-Tudela, C.-L. Hung, and H. J. Kimble. “Colloquium: Quantum matter built from nanoscopic lattices of atoms and photons”. *Rev. Mod. Phys.* 90 (3 2018), p. 031002 (cited on p. 29).
- [114] P. Samutpraphoot, T. Đorđević, P. L. Ocola, H. Bernien, C. Senko, V. Vuletić, and M. D. Lukin. “Strong Coupling of Two Individually Controlled Atoms via a Nanophotonic Cavity”. *Phys. Rev. Lett.* 124 (6 2020), p. 063602 (cited on pp. 29, 30, 66–68).
- [115] J. Beugnon, C. Tuchendler, H. Marion, et al. “Two-dimensional transport and transfer of a single atomic qubit in optical tweezers.” *Nature Physics* 3 (2007), pp. 696–699 (cited on p. 29).
- [116] A. Lengwenus, J. Kruse, M. Schlosser, S. Tichelmann, and G. Birkl. “Coherent Transport of Atomic Quantum States in a Scalable Shift Register”. *Phys. Rev. Lett.* 105 (17 2010), p. 170502 (cited on p. 29).
- [117] J. D. Thompson, T. G. Tiecke, N. P. de Leon, J. Feist, A. V. Akimov, M. Gullans, A. S. Zibrov, V. Vuletić, and M. D. Lukin. “Coupling a Single Trapped Atom to a Nanoscale Optical Cavity”. *Science* 340.6137 (2013), pp. 1202–1205 (cited on pp. 30, 38, 97, 98).
- [118] *See Supplemental Material ()* (cited on pp. 30, 32, 35).
- [119] C. T. Nguyen, D. D. Sukachev, M. K. Bhaskar, B. Machielse, D. S. Levonian, E. N. Knall, P. Stroganov, C. Chia, M. J. Burek, R. Riedinger, H. Park, M. Lončar, and M. D. Lukin. “An integrated nanophotonic quantum

register based on silicon-vacancy spins in diamond”. *Phys. Rev. B* 100 (16 2019), p. 165428 (cited on pp. 30, 77).

- [120] S. Kuhr, W. Alt, D. Schrader, I. Dotsenko, Y. Miroshnychenko, A. Rauschenbeutel, and D. Meschede. “Analysis of dephasing mechanisms in a standing-wave dipole trap”. *Phys. Rev. A* 72 (2 2005), p. 023406 (cited on pp. 32, 61, 87–89).
- [121] D. Reitz, C. Sayrin, R. Mitsch, P. Schneeweiss, and A. Rauschenbeutel. “Coherence Properties of Nanofiber-Trapped Cesium Atoms”. *Phys. Rev. Lett.* 110 (24 2013), p. 243603 (cited on pp. 32, 87).
- [122] D. Hümmer, P. Schneeweiss, A. Rauschenbeutel, and O. Romero-Isart. “Heating in Nanophotonic Traps for Cold Atoms”. *Phys. Rev. X* 9 (4 2019), p. 041034 (cited on pp. 32, 89).
- [123] H. Y. Carr and E. M. Purcell. “Effects of Diffusion on Free Precession in Nuclear Magnetic Resonance Experiments”. *Phys. Rev.* 94 (3 1954), pp. 630–638 (cited on p. 34).
- [124] A. S. Sørensen and K. Mølmer. “Probabilistic Generation of Entanglement in Optical Cavities”. *Phys. Rev. Lett.* 90 (12 2003), p. 127903 (cited on p. 35).
- [125] W. Chen, J. Hu, Y. Duan, B. Braverman, H. Zhang, and V. Vuletić. “Carving Complex Many-Atom Entangled States by Single-Photon Detection”. *Phys. Rev. Lett.* 115 (25 2015), p. 250502 (cited on p. 35).
- [126] C. Sackett, D. Kielpinski, B. King, et al. “Experimental entanglement of four particles.” *Nature* 404 (2000), pp. 256–259 (cited on pp. 35, 76).
- [127] H. Kübler, J. P. Shaffer, T. Baluktsian, R. Löw, and T. Pfau. “Coherent excitation of Rydberg atoms in micrometre-sized atomic vapour cells”. *Nature Photonics* 4.2 (2010), pp. 112–116 (cited on p. 40).
- [128] S. Olmschenk, D. N. Matsukevich, P. Maunz, D. Hayes, L.-M. Duan, and C. Monroe. “Quantum Teleportation Between Distant Matter Qubits”. *Science* 323.5913 (2009), pp. 486–489 (cited on p. 40).

- [129] H. Choi, M. Pant, S. Guha, et al. “Percolation-based architecture for cluster state creation using photon-mediated entanglement between atomic memories.” *npj Quantum Inf* 5 (2019), p. 104 (cited on p. 41).
- [130] A. Reiserer, N. Kalb, G. Rempe, and S. Ritter. “A quantum gate between a flying optical photon and a single trapped atom”. *Nature* 508.7495 (2014), pp. 237–240 (cited on p. 42).
- [131] W. Dür, H.-J. Briegel, J. I. Cirac, and P. Zoller. “Quantum repeaters based on entanglement purification”. *Phys. Rev. A* 59 (1 1999), pp. 169–181 (cited on p. 43).
- [132] W. Dür and H. J. Briegel. “Entanglement purification and quantum error correction”. *Reports on Progress in Physics* 70.8 (2007), pp. 1381–1424 (cited on p. 43).
- [133] S. Krastanov, V. V. Albert, and L. Jiang. “Optimized Entanglement Purification”. *Quantum* 3 (2019), p. 123 (cited on p. 43).
- [134] B. Hacker, S. Welte, G. Rempe, and S. Ritter. “A photon–photon quantum gate based on a single atom in an optical resonator”. *Nature* 536.7615 (2016), pp. 193–196 (cited on p. 43).
- [135] B. Hacker, S. Welte, S. Daiss, A. Shaukat, S. Ritter, L. Li, and G. Rempe. “Deterministic creation of entangled atom–light Schrödinger-cat states”. *Nature Photonics* 13.2 (2019), pp. 110–115 (cited on p. 43).
- [136] R. Raussendorf and H. J. Briegel. “A One-Way Quantum Computer”. *Phys. Rev. Lett.* 86 (22 2001), pp. 5188–5191 (cited on p. 43).
- [137] J. Borregaard, H. Pichler, T. Schröder, M. D. Lukin, P. Lodahl, and A. S. Sørensen. “One-Way Quantum Repeater Based on Near-Deterministic Photon-Emitter Interfaces”. *Phys. Rev. X* 10 (2 2020), p. 021071 (cited on p. 43).
- [138] W. Bogaerts, D. Pérez, J. Capmany, D. A. Miller, J. Poon, D. Englund, F. Morichetti, and A. Melloni. “Programmable photonic circuits”. *Nature* 586.7828 (2020), pp. 207–216 (cited on p. 44).

- [139] A. H. Atabaki, S. Moazeni, F. Pavanello, H. Gevorgyan, J. Notaros, L. Alloatti, M. T. Wade, C. Sun, S. A. Kruger, H. Meng, K. Al Qubaisi, I. Wang, B. Zhang, A. Khilo, C. V. Baiocco, M. A. Popović, V. M. Stojanović, and R. J. Ram. “Integrating photonics with silicon nanoelectronics for the next generation of systems on a chip”. *Nature* 556.7701 (2018), pp. 349–353 (cited on p. 44).
- [140] C. Sun, M. T. Wade, Y. Lee, J. S. Orcutt, L. Alloatti, M. S. Georgas, A. S. Waterman, J. M. Shainline, R. R. Avizienis, S. Lin, B. R. Moss, R. Kumar, F. Pavanello, A. H. Atabaki, H. M. Cook, A. J. Ou, J. C. Leu, Y. H. Chen, K. Asanović, R. J. Ram, M. A. Popović, and V. M. Stojanović. “Single-chip microprocessor that communicates directly using light”. *Nature* 528.7583 (2015), pp. 534–538 (cited on p. 44).
- [141] R. J. Niffenegger, J. Stuart, D. Kharas, S. Bramhavar, C. D. Bruzewicz, W. Loh, R. T. Maxson, R. McConnell, D. Reens, G. N. West, J. M. Sage, and J. Chiaverini. “Integrated multi-wavelength control of an ion qubit”. *Nature* 586.October (2020) (cited on p. 44).
- [142] X. Luan, J.-B. Béguin, A. P. Burgers, Z. Qin, S.-P. Yu, and H. J. Kimble. “The Integration of Photonic Crystal Waveguides with Atom Arrays in Optical Tweezers”. *Advanced Quantum Technologies* 3.11 (2020), p. 2000008 (cited on p. 44).
- [143] J.-B. Béguin, A. P. Burgers, X. Luan, Z. Qin, S. P. Yu, and H. J. Kimble. “Advanced apparatus for the integration of nanophotonics and cold atoms”. *Optica* 7.1 (2020), pp. 1–2 (cited on p. 44).
- [144] S. Kuhr, W. Alt, D. Schrader, I. Dotsenko, Y. Miroshnychenko, W. Rosenfeld, M. Khudaverdyan, V. Gomer, A. Rauschenbeutel, and D. Meschede. “Coherence Properties and Quantum State Transportation in an Optical Conveyor Belt”. *Phys. Rev. Lett.* 91 (21 2003), p. 213002 (cited on p. 44).
- [145] S. Kuhr, W. Alt, D. Schrader, I. Dotsenko, Y. Miroshnychenko, A. Rauschenbeutel, and D. Meschede. “Analysis of dephasing mechanisms in a standing-wave dipole trap”. *Phys. Rev. A* 72 (2 2005), p. 023406 (cited on p. 44).

- [146] D. Bluvstein, A. Omran, H. Levine, A. Keesling, G. Semeghini, S. Ebadi, T. T. Wang, A. A. Michailidis, N. Maskara, W. W. Ho, S. Choi, M. Serbyn, M. Greiner, V. Vuletić, and M. D. Lukin. “Controlling quantum many-body dynamics in driven Rydberg atom arrays”. *Science* (2021) (cited on p. 45).
- [147] H. Kübler, J. P. Shaffer, T. Baluktsian, R. Löw, and T. Pfau. “Coherent excitation of Rydberg atoms in micrometre-sized atomic vapour cells”. *Nature Photonics* 4.2 (2010), pp. 112–116 (cited on p. 46).
- [148] E. R. Abraham and E. A. Cornell. “Teflon feedthrough for coupling optical fibers into ultrahigh vacuum systems”. *Appl. Opt.* 37.10 (1998), pp. 1762–1763 (cited on pp. 49, 103).
- [149] S. Gröblacher, J. T. Hill, A. H. Safavi-Naeini, J. Chan, and O. Painter. “Highly efficient coupling from an optical fiber to a nanoscale silicon optomechanical cavity”. *Applied Physics Letters* 103.18 (2013), p. 181104 (cited on p. 50).
- [150] J. Chan, M. Eichenfield, R. Camacho, and O. Painter. “Optical and mechanical design of a “zipper” photonic crystal optomechanical cavity”. *Opt. Express* 17.5 (2009), pp. 3802–3817 (cited on p. 50).
- [151] E. D. Black. “An introduction to Pound–Drever–Hall laser frequency stabilization”. *American Journal of Physics* 69.1 (2001), pp. 79–87 (cited on p. 52).
- [152] N. Schlosser, G. Reymond, and P. Grangier. “Collisional Blockade in Microscopic Optical Dipole Traps”. *Phys. Rev. Lett.* 89 (2 2002), p. 023005 (cited on p. 52).
- [153] D. Hümmer, P. Schneeweiss, A. Rauschenbeutel, and O. Romero-Isart. “Heating in Nanophotonic Traps for Cold Atoms”. *Phys. Rev. X* 9 (4 2019), p. 041034 (cited on p. 55).
- [154] K. M. Birnbaum, A. S. Parkins, and H. J. Kimble. “Cavity QED with multiple hyperfine levels”. *Phys. Rev. A* 74 (6 2006), p. 063802 (cited on p. 58).

- [155] R. E. Evans, M. K. Bhaskar, D. D. Sukachev, C. T. Nguyen, A. Sipahigil, M. J. Burek, B. Machielse, G. H. Zhang, A. S. Zibrov, E. Bielejec, H. Park, M. Lončar, and M. D. Lukin. “Photon-mediated interactions between quantum emitters in a diamond nanocavity”. *Science* 362.6415 (2018), pp. 662–665 (cited on p. 60).
- [156] Y. Meng, C. Liedl, S. Pucher, A. Rauschenbeutel, and P. Schneeweiss. “Imaging and Localizing Individual Atoms Interfaced with a Nanophotonic Waveguide”. *Phys. Rev. Lett.* 125 (5 2020), p. 053603 (cited on p. 70).
- [157] H. Bernien, B. Hensen, W. Pfaff, et al. “Heralded entanglement between solid-state qubits separated by three metres.” *Nature* 497 (2013), pp. 86–90 (cited on p. 75).
- [158] W. K. Wootters. “Entanglement of formation and concurrence”. *Quantum Inf. Comput.* 1.1 (2001), pp. 27–44 (cited on p. 77).
- [159] T. A. Savard, K. M. O’Hara, and J. E. Thomas. “Laser-noise-induced heating in far-off resonance optical traps”. *Phys. Rev. A* 56 (2 1997), R1095–R1098 (cited on p. 89).
- [160] R. Grimm, M. Weidemuller, and Y. Ovchinnikov. “Optical dipole traps for neutral atoms”. *Advances in Atomic, Molecular and Optical Physics* 42 (2000), pp. 95–170 (cited on p. 90).
- [161] C. Tuchendler, A. M. Lance, A. Browaeys, Y. R. P. Sortais, and P. Grangier. “Energy distribution and cooling of a single atom in an optical tweezer”. *Phys. Rev. A* 78 (3 2008), p. 033425 (cited on pp. 93, 97).
- [162] W. Alt, D. Schrader, S. Kuhr, M. Müller, V. Gomer, and D. Meschede. “Single atoms in a standing-wave dipole trap”. *Phys. Rev. A* 67 (3 2003), p. 033403 (cited on p. 97).
- [163] A. Kaufman. “Laser cooling atoms to indistinguishability: Atomic Hong-Ou-Mandel interference and entanglement through spin exchange”. PhD thesis. University of Colorado at Boulder, 2015 (cited on p. 104).

- [164] S. Debnath, N. M. Linke, C. Figgatt, K. A. Landsman, K. Wright, and C. Monroe. “Demonstration of a small programmable quantum computer with atomic qubits”. *Nature* 536.7614 (2016), pp. 63–66 (cited on p. 109).
- [165] C. Weitenberg, M. Endres, J. F. Sherson, M. Cheneau, P. Schauß, T. Fukuhara, I. Bloch, and S. Kuhr. “Single-spin addressing in an atomic Mott insulator”. *Nature* 471.7338 (2011), pp. 319–324 (cited on p. 109).
- [166] T. Xia, M. Lichtman, K. Maller, A. W. Carr, M. J. Piotrowicz, L. Isenhower, and M. Saffman. “Randomized Benchmarking of Single-Qubit Gates in a 2D Array of Neutral-Atom Qubits”. *Phys. Rev. Lett.* 114 (10 2015), p. 100503 (cited on p. 109).